Cross sensitivity analysis of optical fibre-based sensing for high pressure, high temperature measurement in oil and gas applications.

AMOS, S.U.

2018

Cross sensitivity analysis of optical fibre based sensing for high pressure high temperature measurement in oil and gas applications

Solomon UDOH Amos

A thesis submitted in partial fulfilment of the requirements for the degree of

Doctor of Philosophy

at

Robert Gordon University

School of Engineering

February 2018

PhD candidate

Solomon UDOH Amos

Supervisory team

Dr. Radhakrishna Prabhu

Dr. James Njuguna

School of Engineering, Robert Gordon University, The Sir Ian Wood Building, Riverside East, Garthdee Road, Aberdeen, AB10 7GJ, United Kingdom.

Funding organization

Petroleum Technology Development Fund (PTDF), Nigeria

To Bibiana,

my wife, mother of our beautiful daughter,

and the woman I want to grow old with.

Acknowledgements

I would like to thank my primary supervisor, Dr. Radhakrishna Prabhu for his invaluable guidance, great amount of support and patience while undertaking this research. Prabhu trusted me with his many wonderful ideas during the course of my studies and at the same time encouraged me to further explore and develop these ideas my own way while offering me great advice. He has inspired me not only as an academic but also as a person. I am very privileged to have worked under his supervision. I would also like to acknowledge my secondary supervisor, Dr. James Njuguna for his advice and support for many aspects of this work.

My sincere appreciation goes to the funding body Petroleum Technology Development Fund (PTDF) that enabled me pursue this project.

I feel lucky to be part of a vibrant and motivating research group within the research community. A big thanks to Dr. Kaushal Bhavsar who always supported me and gave his invaluable insights on some concepts I found very difficult to demystify.

A big thanks to my family who are miles away and always send their support, encouragement and love.

Abstract

Measurements of physical parameters like pressure, temperature, flow rate, vibrations and displacement in harsh environment are often desired in the oil and gas industry. Pressure and temperature are the most important parameters among them. Changes in pressure and temperature have a major role in many downhole processes and they have enabled the performance of producing wells, water-injection profiles, fracture jobs, carbon dioxide (CO_2) injection, and enhanced oil recovery to be successfully monitored over the years. However, measurements of these parameters were mostly carried out by logging tools that comprise several conventional electronic gauges. Temperature and pressure in deep and ultra-deep wells could reach beyond $300\,℃$ and $20000\,kPa$. Fibre optic sensor developments have created new interest in oil and gas production monitoring and control. Fibre optic sensors currently deployed in the oil and gas industry can only operate up to $150\,℃$ and even the most robust sensors are limited below $300\,℃$.

In this research, the effect of cross sensitivity on multi-parameter optical fibre sensor for oil and gas applications in harsh environments is studied and analysed. Mathematical models of the cross sensitivity function of fibre Bragg grating (FBG) and its physical mechanism has been developed. This analysis was based on the fact that FBG sensor was in the state in which temperature and pressure were simultaneously functioning on.

The main objective of this research is to investigate the cross sensitivity effect of fibre optic sensing technology for oil and gas sensing applications by

designing sensing structures and developing theoretical equations for the system model of the optical fibre sensor capable of addressing this issue.

Different techniques have been proposed to tackle this cross sensitivity challenge. Firstly, the use of dual sensing structure that investigate and analysed the spectral characterization of a Fabry-Perot interferometer (FPI) sensor and the interaction with physical parameters. Preliminary results of this configuration are used to eliminate the issue of temperature-pressure cross-sensitivity and effectively improve the resolution of the sensor system. Secondly, the concept of a metal coated hybrid sensing system is proposed. The theoretical design and analysis of a metal coated hybrid sensing system of FBG and Extrinsic Fabry-Perot Interferometer (EFPI) cavity for high pressure high temperature (HPHT) measurement in oil and gas applications is reported. The FBG and EFPI are used to measure temperature and pressure respectively. This configuration is able to solve the problem of cross sensitivity. Lastly, a novel thin-film fibre optic extrinsic FPI sensor with an ultra-high pressure and temperature sensitivities are analysed theoretically using 16-layer graphene film deposited on silicon carbide (SiC) substrate as the diaphragm. The performance parameters of the proposed sensor are investigated in terms of sensitivity at the operating wavelength of $1550\,nm$. It was observed in the numerical study that the sensitivity can be greatly increased by using multilayer graphene on SiC substrate. This sensor is expected to have potential for monitoring oil and gas applications in harsh environments.

Contents

List of Figures

List of Table

Nomenclature

Symbol	Description
λ_B	Bragg wavelength
$\Delta\lambda_B$	Shift in Bragg wavelength
n_{eff}	Effective refractive index
Λ	Grating period
E_i	Electric field
A	Amplitude
B	Magnetic field
$\mathcal{E}_0$	Permittivity of free space
μ_0	Permeability of free space
H	Magnetising field
ε	Strain
ε_r	Radial strain
ε_z	Axial strain
P	Pressure
T	Temperature
R	Reflectivity
$\Delta\varepsilon$	Change in strain
ΔT	Change in Temperature
ΔP	Change in pressure
K_T	Temperature sensitivity
K_P	Pressure sensitivity
K_ϵ	Strain sensitivity
P_e	Effective strain-optic constant

ξ	Thermo-optic coefficient
α	Coefficient of thermal expansion
ν	Poisson's ratio
P_{11}, P_{12}	Pockels constant
E	Young's modulus
L	Grating length
$\varphi(z)$	Phase angle
κ	AC coupling
$\hat{\sigma}$	DC coupling
β	Mode propagation constant
$R(z)$	Amplitude of forward propagation
$S(z)$	Amplitude of backward propagation
∂_n	Change in refractive index
χ_{cs}	Cross sensitivity term
I_1, I_1	Light intensities
P_{max}, P_{min}	Maximum and minimum reflected power
∂_{dia}	Diaphragm sensitivity
K_1	Thermal axial coefficient
$\Delta\partial r_1$	Free radial elongation
∇	Three dimensional gradient operator
Σ	Summation

Chapter 1

1 Downhole monitoring of oil and gas production

1.1 Introduction

The recovery of oil from deep reservoirs is one of the major challenges facing the oil and gas industry as a result of limited availability of downhole information like temperature, pressure, flowrate etc. This information plays a major role in improving the performance (production) of the reservoir and well optimization. Fundamental understanding and knowledge of where hydrocarbons are located, the volume of the hydrocarbons in place and how to exploit and extract them cost effectively, with enhanced operational efficiency, improved safety and security are necessary requirements for the oil and gas industry. Over the last decade, companies have invested large amount of capital in sensors for oil and gas production. However, they are still seeking new approaches to maximizing their reservoir production given the current global oil market downturn and thus realise the return on investment for their developed sensors. Measurements of physical parameters like temperature and pressure provide important resources for most downhole processes and have enabled monitoring of the performance of producing wells, water injection profiles and enhanced oil recovery.

The measurements of these physical parameters have been done using conventional electronic gauges. The recovery becomes more and more challenging and difficult as exploration and production operations seek new frontiers into deep and ultra-deep environments with approximately up to

$3000\,m$ of water depth. These gauges tend to fail under high pressure high temperature (HPHT) environments.

Fibre optic sensors have been developed and have been applied to a wide range of industrial and commercial applications. The ability of fibre optic sensors to accurately measure large numbers of physical parameters in harsh conditions in a distributed framework has enabled tremendous success in sensing and monitoring in other industries like power, aerospace, and telecommunications and has now started to be deployed in the oil and gas industry. Moreover, with the fibre being able to serve as the sensing probe and the communication channel along with other features (immune to electromagnetic interference, small size, intrinsically safe) make them particularly well suited for applications within the oil and gas industry. However, fibre optic sensors can only measure temperature up to $150\,℃$ [1]. There is no industry defined standard for downhole monitoring of pressure and temperature in the oil and gas industry. Typical downhole monitoring systems should measure pressure ranges up to $20{,}000\,kPa$, temperature range up to $300\,℃$ with high accuracy and high resolution of 0.03% and 0.005% of full scale respectively [1].

1.2 Motivation

Downhole monitoring has been in existence as far back as 1960 [2] when electronic gauges were the only available devices for measuring downhole information such as temperature, pressure, flowrate etc. As the demand for exploration of oil and gas increases, the oil and gas industry is extending the operating limit of the current conventional sensing capability to achieve improved reliability, better efficiency and longer life span. However, the extreme harsh environment of the reservoir, consisting of strong electromagnetic interference (EMI), HPHT and a highly corrosive chemical

environment lead to extremely severe requirements on the conventional electronic sensing system used in downhole monitoring. Thus, conventional electronic sensing systems, usually fail to meet the demand [3].

Electronic systems have been installed and tested in various oilfields [4, 5]. The major challenge of these electronic sensors is that they become extremely unreliable when deployed in HPHT environments [6]. A previous study has shown the application of permanent downhole temperature and pressure gauges in the reservoir management of two complex North Sea oilfields, 40 quartz and quartz capacitance gauges were installed in areas with downhole temperatures of $70\,°C$ to $130\,°C$. Of these 40 installations, 17 failed in the first two years [5].

Optical fibre sensors have been developed and they have many advantages over the conventional electronic sensors due to their small size, immunity to EMI, robustness and chemical inertness. They are also intrinsically safe (they do not cause explosion) making them applicable in harsh environments since they do not make use of electrical signals. The two major types of optical fibre sensors are the fibre Bragg grating (FBG) and the Fabry-Perot interferometer (FPI) fibre sensors. The FBG sensor has the ability to multiplex multiple arrays of fibre sensors into a single fibre which is capable of measuring different parameters such as temperature, strain, pressure, humidity and flowrate [3]. However, the major challenge of FBG sensor is the issue of cross sensitivity. This is the fact that FBG is simultaneously sensitive to both temperature and pressure. The reflectance spectrum of an FBG responds to both temperature and pressure changes which in turn affects the accuracy of the sensor.

1.3 Fibre optic sensors

The field of fibre optic sensing has been growing for the past 30 years since it was first developed in 1971 [7-9]. The applications of fibre optic sensors are increasing widely in a variety of different fields, mainly due to their immunity to electromagnetic interference, high sensitivity, good resolution, large dynamic range, multiplexing capabilities, remote signal processing ability, electrically passive nature, ability to withstand harsh environments, intrinsically safe nature, small size and light weight. As a result of these advantages, numerous fibre optic sensing technologies have been developed over the years in a wide variety of applications. The applications and principles are extremely diversified with various mechanisms for measurements of physical parameters like pressure, temperature, flow rate, vibration and displacement, strain, electromagnetic field and chemicals using optical fibres. They are becoming very attractive for biomedical sensing, structural health monitoring, military and defence, power, telecommunications and aerospace in recent years.

The material properties of optical fibres play a very important role in their advantages over conventional electronic sensors. The single mode fibre is the most widely used optical fibre in sensing and it operates within the $1310\,nm$ to $1550\,nm$ range [10]. The fibre properties like the low attenuation exhibited within this range ($< 0.35\,dB/km$ @$1310\,nm$ and $< 0.22\,dB/km$ @$1550\,nm$) enables data to be transmitted from the sensing region to the interrogation instrument without any significant loss of key information across long distances [11]. Also optical fibres have good material strength and do not easily break. However,

the material strength reduces when subject to large tension stress. The use of protective coating strengthens the fibre and maintains long term reliability of the fibre.

Fibre optic sensors have been extensively researched for oil and gas applications [12]. The areas of applications include downhole production monitoring, seismic sensing, downstream process monitoring, structural health and pipeline monitoring in the field of exploration, production and products distribution. Despite the many advantages of fibre optic sensors, they have not been extensively commercialised owing to the more developed and established conventional sensors. Therefore, a successful fibre optic sensor must offer compelling advantages that the conventional sensor cannot match.

This work focuses on designing sensing structures and developing theoretical models of the optical fibre sensors in oil and gas industry. The basic idea is to use a single mode fibre to develop a multifunctional sensing system capable of measuring temperature and pressure reliably and accurately. Some of the fibre optic sensors that have been demonstrated in the oil and gas industry employ the distributed temperature sensing (DTS) [13] for temperature profiling, FBG [14] based sensing for multi parameters measurement and Fabry-Perot (FP) [9, 15, 16] sensing for point based sensing.

1.3.1 Distributed temperature sensing (DTS)

Detecting temperature change has a major role in understanding and monitoring many downhole processes and temperature measurements have enabled monitoring of the performance of producing wells, water-injection profiles, etc over the years. However, measurements of temperature were mostly carried out by wireline logging tools that comprise several electronic

gauges. Fibre optic sensor developments have created new interest in temperature measurements for oil and gas production. Fibre optic technology used in measuring temperature is known as the Distributed Temperature Sensing (DTS), which measures temperature by means of fibre optic cable that provides a continuous profile of temperature along the fibre which is based on the detection of backscattering light using the Raman [17], Rayleigh [18] and Brillouin [19] principles as shown in Figure 1.1

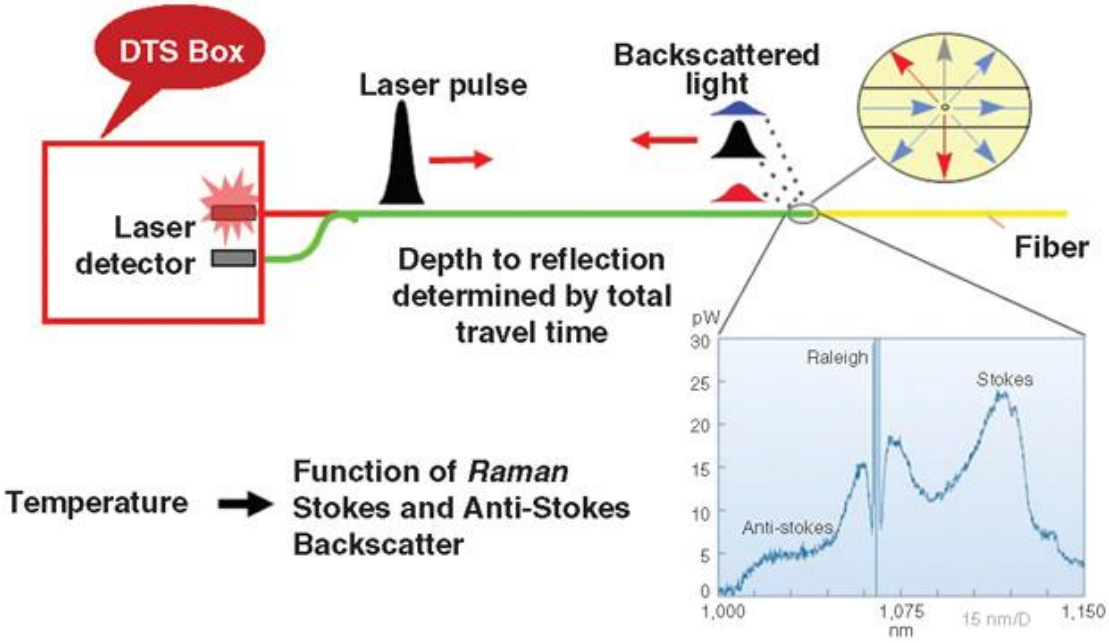

Figure 1.1 DTS based on Raman stoke and anti-stoke backscattering [20]

The back-scattered light contains three spectral components, the Rayleigh scattering with wavelength of laser source, the Stokes component with the higher wavelength in which the photons are generated, and the Anti-Stokes components with a lower wavelength. The intensity of the Anti-Stokes band is temperature dependent, while the Stokes band is temperature insensitive. The ratio of the Anti-Stokes and the Stokes light intensities provides the local temperature measurement [20]

DTS has the capability of measuring temperature along the entire fibre length (multiple points) simultaneously, compared to other traditional methods that measure temperature on a point-by-point basis. Several works on DTS have been reported [13, 17]. The DTS was the first commercially successful monitoring optical technology deployed in the oil and gas industry [21]. DTS has since been used in operating and development fields and in 2000, DTS data was successfully used in identifying formation damage in a production field [22]. The DTS data was used to locate and monitor steam breakthrough zones in steam flooding projects [23]. Also, numerical methods for estimating the flowrate profile from temperature profile using DTS has been reported [24]. It was discovered that the DTS data can be used to estimate the production profile for a single phase flow. However, for horizontal or multiphase flow, additional information will be needed to measure flowrate by means of DTS. It was later reported on how DTS was successfully used in estimating production flowrate even after gas breakthrough that involved multiphase flow [25]. Other area where the DTS has been successfully implemented is in pipeline leak detection and asset integrity [26].

1.3.2 Fibre Bragg grating (FBG)

The FBG is an important sensing element for measuring multi-parameter measurands such as strain, temperature, pressure and flow and has been extensively studied over the past 20 years [14]. The FBG has its origin from the discovery of the photosensitivity of germanium-doped silica fibre and was first demonstrated by Hill *et al* at the Canadian Communications Research Centre (CRC), Ottawa, Ontario in 1978 [27, 28]. They used a germanium-doped silica fibre that has its light source from the radiation of ion laser of argon and after some few minutes, they observed that an increase in the

intensity of the reflected light with the exposure time until total reflection occurred. It was later confirmed that a narrowband Bragg grating filter was formed over the entire $1\,m$ length of fibre. Their success subsequently resulted into the research of germanium-doped silica fibre properties. In 1989, Meltz *et al* [29] further demonstrated that a permanent refractive index change occurred when a germanium-doped fibre is exposed to direct ultraviolet (UV) light.

Initially, the photo-induced reflectivity observation was more of scientific interest, but it later become the foundation for a technology which now has broad role in sensor systems and optical communications. Research and development underlying the mechanism of fibre grating and its numerous applications is still ongoing. FBGs are now commercially available and have found major applications in structural health monitoring and state of the art telecommunications networks. Extensive review of literature was carried out to understand the underlying mechanism and characterization of the FBG.

The FBG mechanism occurs when the periodic perturbation of the refractive index along the fibre optic length is formed by exposing the core of the fibre to a periodic pattern of intense ultraviolet (UV) light. This exposure induces a permanent change to the refractive index of the core of the fibre optic cable. A small amount of incident light is reflected at each periodic refractive index change when it is in phase with the grating period while others are transmitted to the other end as they are not in phase with the grating period as shown in Figure 1.2. The entire reflected light waves are combined into one large reflection at a particular wavelength where the strongest mode coupling occurs.

This is known as the Bragg condition and the wavelength at which this occurs is called the Bragg wavelength [13].

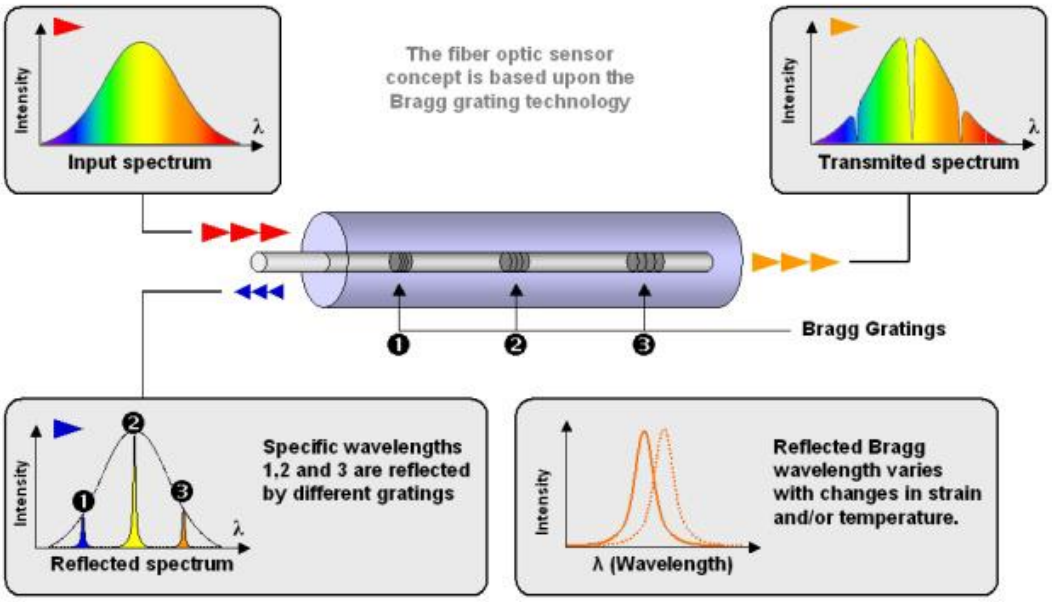

Figure 1.2 Schematic of FBG technology and basic operating principle [19]

The Bragg wavelength λ_B is given by [14]

$$\lambda_B = 2n_{eff}\Lambda$$

where n_{eff} is the effective refractive index of the fibre for optical mode propagation along the fibre and Λ is the grating period. This shows that the Bragg wavelength is dependent on the refractive index and the grating period, so any changes on the physical structure on either of them will cause a shift of the Bragg grating wavelength. This means that such a device can be used as sensor. FBG based sensors have a distinctive advantage over the electronic systems and other optic fibre configurations due to its multiplexing capability that allows a single fibre optic cable with tens of gratings to measure a large

range of parameters. This research on FBG for real time monitoring and control of oil and gas production will involve the area of simulation of FBG and its theoretical and experimental validations. The simulation of the effect of external perturbations on shift in wavelength of FBG using wideband light source also needs to be investigated for the design of FBG sensor systems. Multi parameter measurements using FBG have been reported [30, 31], where strain and temperature perturbations are acting on the Bragg gratings simultaneously. One challenge in FBG is the problem of cross sensitivity; when the sensor is simultaneously sensitive to both strain and temperature [32]. The cross sensitivity is not only affected by the external parameters such as temperature and pressure, but also by the properties of the fibre materials. The cross sensitivity effect of an FBG sensor in most oil and gas applications is crucial and should be minimized so that decoupling of temperature and pressure measurement is simplified sensor interrogation.

To overcome these limitations, this research will also look into the possible methods of discriminating between these parameters. Detailed study into the properties and principle of FBG characterization is presented in chapter 3.

1.3.3 Fabry-Perot interferometer (FPI)

There is increasing interest in utilizing miniature fibre optic sensors for pressure/temperature monitoring due to their advantages over conventional sensors, such as immunity to electromagnetic interference, high resolution, fast response, and compact size [1]. The pressure sensors that are based on the Fabry–Perot interferometer (FPI) have shown promising results for obtaining static and dynamic pressure measurements [33, 34]. The FPI sensor is typically constructed directly on a fibre end-face and consists of a cleaved optical fibre and a pressure/acoustic-sensitive

diaphragm known as an extrinsic Fabry–Perot interferometric (EFPI) sensor structure. The pressure sensitivity of the diaphragm in the FPI sensor is defined as the ratio of the FPI cavity's length variation to the pressure [35]. The key elements that determine the pressure sensitivity of the FPI sensor are the materials used and the thickness of the diaphragm. In this work, FPI pressure sensors with different types of materials as a pressure-sensitive diaphragm, including copper metal and nickel metal, silicon carbide and graphene membrane are investigated.

1.4 Sensor requirements for pressure and temperature measurements in the oil and gas industry

The fibre optic sensor needed in the oil and gas industry for downhole monitoring must satisfy the following requirements:

1. High pressure ($15000 - 20000\ kPa$) and temperature ($500\ ℃$) measuring capabilities.
2. Reliability
3. Good thermal strength
4. Good resistance to chemical corrosion

The material selection is very important in sensor design and development since the limitations and capabilities of fibre optic sensors are mostly dependent on the materials they are made with. Various fibre optic sensor materials have been developed, they include fused-silica, polymers, silver, glasses, and crystals. The material selection for this research was based on two main criteria: firstly, the material for the sensor design should have the capability to withstand harsh environments and still maintain reasonably good mechanical and optical properties; secondly, the materials selected for the sensor design have similar thermal properties. Since sensing systems developed and

constructed out of similar or uniform materials have good reliability, stability and survivability when used in high temperature and high pressure applications, than those made of different materials that mostly suffer from thermal expansion mismatch. Based on these, fused-silica, silicon carbide (SiC), for the material of choice for the sensor diaphragm, copper (Cu) and nickel (Ni) are the selected materials for the sensor design in this project. To achieve a miniaturised optimised sensor, graphene was selected for ultra-thin sensor design capable of meeting both criteria listed above.

The selected materials have good thermal, mechanical and optical properties when used in HPHT applications. This work started with fused-silica based fibre optic sensor, then progressed to aluminium and SiC diaphragm based sensors. With these initial efforts, there is need to design the sensor structure capable of withstanding HPHT environments.

HPHT sensing systems are highly desirable in the oil and gas industry such as downhole monitoring and subsea underwater structure monitoring. In downhole monitoring, a fibre optic sensor system would greatly help to detect any abnormal surge in pressure and temperature and which in turn improve the performance and efficiency. However, downhole temperature and pressure can reach as high as $500\,℃$ and $15000 - 20000\,kPa$ respectively. These extreme harsh environments pose huge challenges to the current fibre optic sensing technology which could affect the design, material or coating of the sensor. Conventional electronic sensors and current fibre optic sensors are usually limited to $150\,℃$ and would fail as oil and gas production gets into the phase of extremely harsh environments. Different materials for sensing HPHT environments have been explored to develop temperature and pressure sensors, including SiC , sapphire fibre [36, 37], ceramic [38] and diamond [39].

However, almost all of these are diaphragm based design and have employed either capacitive or piezoelectric detection.

1.5 Aim and objectives

One of the focuses of fibre optic sensing for oil and gas applications for HPHT environments is pressure and temperature sensing. The FBG sensor has been extensively used in fibre sensor applications owing to its compactness in structure, simplicity in fabrication and wavelength coding in measurements. However, in temperature and pressure sensor applications, it is difficult to distinguish between temperature and pressure effects, as the FBG is sensitive to both.

The main aim of this research is to design and analyse optical sensing systems capable of addressing the cross sensitivity problem that may exist in FBG for high pressure high temperature measurements

To achieve this aim, a few objectives have been identified that need to be met. They are outlined below:

1. Sensitivity and cross-sensitivity analysis of FBG based sensor for temperature and pressure measurements.
2. Design and development of a sensor head comprising the use of FBG and EFPI for simultaneous measurement of temperature and pressure in permanent downhole monitoring of oil and gas wells.
3. Analysis of the spectral characterization of the multiplexed FBG and EFPI and the proposed mechanism for separating the FBG response from the EFPI.

4. Establishing a de-multiplexing mathematical model for the FBG and EFPI multiplexed sensor for temperature and pressure measurements respectively.
5. The theoretical design and analysis of a double metal coated sensing system of FBG and EFPI cavity for HPHT measurement in harsh environments.
6. The theoretical design and analysis of a novel ultra-thin pressure and temperature sensor based on graphene diaphragm and FBG.

1.6 Thesis organization

In spite of the great progress recently being made with fibre optic sensor technology, there are still many challenges yet unsolved. The oil and gas industry are very slow in adopting this technology. The goal of this thesis is to carry out the design and analysis of sensing systems to tackle the problem of cross sensitivity of FBG in HPHT measurements for oil and gas applications. The concept was based on the fact that the interaction of the physical parameters and light wave properties pose a serious cross sensitivity challenge on the reliability of FBG sensor. A review of the principles of operation of conventional pressure and temperature sensors is presented in chapter 2 in order to ascertain that the current solutions available in the industry are not sufficient in meeting the goal of this research. The introduction and review of optical fibre sensor as an alternative for measuring such parameters are also presented. Wavelength, intensity, interferometric and polarization modulation based sensing are described. Lastly the sensing principles of FBG for temperature, strain and pressure are detailed. These provide different design and

measurement techniques from which the most practical ones are considered for the solution of addressing the cross sensitivity problem.

On selecting the most suitable optical fibre based sensor in order for the measurement requirements to be met, numerical analysis of the FBG sensor when subject to external perturbations is detailed in chapter 3. Modelling, simulation and characterization of the Bragg grating which are based on solving the coupled-mode theory (CMT) equation by using the transfer matrix method are carried out. The effect of spectral reflectivity dependence on the grating length and refractive index are analysed and investigated. The effect of bandwidth dependence on the grating length and refractive index is also investigated and the simulation results are presented in section 3.3. Finally in chapter 3, the theoretical models of the cross sensitivity function of FBG and its physical mechanism is developed and analysed. This analysis is based on the fact that FBG sensor is in the state in which the strain, temperature and pressure are simultaneously functioning on. Based on the interaction of the physical parameters of the sensor and light wave properties, this poses a serious cross sensitivity challenge on the reliability of the FBG sensor.

To overcome this limitation and minimise the effect of cross sensitivity in FBG sensor, a multiplexed FBG/EFPI sensor for simultaneous measurement of temperature and pressure is designed in chapter 4. Analysis of the spectral characterizations (basic sensor system configuration, finesse, fringe visibility, sensor mechanical analysis which includes diaphragm deflection, frequency response and stress distribution) are presented and a de-multiplexing mathematical model for the multiplexed sensor is also carried out.

A technique for protecting the optical fibre sensor when exposed to HPHT environments while still having the capacity to minimise the effect of cross sensitivity of the sensor is investigated in chapter 5. The variation of the optical and structural properties is detailed. The optical analysis is carried out to obtain the spectral response of the sensor while the structural analysis is used to obtain the change in optical properties of the sensor due to photo-elastic effect. After reviewing the theoretical analysis and the limitation of the technique presented in chapter 5, a novel ultra-thin sensing configuration with graphene diaphragm deposited in SiC substrate is presented in chapter 6.

Finally, chapter 7 summarizes the thesis and provides conclusions based on the research carried out. Further work based on this thesis is also suggested in this chapter.

1.7 References

[1] Y. J. Rao, "Recent progress in fiber-optic extrinsic Fabry–Perot interferometric sensors," Optical Fiber Technology, vol. 12, pp. 227-237, 2006.

[2] W. A. Nestlerode, "The Use Of Pressure Data From Permanently Installed Bottom Hole Pressure Gauges." Society of Petroleum Engineers. doi:10.2118/590-MS, 1963.

[3] A. D. Kersey, "Optical fiber sensors for permanent downwell monitoring applications in the oil and gas industry," *IEICE Trans. Electron,* vol. 3, pp. 400 - 404, 2000.

[4] M. F. C. Bezerra, S. F. Da Silva, and B. C. Theuveny, "Permanent Downhole Gauges: A Key To Optimize Deepsea Production." *Offshore Technology Conference*, Jan. 1992.

[5] T. Unneland, "Permanent Downhole Gauges Used in Reservoir Management of Complex North Sea Oil Fields," *Society of Petroleum Engineers*, Aug. 1994.

[6] P. M. Nellen, P. Mauron, A. Frank, U. Sennhauser, K. Bohnert, P. Pequignot, P. Bodor, and H. Brändle, "Reliability of fiber Bragg grating based sensors for downhole applications," *Sensors and Actuators A: Physical,* vol. 103, pp. 364-376, 2003.

[7] V. Vali and R. W. Shorthill, "Fiber ring interferometer," *Applied Optics,* vol. 15, pp. 1099-1100, 1976.

[8] A. J. Rogers, "Optical methods for measurement of voltage and current on power systems," *Optics & Laser Technology,* vol. 9, pp. 273-283, 1977.

[9] A. D. Kersey, "A Review of Recent Developments in Fiber Optic Sensor Technology," *Optical Fiber Technology,* vol. 2, pp. 291-317, 1996.

[10] A. W. Snyder and J. Love, *Optical Waveguide Theory*: Springer US, 1983.

[11] M. Yasin, S. W. Harun, and H. Arof, *Recent progress in optical fiber research*: InTech, 2011.

[12] A. D. Kersey, "Optical fiber sensors for permanent downwell monitoring applications in the oil and gas industry," *IEICE Trans. Electron,* vol. 3, pp. 400 - 404, 2000.

[13] A. H. Hartog, A. P. Leach, and M. P. Gold, "Distributed temperature sensing in solid-core fibres," *Electronics Letters,* vol. 21, pp. 1061-1062, 1985.

[14] A. D. Kersey, M. A. Davis, H. J. Patrick, M. LeBlanc, K. P. Koo, C. G. Askins, M. A. Putnam, and E. J. Friebele, "Fiber grating sensors," *Journal of Lightwave Technology,* vol. 15, pp. 1442-1463, 1997.

[15] D. A. Jackson, "Recent progress in monomode fibre-optic sensors," *Measurement Science and Technology,* vol. 5, p. 621, 1994.

[16] B. H. Lee, Y. H. Kim, K. S. Park, J. B. Eom, M. J. Kim, B. S. Rho, and H. Y. Choi, "Interferometric Fiber Optic Sensors," *Sensors,* vol. 12, p. 2467, 2012.

[17] T. Shiota and F. Wada, "Distributed temperature sensors for single-mode fibers," 1992, pp. 13-18.

[18] A. Hartog, "A distributed temperature sensor based on liquid-core optical fibers," *Journal of Lightwave Technology,* vol. 1, pp. 498-509, 1983.

[19] J. P. Dakin, D. J. Pratt, G. W. Bibby, and J. N. Ross, "Distributed optical fibre Raman temperature sensor using a semiconductor light source and detector," *Electronics Letters,* vol. 21, pp. 569-570, 1985.

[20] A. Ukil, H. Braendle, and P. Krippner, "Distributed Temperature Sensing: Review of Technology and Applications," *IEEE Sensors Journal,* vol. 12, pp. 885-892, 2012.

[21] B. K. Drakeley, E. S. Johansen, E. Zisk, and T. Bostick, III, "In-well Optical Sensing - State Of The Art Applications And Future Direction For Increasing Value in Production Optimization Systems." *Society of Petroleum Engineers*, Jan. 2006.

[22] J. S. James and S. A. v. der, "Distributed temperature sensing - A DTS primer for oil and gas production," *Unclassified, Shell International Exploration And Production B. V., The Hague, ,* 2003.

[23] D. K. Nath, R. Sugianto, and D. B. Finley, "Fiber-Optic Distributed Temperature Sensing Technology Used for Reservoir Monitoring in an Indonesia Steam Flood," 2007.

[24] L. B. Ouyang and D. L. Belanger, "Flow Profiling by Distributed Temperature Sensor (DTS) System - Expectation and Reality," *Society of Petroleum Engineers, May* 2006.

[25] G. A. Brown, "Monitoring Multilayered Reservoir Pressures and GOR Changes Over Time Using Permanently Installed Distributed Temperature Measurements." *Society of Petroleum Engineers*, 2006

[26] F. Tanimola and D. Hill, "Distributed fibre optic sensors for pipeline protection," *Journal of Natural Gas Science and Engineering,* vol. 1, pp. 134-143, 2009.

[27] K. O. Hill, Y. Fujii, D. C. Johnson, and B. S. Kawasaki, "Photosensitivity in optical fiber waveguides: Application to reflection filter fabrication," *Applied Physics Letters,* vol. 32, pp. 647-649, 1978.

[28] B. S. Kawasaki, K. O. Hill, D. C. Johnson, and Y. Fujii, "Narrow-band Bragg reflectors in optical fibers," *Optics Letters,* vol. 3, pp. 66-68, 1978.

[29] G. Meltz, W. W. Morey, and W. H. Glenn, "Formation of Bragg gratings in optical fibers by a transverse holographic method," *Optics Letters,* vol. 14, pp. 823-825, 1989.

[30] C. M. Lawrence, D. V. Nelson, and E. Udd, "Multiparameter sensing with fiber Bragg gratings," vol. 2872, pp. 24-31, 1996.

[31] C. M. Lawrence, D. V. Nelson, E. Udd, and T. Bennett, "A fiber optic sensor for transverse strain measurement," *Experimental Mechanics,* vol. 39, pp. 202-209, 1999.

[32] M. G. Xu, J. L. Archambault, L. Reekie, and J. P. Dakin, "Discrimination between strain and temperature effects using dual-wavelength fibre grating sensors," *Electronics Letters,* vol. 30, pp. 1085-1087, 1994.

[33] S. Avino, J. A. Barnes, G. Gagliardi, X. Gu, D. Gutstein, J. R. Mester, C. Nicholaou, and H.-P. Loock, "Musical instrument pickup based on a laser locked to an optical fiber resonator," *Optics Express,* vol. 19, pp. 25057-25065, 2011.

[34] T. W. Kao and H. F. Taylor, "High-sensitivity intrinsic fiber-optic Fabry–Perot pressure sensor," *Optics Letters,* vol. 21, pp. 615-617, 1996.

[35] Y. Wang, D. N. Wang, C. Wang, and T. Hu, "Compressible fiber optic micro-Fabry-Pérot cavity with ultra-high pressure sensitivity," *Optics Express,* vol. 21, pp. 14084-14089, 2013

[36] A. Wang, S. Gollapudi, K. A. Murphy, R. G. May, and R. O. Claus, "Sapphire-fiber-based intrinsic Fabry–Perot interferometer," *Optics Letters,* vol. 17, pp. 1021-1023, 1992.

[37] M. Soeda, T. Kataoka, Y. Ishikura, S. Kimura, T. Masuda, Y. Yoshikawa, and M. Nagata, "Sapphire-based capacitive pressure sensor for high temperature and harsh environment application," in *Proceedings of IEEE Sensors*, vol. 2, pp. 950-953, 2002.

[38] M. A. Fonseca, J. M. English, M. v. Arx, and M. G. Allen, "Wireless micromachined ceramic pressure sensor for high-temperature applications," *Journal of Microelectromechanical Systems,* vol. 11, pp. 337-343, 2002.

[39] K. C. Holmes, J. L. Davidson, W. P. Kang, and A. L. Stemberg, "Diamond microelectromechanical sensors for pressure and

acceleration sensing," *Microelectromechanical Systems Conference*, pp. 45-49 2001.

Chapter 2

2 Review of Optical Fibre Sensing Technology

2.1 Introduction

As stated in Chapter 1, the main focus of this work is to design and analyse optical sensing systems capable of addressing the cross sensitivity problem that may exist in FBG for high pressure high temperature measurements, specifically for oil and gas applications. The objectives are designing sensing structures and developing theoretical models for the optical fibre sensor satisfying the requirements of the sensor interrogation differentiation of temperature and pressure measurements. In this chapter, an overview of the principles of operation of conventional pressure and temperature sensors is presented. The introduction and review of the optical fibre sensor as an alternative for measuring these parameters are presented. Fibre Bragg grating and Fabry-Perot interferometric sensors are reviewed focusing on their applications as temperature and pressure sensors respectively.

2.2 Conventional sensing technology

Generally, both temperature and pressure measurements can be achieved by determining the effect they may have on the sensing element in terms of the temperature and strain applied to this particular element. The actual temperature and pressure are then determined, and this is the general principle on which many conventional sensors are based on. In practice, every measurement involves the use of certain calibrated transducers to convert

measurable quantity into an actual value. Electric pressure sensors for example, make use of piezo-resistive materials as the sensing element. The piezo-resistive element is the calibrated transducer that converts the applied strain into an electric signal which then allows the pressure to be determined. When the piezo-resistive material is embedded onto a sensing element like a diaphragm, any strain in the diaphragm will result to a change in the material resistance which can then be measured electronically. Measurement of temperature involves the use of transducers to convert change in temperature into other measurable physical quantities, such as resistance (resistance temperature detector or RTD), electromotive force (thermocouple), displacement (bimetallic thermometer), volume expansion (liquid filled thermometer), and some other characteristics of materials that vary with temperature [1].

There are three types of pressure sensing elements; they are bellows, diaphragm and Bourdon tube (Figure 2.1).

The bellows based sensing element has many convolutions or folds, formed by several thin walled tubes that has one end sealed. The bellows is subject to a mechanical displacement when pressure is applied. This has a similar concept as that of the diaphragm membrane.

The diaphragm sensing element is a circular membrane that is attached or fabricated to the end of a fixed surface. The diaphragm will deflect when pressure or any form of mechanical strain is applied leading to a mechanical displacement of the membrane.

The Bourdon tube has a eccentric cross-section and the tube is generally bent into a C-shape or arc length of about 27 degrees. The other end or free end of

the device is sealed by a tip. It works based on the principle that the closed end straightens out when any mechanical strain or pressure is applied which results in an accurate displacement. Figure 2.1 shows the various pressure sensing elements which convert measured pressure to a mechanical displacement.

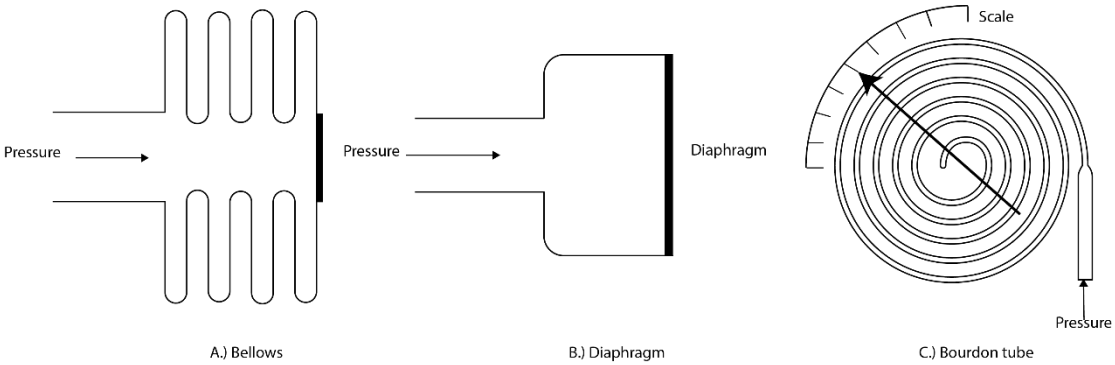

Figure 2.1 Pressure sensing elements which convert applied pressure to mechanical displacement

From Figure 2.1, once the applied pressure is converted to a mechanical displacement, there is a need to convert the mechanical displacement into an actual pressure value. There are two basic ways of achieving this actual pressure value. First, through the conversion of the mechanical displacement into an electrical signal and secondly by reading out the mechanical displacement directly through the pointer. The conversion of the mechanical displacement is usually done by a displacement sensor that changes the electrical parameters like capacitance, resistance or magnetic properties.

The displacement sensor is a capacitive sensor based on placing a pair of parallel plate capacitors side by side separated by a diaphragm that moves as

a result of the applied pressure. When pressure is applied to the sensor, the diaphragm deflects, therefore changing the spacing between the parallel plate capacitors. This results into the applied pressure being measured.

Another kind of electrical sensor is the piezoelectric sensor that generates an electric signal when strain is applied to a crystalline structure called quartz. Quartz sensors are the most common conventional sensors used in the oils and gas industry due to their high elastic modulus, high natural frequency, good linearity and low hysteresis. The various common conventional sensing mechanisms currently being deployed include resistive, capacitive, resonant etc.

2.2.1 Piezo-resistive sensor

The piezo-resistive sensor measures pressure by applying the piezo-resistive effect principle on a bonded diaphragm that serves as a strain gauge. The piezo-resistive effect is the change in resistivity of a material due to applied mechanical stress or strain. The piezo-resistive effect is present in various metal and semiconductor materials like germanium, silicon, polysilicon, silicon-carbide etc. The piezo-resistive effect is much larger than the geometrical effect in metals and semiconductors. Piezo-resistive sensors have high linearity, very good sensitivity and the output signals are very easy to retrieve. However, they suffer from thermal mismatch between the substrate and the chip which can cause large offset voltage. They also suffer surface contamination and susceptible to junction leakage.

2.2.2 Piezo-electric sensor

The piezo-electric sensor measures pressure by applying the piezo-electric effect principle which convert it to an electric potential. The piezo-electric

sensor is made up of piezo-electric ceramics and single crystal materials. The principle is based on the deformation of these materials when there is an applied pressure. The piezo-electric effect has a dynamic property that only generate an output when the input is changing. This limit the capability of the piezo-electric sensor since it can only carryout dynamic measurements.

2.2.3 Capacitive sensor

The capacitive sensor measures pressure based on the change of the capacitance of a capacitor when an external pressure is applied. A thin diaphragm serves as an electrode of the capacitor. The diaphragm has a cavity with a reference pressure on one side and the pressure is applied on the other side. As the external pressure is applied, there is a deflection on the diaphragm which cause a change in the distance between both electrodes effecting the capacitance change. The change can be in small linear range which will in turn requires amplifier and converter electronics to convert the small capacitance change to readable voltage or current output.

The major challenge of these electronic sensors is that they become extremely unreliable when deployed in harsh environments [2]. The extreme harsh environment of the reservoir, consists of strong EMI, high temperature, high pressure and a highly corrosive chemical environment put high requirements on the conventional electronic sensing system used in downhole monitoring. As such, conventional electronic sensing systems, usually fail to meet the demand. Fibre optic sensors have been developed and demonstrated to have the capabilities to solve these challenges and they have become commercially available to the oil and gas industry. However, the fibre optic sensors currently deployed in the oil and gas industry can only operate up to $150\,℃$ and even the most robust sensors are limited below $300\,℃$. Therefore, the aim of this

research is to push the limit of fibre optic sensing technology for oil and gas sensing applications by designing a sensing structure and develop theoretical equations for the system model of the optical fibre sensor satisfying the requirements of the signal processing capabilities.

2.3 Fibre optic sensing technology

Fibre optic based sensing technology has several inherent advantages which makes them very attractive for a wide range of industrial sensing applications. In recent years, the recovery of hydrocarbons is becoming more and more difficult and challenging as exploration and production operations tend to seek new frontiers into deep and ultra-deep harsh environments with approximately up to $3000\,km$ of water depth [3-6]. As the energy demand continues to rise, there is an urgent need for efficient management and optimization for production operations and systems to make this growing energy demand sustainable

The optical fibre is typically made of a cylindrical waveguide that consist of a thin core with refractive index covered by a cladding layer with a refractive index usually lower than that of the core for a single mode fibre. Optical fibres include single mode and multi-mode types. The schematic of a typical optical fibre is shown in Figure 2.2.

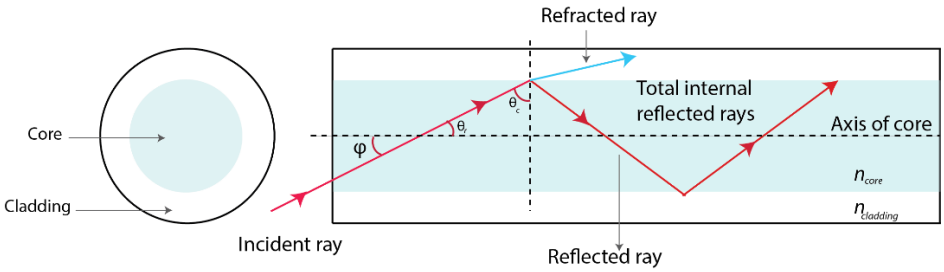

Figure 2.2 Schematic of a typical optical fibre showing propagation through internal reflection of incident light

A single mode fibre is made up of the core and cladding layers which are usually from fused silica. Light is propagated through the core of the fibre by total internal reflection (Snell's law) [3] and to achieve high refractive index, the core of the fibre is usually doped with germanium. To allow for the light energy to be maintained within the core, the refractive index of the core must be greater than that of the cladding.

Based on Snell's law, the total internal reflection occurs when light touches the interface between the core and the cladding at an angle greater than the critical angle described as [3];

$$\theta_c = \sin^{-1}\left(\frac{n_{cladding}}{n_{core}}\right) \tag{2.1}$$

where $n_{cladding}$ is the refractive index of the cladding and n_{core} is the refractive index of the core.

The schematic in Figure 2.2 shows that the incident ray at the waveguide boundary at an angle equal to or greater than the critical angle θ_c will experience total internal reflection.

From the basic principle of light propagation through an optical fibre, the light propagation changes when subjected to varying environmental conditions such as temperature and strain. By analysing the changes of the light properties through the fibre, the environmental conditions themselves can be determined. Light propagated through an optical fibre can be characterized by parameters such as intensity, phase, wavelength and polarisation. The detection of the changes of these parameters as the optical fibre interact with external perturbations can lead to the design of optical sensors capable of measuring

variety of physical parameters. As a result, fibre optic sensors can be categorised into; intensity measurement, phase (interferometric) measurement, spectral (wavelength) and polarisation modulated fibre optic sensors based on the physical quantity they measure and their effect on the electric field of the optical signal. Extensive research into the advancement of optical fibre technology for variety of applications have been ongoing for the past 30 years which have laid the technical background for the various categories and their applications are expanding rapidly. Fibre optic sensors for high pressure and high temperature measurement are theoretically analysed and designed which are relevance for this research.

Fibre optic sensors offer numerous advantages over their conventional counterparts such as immunity to EMI, operating in harsh environments, multiplexing capability, small size and light weight.

Fibre optic sensors are further divided into two subcategories; intrinsic and extrinsic sensors. For intrinsic sensors, the light is confined within the optical fibre in which the physical quantity acts on. The performance of intrinsic sensors are largely dependent on the fibre materials. While for extrinsic sensors, the light exits the fibre, gets modulated by the external perturbation like pressure or temperature and is propagated back into the fibre. The performance in this case, is largely independent of the fibre material but more dependent on the sensing element.

Propagation of light through the fibre is usually used to determine measurement information by intensity, interferometer, spectral characterisation and polarisation. In the following sections, the operation principles based on the various techniques stated above are reviewed and the most promising is further investigated and analysed.

2.3.1 Wavelength modulation based sensing

Wavelength modulation based optical sensing measures physical parameters by detecting a change in wavelength when the optical fibre interacts with the measurand. The most common type of wavelength modulated optical sensing is fibre grating sensing which is produced when the core of the fibre is exposed to an intense UV laser light that was first discovered in 1978 by Hill [7]. FBG sensors and long periodic grating sensors have since been developed based on this technique and have found many applications in measuring temperature, pressure and strain [8]. FBG sensors were developed to measure hydrostatic pressure with a typical resolution of 0.005% full scale by specially coating the grating region with different materials [9, 10]. The multiplexing capability and the zero optical power loss of the fibre grating based sensors have led to more research in this technology. However, the long term stability and reliability of this technology has been a major challenge due to the degradation of its mechanical strength and optical properties when exposed to harsh environment [11]. Also, despite the many opportunities these sensors have of replacing the conventional electronic sensors over other technologies, many concerns still exist. The issue of cross sensitivity limits the scale of this technology when used in harsh environments. For fibre grating based sensors to be used in real applications, these issues and challenges must have to be minimised. Chapter 3 of this work extensively studies the issue of cross sensitivity and how it can be minimised.

2.3.2 Intensity modulation based sensing

Intensity modulation sensing measures physical quantities based on the principle of direct detection of the change in optical power in either reflection or transmission. They are inherently simple devices where light from an optical

source is propagated through the fibre and the intensity is altered at the transducer which is then returned to an optical detector. The light intensity detected by the detector is a function of the physical quantity measured. There are three different classes of intensity modulation based sensing as shown in Figure 2.3. They are transmission intensity, reflection intensity and micro bending intensity [9].

Intensity modulated based sensors made with multimode fibre optic micro-bend have successfully been commercialized. It is based on the operating principle in which the mechanical periodic micro-bend coupled the energy of both the radiation and guided modes thereby resulting in the attenuation of the transmitted light. Sensor configuration can be design and constructed in such a way that the mechanical micro-bending device transfer the applied perturbation to the optical intensity change. The micro-bend modulated sensors have been reported to have good performance characteristic like good resolution, however, the fluctuation of the light source and large hysteresis posed limit to their accuracy [12]. Moreover, the large size of the micro-bending device makes it very difficult to be applied in many sensing applications.

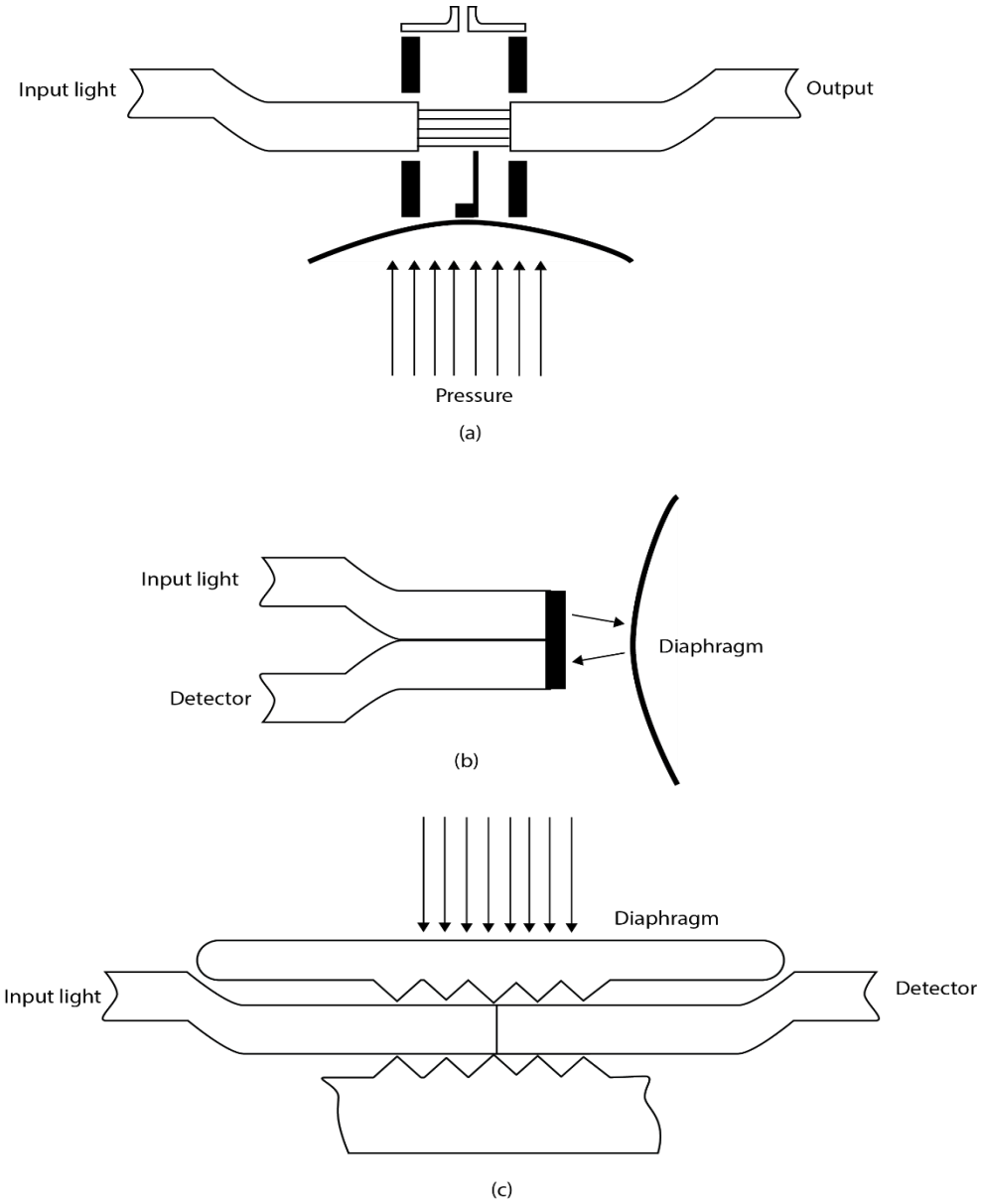

Figure 2.3 Intensity modulated based sensing class; (a) Transmission intensity (b) Reflection intensity (c) micro-bending intensity type

2.3.3 Interferometric modulation based sensing

Phase modulated sensing uses the interferometric mechanisms such as the Mach-Zehnder, Michelson, Sagnac and Fabry-Perot to measure physical parameters see Figure 2.4. It works based on the principle of constructive interference by observing the change in interference between two light beams. The interferometric modulation based sensing has become a very useful tool

for high precision sensing, optical spectrum analysis, construction of lasers and optical wavelength filtering [13]. This sensing technique uses the interference between two parallel beams propagated through different optical paths or fibre. It relies on the change in the cavity length of one of the interference arms. The cavity length change can be as a result of either the refractive index change or the change in fibre length. The different types of interferometric based sensing have slightly varying sensing mechanism.

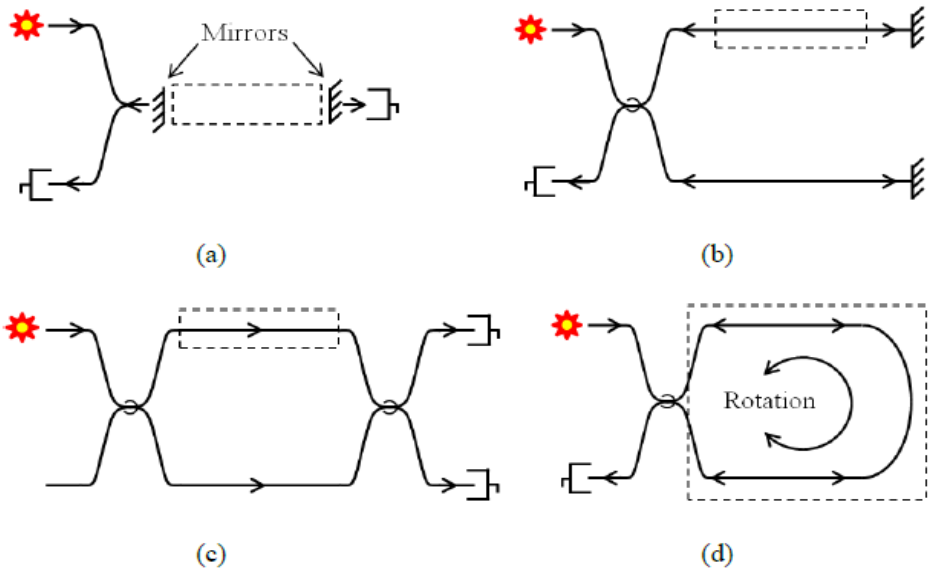

Figure 2.4 Phase modulated sensing uses the interferometric techniques (a) Fabry-Perot interferometer (b) Michelson interferometer (c) Mach-Zehnder interferometer and (d) Sagnac interferometer

The Fabry-Perot interferometer is generally designed to measure physical parameters through a formation of a cavity having two parallel reflective surfaces. When light is propagated through the Fabry-Perot cavity, multiple interference of light is formed caused by the multiple reflections between the two reflective surfaces. The Fabry-Perot interferometer is subdivided into two

categories, intrinsic Fabry-Perot interferometer (IFPI) and extrinsic Fabry-Perot interferometer (EFPI). In IFPI, the light is confined and modulated within the fibre. The cavity length and modulation are formed within the fibre. In EFPI, the light exits the fibre and is modulated before being propagated back into the fibre. The cavity length is formed outside of the fibre and the fibre serves as the medium for transmitting light into and out of the Fabry-Perot cavity. Different configurations for FPI have been proposed and developed. One configuration is to place a different fibre aligned to the first one which form a cavity between them and then packaged using a glass or silica, see Figure 2.5. An alternative method is the use of diaphragm at the opposite side of the fibre end forming a cavity. Any change in the cavity length due to the deformation of the diaphragm would result in changes in interference.

The IFPI is usually fabricated by splicing a special fibre and coating the two end-faces with a reflective film. The output signal is generated by the superposition of the multiple reflections at the end-faces of the special fibre. These reflections are as a result of the reflectance of the coating, the cavity and the refractive index of the fibre. Whenever there is a change in the cavity length or the refractive index, the interference output can be tracked thereby able to measure any physical quantity that caused the changes of the optical properties.

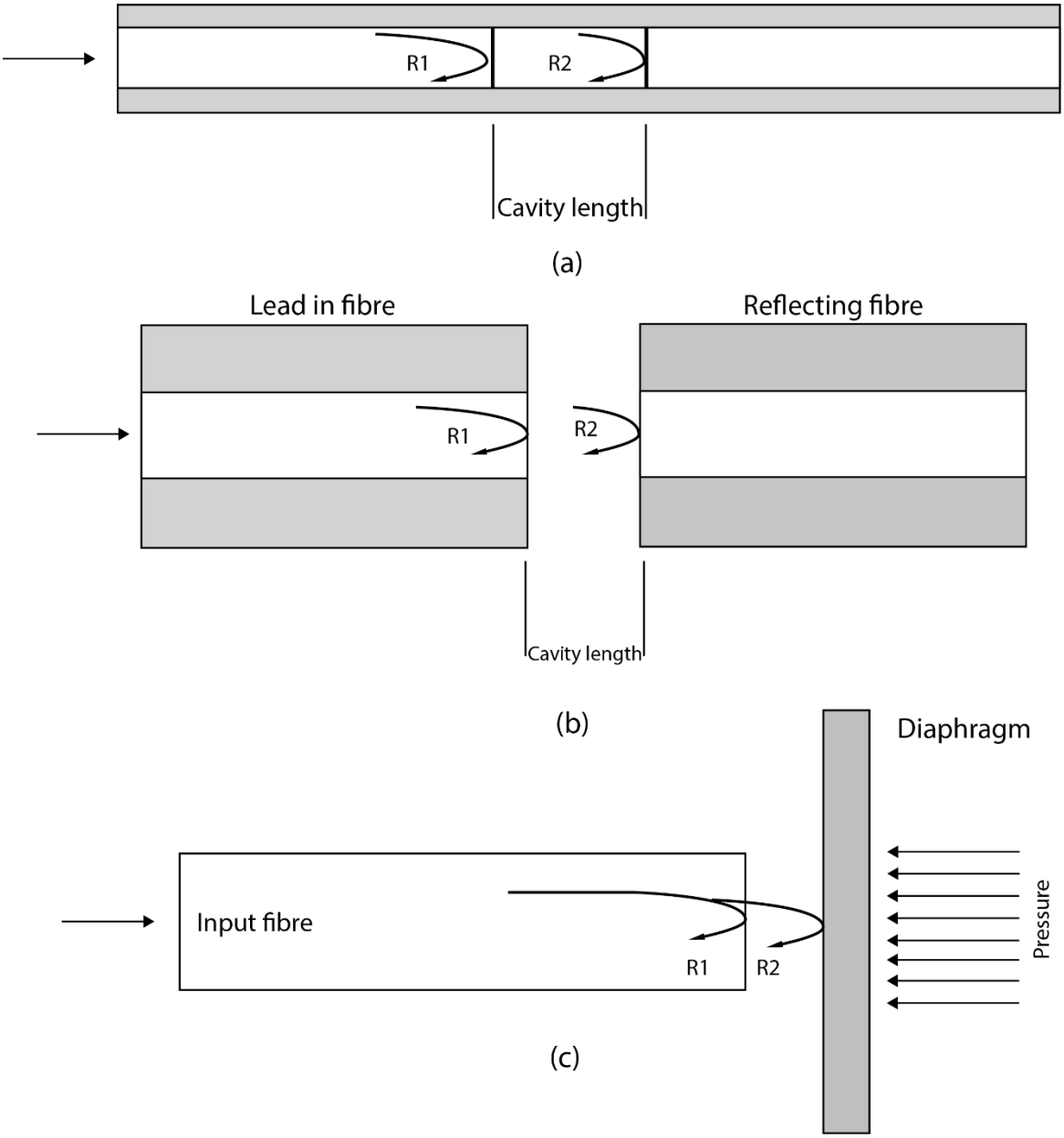

Figure 2.5 Different Fabry-Perot configurations (a) Illustration of IFPI formed with a single optical fibre (b) Arrangement of an EFPI formed using two optical fibres and (c) Schematic of a FP cavity formed using an optical fibre as the lead-in fibre and a deformable diaphragm.

In EFPI, the performance of the sensor depends only on the sensing element which gives it the flexibility to adapt to various sensing applications. An EFPI cavity is formed by placing an input fibre side by side to a reflecting fibre. As

light is propagated through the input fibre, a fraction of it is reflected back as *R1*, and all others are transmitted into the cavity space to the reflected fibre end-face. Part of the transmitted light are also reflected back as *R2* at the end-face of the reflected fibre which is then recoupled into the input fibre.

EFPI sensors have been developed and are commercially available. The EFPI sensors have many advantages over the Mach-Zehnder and Michelson sensors such as their high sensitivity, small size, good flexibility, and their simple structures. These make them very attractive for various sensing applications. However, the EFPI have the potential of having low coupling efficiency due to the usual misalignment of the reflecting fibre.

2.3.4 Polarization modulation based sensing

Polarization modulated sensing is based on the principle of photo-elastic effect and the Faraday's effect. Photo-elastic fibre sensors are designed in such a way that the applied pressure is transferred through photo-elastic effect into the change in polarization property of the optical fibre or medium [14]. While the sensors based on Faraday's effect measure both electric and magnetic field. Measurement based on Faraday's effect have found applications in electric current measurements. Optical sensors based on photo-elastic effect was first introduced in 1982 by Spillman [14]. After then, many sensing applications based on photo-elastic effect have been developed and reported to help solved the challenge of compensation for the power variation [15]. Silica and glass fibres show weak photo-elastic effect, however, external crystals are used as better sensing element for more accurate measurements.

2.3.5 Fibre Bragg grating sensors

A fibre Bragg grating (FBG) is simply produced from a standard single mode optical fibre. The core of the fibre is expose to two ultra-violet light beams originating from the same laser source, the UV light beams constructively and destructively interfere. The result is a grating sensor recorded into the fibre formed as the periodic variation of the refractive index of the fibre core as shown in Figure 2.6. When light is propagated into the fibre, a narrow waveband of light is reflected back at the grating while other wavelengths of light are transmitted, see Figure 2.7. The wavelength of the reflected light varies with the period of the grating which itself varies with both strain and temperature. The central wavelength of reflected signal is generally called the Bragg wavelength (λ_B) and it has a linear relationship between the refractive index and the period of the grating $\lambda_B = 2n_{eff}\Lambda$. This means that any variation in strain and temperature to which the optical fibre is subjected to can cause a shift in the Bragg wavelength. The effective refractive index is n_{eff} is a physical characteristic of the fibre optic material in which the grating is formed, while

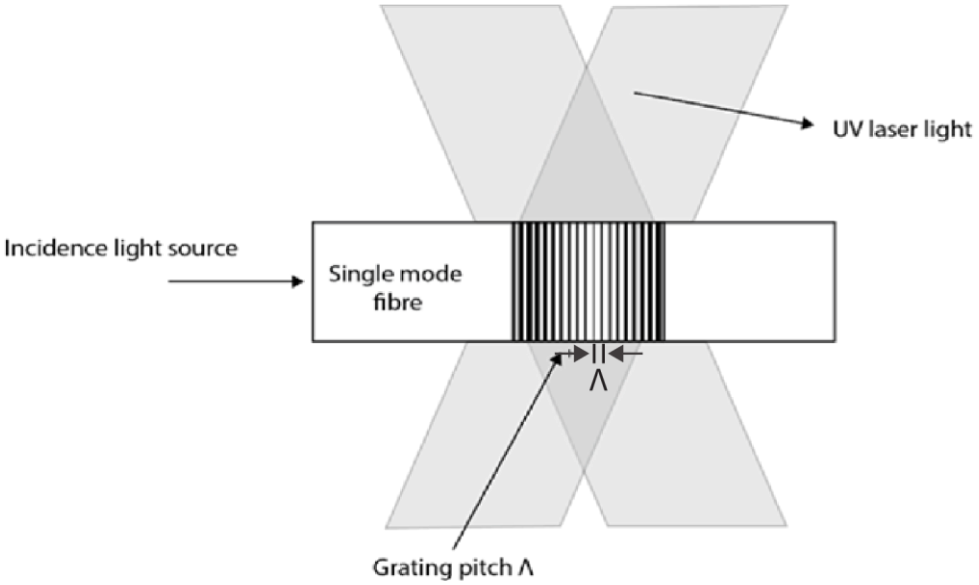

Figure 2.6 Refractive index change of fibre Bragg grating

the grating period Λ depends on the design of the grating. The changes in temperature and applied strain on the grating of the fibre directly modify the refractive index or the grating period of the fibre respectively.

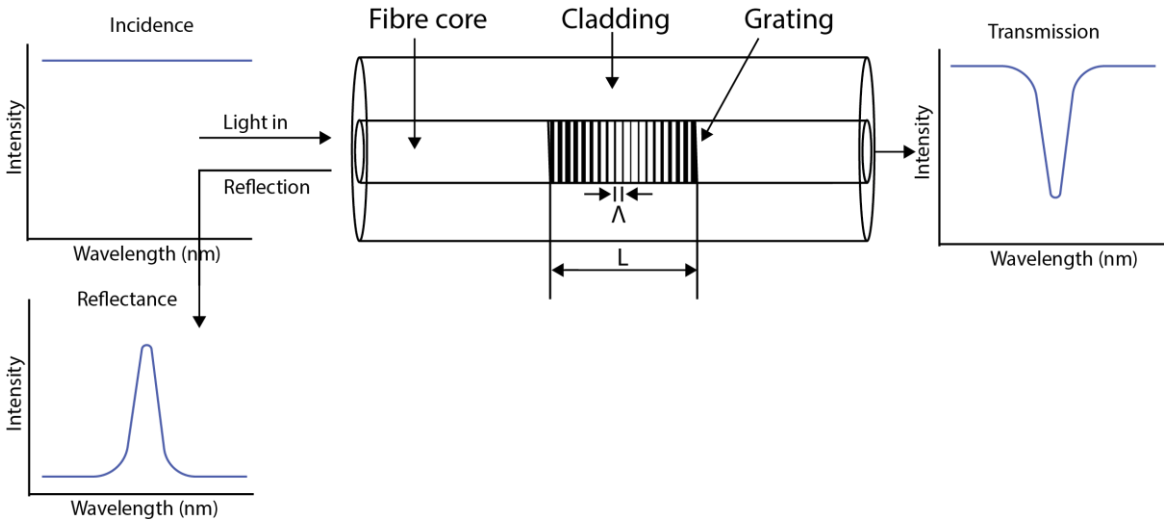

Figure 2.7 Schematic of FBG and its reflection and transmission properties

These simple principles had made it possible for the various advancement of the FBG sensing technology and also take advantage of the multiplexing capability of an FBG. See Figure 2.8.

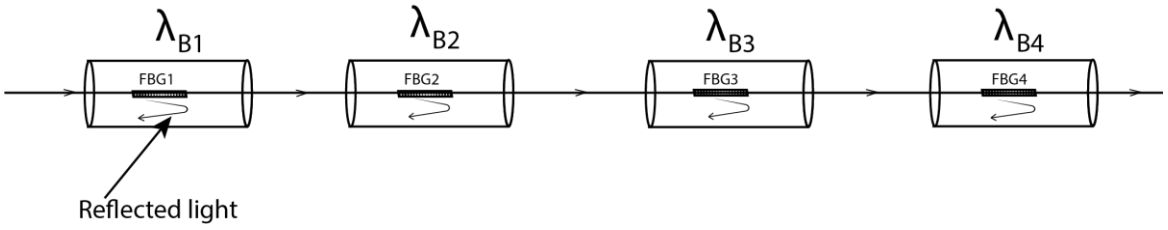

Figure 2.8 Multipoint distributed (WDM) pointing sensing based on FBG

The nature of the output of Bragg gratings provide these sensors with a built-in self-referencing capability. As the sensed information is encoded directly into wavelength, which is an absolute parameter, the output does not

depend directly on the total light levels, losses in the connecting fibres and couplers, or source power. This is widely acknowledged as one of the most important advantages of these sensors. The wavelength encoded nature of the output, however, also facilitates wavelength division multiplexing by allowing each sensor to be assigned to a different "slice" of the available source spectrum. This enables quasi-distributed sensing of strain, temperature, or potentially other measurands by associating each spectral slice with a particular spatial location. The concept is illustrated in Figure 2.8. The upper limit to the number of gratings which can be addressed in this way is a function of the source profile width and the operational wavelength bandwidth required for each grating element.

A FBG sensor is primarily composed of three main segments; the sensing part, which compose of the bare FBG that does the actual sensing, the packaging and the FBG arrays; the instrumentation which composed of the interrogating instruments and related component such as the switches, multiplexors, data acquisition system, data processing units, software and graphical user interface; and the system integration unit which compose of project management and engineering aspects [16].

When FBG was first demonstrated in 1978 by Hill, They observed photosensitivity of the optical fibre when exposing the germanium doped fibre core to the two coherent argon-ion laser counter propagating radiation with $488\ nm$ wavelength. The result showed a periodic change in the refractive index similar to the periodic pattern of the interference wave of the laser. Both the reflected light from the grating and the writing laser have the same wavelength. This limit the capability of this techniques. About 10 years later, Meltz et al

[17] in 1989 presented a holographic technique to address that limitation by using a writing wavelength of $244\,nm$ $(5\,eV)$ that made it possible to write gratings with wavelength other than the wavelength of the writing laser. They observed that photosensitivity was a two photon-process that could be made more efficient if it were a one-photon process corresponding to the germania oxygen vacancy defect band. The transverse holographic technique was successful since the fibre cladding is transparent to UV radiation, while the fibre core is highly absorbing to this radiation.

One of the major advantages of the fibre grating fabrication by intersecting the two interfering beams at an angle is the fact that many custom Bragg grating fabrication can be done having much longer wavelengths than the writing wavelength. After the pioneering work by Hill and Meltz, the couple mode theory [18] has been developed to analyse the spectral properties of fibre Brag grating by Erdogan *et al* [19]. Lemaire in 1993 [20] proposed the use of Hydrogen loading technique to improve the optical fibre photosensitivity prior to laser irradiation. This method of Hydrogen diffusion enabled the core to be more susceptible to UV laser radiation. Refractive index change of the order of 10^{-2} had also been achieved through this method. In 1993, a phase mask technique [21] was developed that successfully supersedes the success of the transverse holographic method by Meltz. Phase mask is made up of a thin slab of silica glass etched using photolithographic technique. This material is transparent to the UV radiation which makes the phase mask to diffract the light into 0, -1 and +1 diffraction order. By carefully controlling the phase mask corrugations reduces the zero-order diffraction, allowing the +1/-1 diffraction to interfere and produce the pattern of the laser radiation to enable the Bragg grating to be printed in the core of the fibre. In 1995, Othonos [22]

demonstrated an improvement in the coherence of the writings by relaxing the need for a close contact. The phase mask made the manufacturing of FBG very simple through easier alignment, lowering the coherence demand on the laser beams and reduction in the stability requirements on the imprinting device. The ability of manufacturing high performance Bragg grating at low cost is key to the large scale use cases of this technique in optical sensing applications. However, this technique relies on the use of separate phase mask for the production of each gratings for different operating wavelength.

Recently, many fibre optic sensors are made with FBG through the modulation of the refractive index profiles. Different types of FBG have been reported based on their coupling characteristics. First, short period grating FBG [7]. Here, the grating period is typical within the range of $0.22 - 0.54\,\mu m$ with the light coupled into the backward propagation direction. Second, tilted period grating [23, 24]. When the fringes of the short period grating is tilted by an angle a tilted period grating is formed. The light with the tilted signal can also be coupled into the backward propagation direction. Lastly, the long period grating [25, 26]. The grating period of the long period grating has a length within the range of $100 - 500\ \mu m$ with the light coupled into the forward propagation direction. They act as loss filters and are usually used as gain equalizer. They have been successfully manufactured by exposing the core of the fibre to point by point UV light. Other examples include chirped FBG, apodized FBG and phase shift FBG [27-29]

2.3.5.1 Sensing principle of FBG for temperature and strain

A change in temperature or strain acts directly to the centre wavelength of the grating causing a shift to the effect of the change. By measuring this shift in Bragg wavelength it is possible to determine the variation in temperature or strain applied to the grating of the fibre. The expression for this definition is given as [31]

$$\frac{\Delta\lambda_B}{\lambda_B} = K_\varepsilon \Delta\varepsilon + K_T \Delta T \qquad (2.2)$$

where $\Delta\lambda_B/\lambda_B$ is the normalised Bragg wavelength change of the FBG, $\Delta\varepsilon$ and ΔT are the change in both strain and temperature, K_ε is the strain effect and K_T is the temperature sensitivity on the FBG. The K_ε and K_T parameters are constant for wide range of values and Equation 2.2 can be re-written as [31]

$$\frac{\Delta\lambda_B}{\lambda_B} = (1 - P_e)\Delta\varepsilon + (\alpha + \xi)\Delta T \qquad (2.3)$$

where P_e is the elasto-optic coefficient, α is the coefficient of thermal expansion and ξ is the thermo-optic coefficient.

The FBG is sensitive to both strain and temperature, in most practical applications, it's very common to compensate for the temperature so that the effects of coefficient of thermal expansion and temperature on the refractive index can be determined. For low range of temperature, the temperature sensitivity is approximately 10×10^{-6} /℃ while the strain sensitivity is 0.80 for a fixed Bragg wavelength of $1550\,nm$.

In deep and ultra-deep environments, temperature information is one of the key parameters to measure for oil and gas well and structural health monitoring. In deep wells, it is necessary to monitor temperature and the temperature sensors have to be properly coated and packaged to maintain accurate stability in these environments over a long period of time. FBGs have been have been employed as the sensor of choice for multi-parameter measurement by detecting the reflected wavelength information [32-34]. The change in the reflected and transmitted optical spectra can be used in interrogating the physical parameters [35, 36]. Several techniques have been developed over the years to improve the performance of FBG based temperature sensing in high temperature environments. Some of these methods include thermal cycling, annealing of the gratings [37, 38], and fabricating gratings using femtosecond laser [39, 40]. However, when FBGs are written in a polarization maintaining fibre, two different resonant wavelengths are seen and two orthogonal polarized modes will propagate the core of the fibre [41-43]. Measurements of high temperature with optical fibre sensors have been realised, however, researchers are still seeking new methods of simplifying the fabrication process and reduce the cost of production. One of the major concerns for deploying fibre gratings sensors in the oil and gas industry is their thermal instability in high temperature environments, especially for downhole measurements. The capability of the FBG sensor as a high temperature sensor is mainly limited by the thermal stability of the refractive index modulation [44]. Alternatively, metal coated FBG sensors have become very popular techniques for improving the performance of optical sensors for harsh environments [45, 46]. These make

them highly suitable for oil and gas sensing applications. FBG sensors have become mainstream sensors for oil and gas sensing applications leading to the demand for better optical based sensors. In chapter 5 of this work, we introduce the design and analysis a metal coated hybrid sensor for high pressure high temperature measurement. The characterization of this sensor could provide insight into development of other more optimised sensing structure for oil and gas applications.

2.3.5.2 Sensing principle of FBG for pressure measurement

Fibre optic pressure sensors for downhole measurement have been proposed and developed [30]. Measurement of pressure is based on the principle of a shift in wavelength of an FBG when the grating length or the refractive index changes. The measurement of pressure by FBG was first demonstrated in 1993 by Xu *et al* [47]. He showed experimentally a pressure sensitivity of $-3.04 \times 10^{-3}\, nm/MPa$ which is equivalent to pressure resolution of $328.9\, kPa$ over a pressure range of 70 MPa with a bare FBG of central wavelength of $1553.3\, nm$ was achievable on a single mode optical fibre. Though this simple technique was capable of developing low pressure sensors, it was limited for downhole pressure measurements because of its low intrinsic pressure sensitivity and low mechanical strength. FBG sensors capable in operating at harsh environments need their structure to be properly coated and packaged to improve sensitivity and mechanical protection. Several techniques for enhancing pressure sensitivity have been studied and reported.

Zhang $et\ al$ [48] proposed a technique that increased pressure sensitivity by 3 order of magnitude. He did this by embedding an FBG in a polymer filled metal jacket with a small aperture at the end. The applied pressure in the longitudinal

axial direction of the fibre imposed an axial compression of the polymer and the optical fibre.

In 2000, Liu *et al* [49] demonstrated both theoretically and experimentally that coating the FBG sensor with two different polymers allows for an increase in pressure sensitivity upto 30 times and temperature of 8 times that of bare FBG. The measured pressure sensitivity and temperature sensitivity for a Bragg wavelength shift of 1540.2 nm were $-5.24 \times 10^{-5}\, MPa^{-1}$ and $5.69 \times 10^{-5}\, ℃^{-1}$ respectively.

Sheng *et al* [50] developed an all fibre highly sensitive sensor based on FBG encapsulated in a half filled metal tube with a round plate attached to the FBG and polymer. The polymer was pressurized along one radial direction only, and responds to an axial force on the round plate, creating an axial stretched-strain on the FBG. The measured pressure sensitivity was measured to be $2.2 \times 10^{-2} MPa^{-1}$ which was $10\,900$ times higher than the bare FBG. Another FBG sensor configuration was reported by Ho *et al* in 2008 [51], where they proposed an FBG based pressure sensor attached on a surface of a thin circular plate. The pressure experienced by the circular plate is correlated to the difference in central wavelength of $1550\, nm$ and measured pressure sensitivity of $4.0 \times 10^{-3}\, MPa^{-1}$.

2.4 Summary

In this chapter, a review of the principles of operation of conventional pressure and temperature sensors was presented in order to ascertain that the current solutions available in the industry are not sufficient in meeting the goals of this research. The introduction and review of optical fibre sensor as an alternative for measuring such parameters were also presented. Wavelength, intensity, interferometric and polarization modulation based sensing were described.

Lastly the sensing principles of FBG for temperature, strain and pressure were detailed. This provided different design and measurement techniques from which the most practical ones were considered for the solution of addressing the cross sensitivity problem. Together these studies provide important insights into the development of other more optimised sensing structure for oil and gas applications.

2.5 References

[1] G. Fowles, I. o. Measurement, and Control, *Flow, Level and Pressure Measurement in the Water Industry*: Butterworth-Heinemann, 1993.

[2] P. M. Nellen, P. Mauron, A. Frank, U. Sennhauser, K. Bohnert, P. Pequignot, P. Bodor, and H. Brändle, "Reliability of fiber Bragg grating based sensors for downhole applications," *Sensors and Actuators A: Physical,* vol. 103, pp. 364-376, 2003.

[3] A. D. Kersey, "Optical fiber sensors for permanent downwell monitoring applications in the oil and gas industry," *IEICE Trans. Electron,* vol. 3, pp. 400 - 404, 2000.

[4] E. Hecht, *Optics*: Pearson, 2014.

[5] S. J. Mihailov, "Fiber Bragg Grating Sensors for Harsh Environments," *Sensors,* vol. 12, 2012.

[6] D. Grobnic, S. J. Mihailov, C. W. Smelser, and D. Huimin, "Sapphire fiber Bragg grating sensor made using femtosecond laser radiation for ultrahigh temperature applications," *IEEE Photonics Technology Letters,* vol. 16, pp. 2505-2507, 2004.

[7] K. O. Hill, Y. Fujii, D. C. Johnson, and B. S. Kawasaki, "Photosensitivity in optical fiber waveguides: Application to reflection filter fabrication," *Applied Physics Letters,* vol. 32, pp. 647-649, 1978.

[8] A. Arie, B. Lissak, and M. Tur, "Static Fiber-Bragg Grating Strain Sensing Using Frequency-Locked Lasers," *Journal of Lightwave Technology,* vol. 17, p. 1849, 1999.

[9] M. G. Xu, H. Geiger, and J. P. Dakin, "Fibre grating pressure sensor with enhanced sensitivity using a glass-bubble housing," *Electronics Letters,* vol. 32, pp. 128-129, 1996.

[10] D. J. Hill and G. A. Cranch, "Gain in hydrostatic pressure sensitivity of coated fibre Bragg grating," *Electronics Letters,* vol. 35, pp. 1268-1269, 1999.

[11] U. Sennhauser, A. Frank, P. Mauron, and P. M. Nellen, "Reliability of optical fiber Bragg grating sensors at elevated temperature," *IEEE International Reliability Physics Symposium Proceedings. 38th Annual*, pp. 264-269, 2000.

[12] J. W. Berthold, "Historical review of microbend fiber-optic sensors," *Journal of Lightwave Technology,* vol. 13, pp. 1193-1199, 1995.

[13] S. Yin and F. T. S. Yu, *Fiber Optic Sensors*: CRC Press, 2002.

[14] W. B. Spillman, "Multimode fiber-optic pressure sensor based on the photoelastic effect," *Optics Letters,* vol. 7, pp. 388-390, 1982.

[15] I. P. Giles, S. McNeill, and B. Culshaw, "A stable remote intensity based optical fiber sensor," *Journal of Physics E: Scientific Instruments,* vol. 18, p. 502, 1985.

[16] A. Méndez, "Fiber Bragg grating sensors: a market overview," 2007, pp. 661905-661906.

[17] G. Meltz, W. W. Morey, and W. H. Glenn, "Formation of Bragg gratings in optical fibers by a transverse holographic method," *Optics Letters,* vol. 14, pp. 823-825, 1989.

[18] A. Yariv, "Coupled-mode theory for guided-wave optics," *IEEE Journal of Quantum Electronics,* vol. 9, pp. 919-933, 1973.

[19] T. Erdogan, "Fiber grating spectra," *Journal of Lightwave Technology,* vol. 15, pp. 1277-1294, 1997.

[20] P. J. Lemaire, R. M. Atkins, V. Mizrahi, and W. A. Reed, "High pressure H_2 loading as a technique for achieving ultrahigh UV photosensitivity and thermal sensitivity in GeO_2 doped optical fibres," *Electronics Letters,* vol. 29, pp. 1191-1193, 1993.

[21] K. O. Hill, B. Malo, F. Bilodeau, D. C. Johnson, and J. Albert, "Bragg gratings fabricated in monomode photosensitive optical fiber by UV exposure through a phase mask," *Applied Physics Letters,* vol. 62, pp. 1035-1037, 1993.

[22] A. Othonos and L. Xavier, "Novel and improved methods of writing Bragg gratings with phase masks," *IEEE Photonics Technology Letters,* vol. 7, pp. 1183-1185, 1995.

[23] I. Riant, "UV-photoinduced fibre gratings for gain equalisation," *Optical Fiber Technology,* vol. 8, pp. 171-194, 2002.

[24] T. Erdogan and J. E. Sipe, "Tilted fiber phase gratings," *Journal of the Optical Society of America A,* vol. 13, pp. 296-313, 1996.

[25] A. M. Vengsarkar, P. J. Lemaire, J. B. Judkins, V. Bhatia, T. Erdogan, and J. E. Sipe, "Long-period fiber gratings as band-rejection filters," *Journal of Lightwave Technology,* vol. 14, pp. 58-65, 1996.

[26] B. J. Eggleton, P. A. Krug, L. Poladian, and F. Ouellette, "Long periodic superstructure Bragg gratings in optical fibres," *Electronics Letters,* vol. 30, pp. 1620-1622, 1994.

[27] B. Malo, S. Theriault, D. C. Johnson, F. Bilodeau, J. Albert, and K. O. Hill, "Apodised in-fibre Bragg grating reflectors photoimprinted using a phase mask," *Electronics Letters,* vol. 31, pp. 223-225, 1995.

[28] J. E. Sipe, L. Poladian, and C. M. de Sterke, "Propagation through nonuniform grating structures," *Journal of the Optical Society of America A,* vol. 11, pp. 1307-1320, 1994.

[29] W. H. Loh and R. I. Laming, "1.55 μm phase-shifted distributed feedback fibre laser," *Electronics Letters,* vol. 31, pp. 1440-1442, 1995.

[31] A. Othonos and K. Kalli, *Fiber Bragg Gratings: Fundamentals and Applications in Telecommunications and Sensing*: Artech House, 1999.

[32] C.-L. Zhao, M. S. Demokan, W. Jin, and L. Xiao, "A cheap and practical FBG temperature sensor utilizing a long-period grating in a photonic crystal fiber," *Optics Communications,* vol. 276, pp. 242-245, 2007.

[33] L. Liu, H. Zhang, Q. Zhao, Y. Liu, and F. Li, "Temperature-independent FBG pressure sensor with high sensitivity," *Optical Fiber Technology,* vol. 13, pp. 78-80, 2007.

[34] N. Takahashi, K. Tetsumura, and S. Takahashi, "Multipoint detection of an acoustic wave in water with a WDM fiber-Bragg-grating sensor," 1999, pp. 270-273.

[35] H. K. Bal, F. Sidiroglou, Z. Brodzeli, S. A. Wade, G. W. Baxter, and S. F. Collins, "Temperature independent bend measurement using a pi-

phase shifted FBG at twice the Bragg wavelength," pp. 76530H-76530H-4, 2010.

[36] L. Zhang, Y. Liu, J. A. R. Williams, and I. Bennion, "Enhanced FBG strain sensing multiplexing capacity using combination of intensity and wavelength dual-coding technique," *IEEE Photonics Technology Letters,* vol. 11, pp. 1638-1640, 1999.

[37] S. K. Abi Kaed Bey, T. Sun, and K. T. V. Grattan, "Optimization of a long-period grating-based Mach–Zehnder interferometer for temperature measurement," *Optics Communications,* vol. 272, pp. 15-21, 2007.

[38] R. Joseph, N. K. Viswanathan, S. Asokan, K. V. Madhav, and B. Srinivasan, "Predicting thermal stability of fibre Bragg gratings - isothermal annealing within isochronal annealing," *Electronics Letters,* vol. 43, pp. 1341-1342, 2007.

[39] S. J. Mihailov, D. Grobnic, R. B. Walker, H. Ding, F. Bilodeau, and C. W. Smelser, "Femtosecond laser inscribed high temperature fiber Bragg grating sensors," pp. 677009-677009-13, 2007.

[40] G. D. Marshall and M. J. Withford, "Annealing Properties of Femtosecond Laser Inscribed Point-by-Point Fiber Bragg Gratings," in *Bragg Gratings, Photosensitivity, and Poling in Glass Waveguides*, Quebec City, p. JWA30, 2007.

[41] Z. Liu, Y. G. Liu, J. Du, S. Yuan, and X. Dong, "Switchable triple-wavelength erbium-doped fiber laser using a single fiber Bragg grating in polarization-maintaining fiber," *Optics Communications,* vol. 279, pp. 168-172, 2007.

[42] H. Kyung Jun, L. Yong Wook, K. Jaejoong, R. Sookyoung, J. Jaehoon, and L. Byoungho, "Simultaneous measurement of strain and temperature incorporating a long-period fiber grating inscribed on a polarization-maintaining fiber," *IEEE Photonics Technology Letters,* vol. 16, pp. 2114-2116, 2004.

[43] Y. Chen-Chun, E. S. Stephen, W. J. Stephen, and P. T. Ralph, "A polarization-maintaining fibre Bragg grating interrogation system for multi-axis strain sensing," *Measurement Science and Technology,* vol. 13, p. 1446, 2002.

[44] D. Grobnic, C. W. Smelser, S. J. Mihailov, and R. B. Walker, "Long-term thermal stability tests at 1000 °C of silica fibre Bragg gratings made with ultrafast laser radiation," *Measurement Science and Technology,* vol. 17, p. 1009, 2006.

[45] X. Li and F. Prinz, "Embedded Fiber Bragg Grating Sensors in Polymer Structures Fabricated by Layered Manufacturing," *Journal of Manufacturing Processes,* vol. 5, pp. 78-86, 2003.

[46] L. Xiao Chun, P. Fritz, and S. John, "Thermal behavior of a metal embedded fiber Bragg grating sensor," *Smart Materials and Structures,* vol. 10, p. 575, 2001.

[47] M. G. Xu, L. Reekie, Y. T. Chow, and J. P. Dakin, "Optical in-fibre grating high pressure sensor," *Electronics Letters,* vol. 29, pp. 398-399, 1993.

[48] Z. Ying, F. Dejun, L. Zhiguo, G. Zhuanyun, D. Xiaoyi, K. S. Chiang, and B. C. B. Chu, "High-sensitivity pressure sensor using a shielded polymer-coated fiber Bragg grating," *IEEE Photonics Technology Letters,* vol. 13, pp. 618-619, 2001.

[49] L. Yunqi, G. Zhuanyun, Z. Ying, C. Kin Seng, and D. Xiaoyi, "Simultaneous pressure and temperature measurement with polymer-coated fibre Bragg grating," *Electronics Letters,* vol. 36, pp. 564-566, 2000.

[50] H. J. Sheng, F. Ming-Yue, C. Tzu-Chiang, L. Wen-Fung, and B. Sheau-Shong, "A lateral pressure sensor using a fiber Bragg grating," *IEEE Photonics Technology Letters,* vol. 16, pp. 1146-1148, 2004.

[51] H. Yen-Te, H. An-Bin, and L. Jui-ting, "Development of a chirped/differential optical fiber Bragg grating pressure sensor," *Measurement Science and Technology,* vol. 19, p. 045304, 2008.

Chapter 3

3 Theoretical Analysis of Fibre Bragg Gratings

3.1 Introduction

The implementation and application of the hybrid optical fibre sensor need a detailed level of understanding of the optical properties which gives rise to various existing phenomena that can be considered for sensing. This chapter establishes the mathematical model of FBG, introduces a numerical method for carrying out FBG response simulation when affected by external perturbations (like pressure, temperature and strain). It also shows the effect of changes relating to the parameters of FBG caused by these external perturbations. Modelling, simulation and characterization of optical FBG for oil and gas sensing applications are presented. The grating length and refractive index profile are key parameters for effective and high performance optical Bragg grating. Modelling and simulation of the Bragg grating which are based on solving the coupled-mode theory (CMT) equation by using the transfer matrix method were carried out using MATLAB.

The fundamental equations required for the theoretical understanding of FBG are presented in this chapter, thus providing a complete background of FBG and its characterization in optical fibres. The spectral reflectivity, bandwidth and side-lobes were analysed with changes in grating length and refractive index and results show that the changes in grating length and refractive index profile affect the bandwidth as the demand for bandwidth and high-speed transmission grows in oil and gas sensing applications. Finally, sensitivity and

cross sensitivity behaviours of FBG are analysed and presented including the various derivations of their mathematical models.

3.2 Properties and Principles of FBG Sensing

FBG can be constructed to a distributed based sensing whose characteristics are wavelength dependent that can accurately be adjusted by proper design. One important feature of the FBG is the relative narrow bandwidth of the reflection spectrum [1]. However, some certain applications such as seismic sensing in the oil and gas industry need large bandwidth [2]. Applying the CMT in this chapter, a short grating length is needed to achieve a large bandwidth and it was also found that the refractive index change will also affect the bandwidth.

The refractive index profile, grating length and the grating strength are basically the three variables that control the properties FBGs. The properties that need to be controlled in an FBG are reflectivity, bandwidth and the side-lobe strength. Parameters like strain, temperature and pressure simultaneously act on FBG sensor [3]. The Bragg wavelength of the FBG will vary with changes in any of these parameters experienced by the fibre optic sensor and the corresponding wavelength shifts are as follows:

3.2.1 Strain and temperature sensing of FBG

The equation models of FBG are derived from both the grating period and refractive index properties of the FBG when subjected to external perturbations [3]. The Bragg wavelength is sensitive to physical changes in the grating due to strain and temperature [3]. Thermal expansion in the FBG causes the effective refractive index and the spacing of the gratings to change simultaneously and produced a wavelength shift. While the temperature

sensitivity of FBG happens as a result of the induced refractive index change due the coefficient of thermal expansion of the optical fibre. The shift in Bragg wavelength $\Delta\lambda_B$ due to the applied longitudinal strain and temperature change is given by [3];

$$\frac{\Delta\lambda_B}{\lambda_B} = (1 - P_e)\Delta\varepsilon + (\alpha + \xi)\Delta T \tag{3.1}$$

where $\Delta\lambda_B$ wavelength difference compared to original Bragg wavelength, λ_B. P_e is the effective photo-elastic constant, ε is the strain applied to the optical fiber, α is thermal coefficient and ξ is the thermo-optic coefficient. Therefore, the strain effect on an optical fiber under a constant temperature $(\Delta T = 0)$, the Bragg wavelength shift $\Delta\lambda_B$ can be expressed in the form [3];

$$\Delta\lambda_{B|S} = \lambda_B(1 - P_e)\varepsilon \tag{3.2}$$

The linear change of the strain or pressure results in variation of FBG central wavelength defined as [3];

$$P_e = \frac{n_{eff}^2}{2}[P_{12} - \nu(P_{11} + P_{12})] \tag{3.3}$$

where $P_{11} = 0.113$ and $P_{12} = 0.252$ are the components of the fibre optic strain tensor also known as the Pockels constants of the fibre, determined experimentally [4] and ν is the Poisson's ratio (which is defined as the ratio of

transverse strain to longitudinal strain in the direction of stretching force). For a typical germanosilicate optical fibre, $\nu = 0.16$, and $n_{eff} = 1.482$. Study has shown that the strain sensitivity is given as $1.2\,pm/\mu\varepsilon$ at a wavelength of $1550\,nm$, corresponding to a change of $1.2\,pm$ for applying a strain of $1\,\mu\varepsilon$ to the fibre grating [3]. An example of a Bragg wavelength shift with applied strain on a $1548.20\,nm$ gratings is shown in Figure 3.1. This shows the variation of the wavelength of FBG versus applied. The variation pattern is linear and the slope is 1.2×10^{-3} and the fitting linear correlation coefficient reached 97.29%

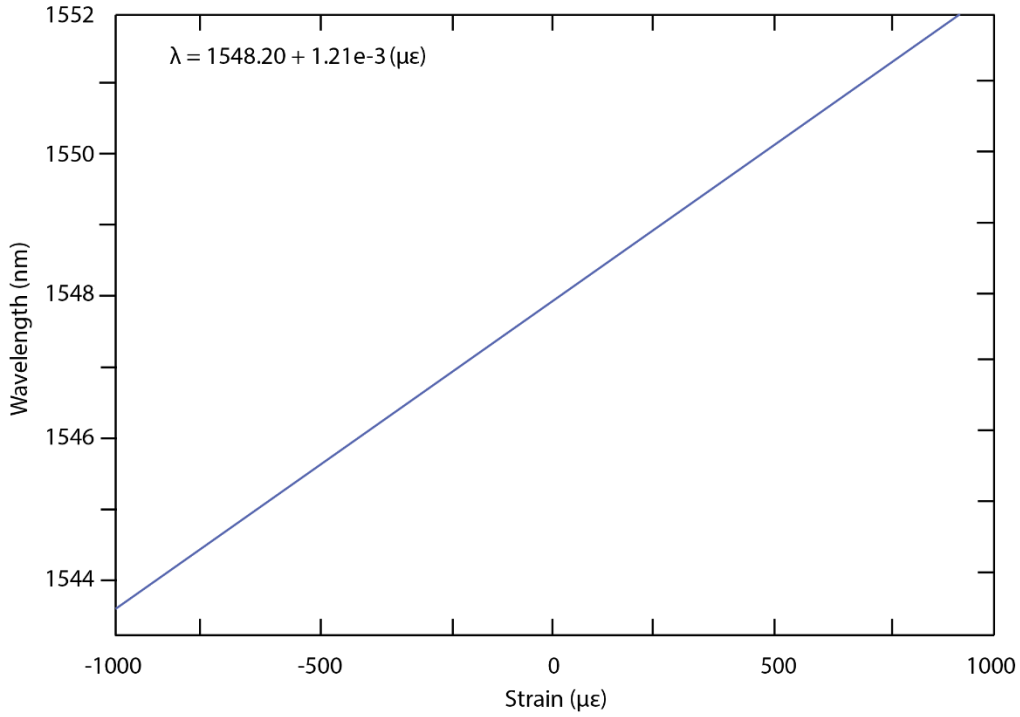

Figure 3.1 Bragg wavelength shift with applied strain on a $1548.20\,nm$ gratings

The second term of equation 3.1 denotes the effect due to temperature on the FBG. The shift in Bragg wavelength is due to the coefficient of thermal expansion, refractive index variations and the grating period. The shift in wavelength $\Delta\lambda_B$ as a result of temperature changes ΔT is described by [3]

$$\Delta\lambda_{B|T} = \lambda_B(\alpha + \xi)\Delta T \tag{3.4}$$

$$\alpha = \frac{1}{\Lambda}\left(\frac{\partial\Lambda}{\partial T}\right) \tag{3.5}$$

$$\xi = \frac{1}{n_{eff}}\left(\frac{\partial n_{eff}}{\partial T}\right) \tag{3.6}$$

where n_{eff} is the effective refractive index and Λ is the grating pitch of the fibre. Study has also shown that the temperature sensitivity of an optical bare fibre is given as $13.7\,pm/℃$ [3] at a wavelength of $1550\,nm$, corresponding to a change of $13.7\,pm$ for applying a temperature of $1℃$ to the fibre grating. An example of a Bragg wavelength shift due to applied temperature on a $1548.20\,nm$ gratings is shown in Figure 3.2. The variation pattern is linear and the slope is 13.7×10^{-3} and the fitting linear correlation coefficient reached 99.38%

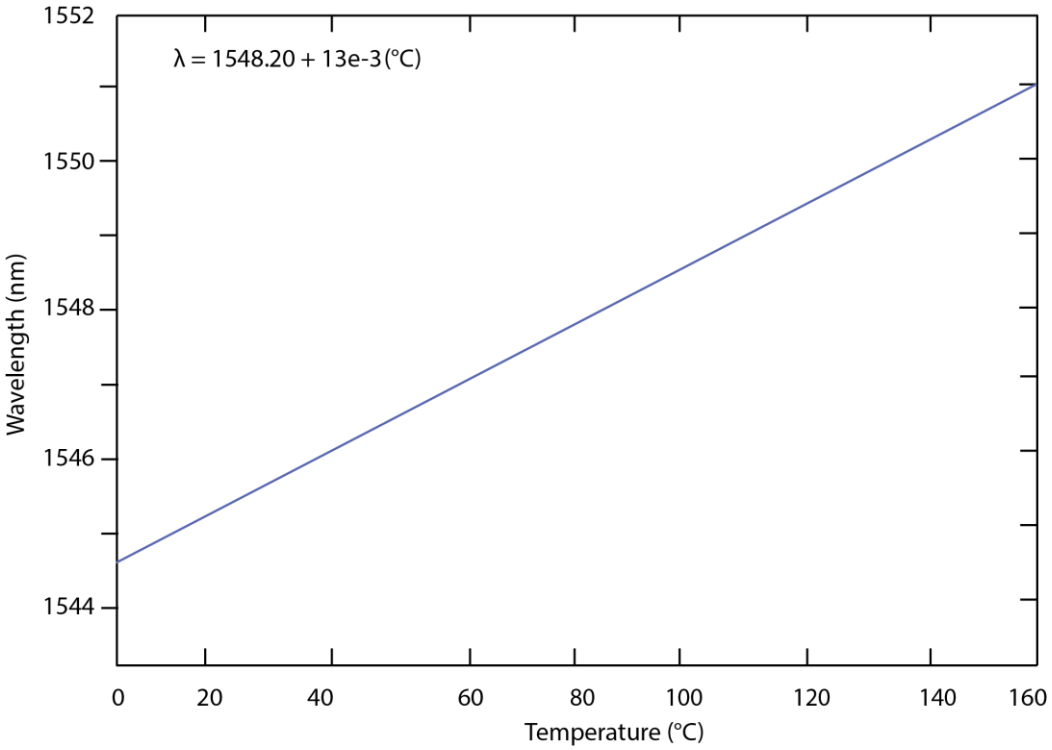

Figure 3.2 Bragg wavelength shift with applied temperature on a $1548.20\,nm$ gratings

It is interesting to note that any changes in the external perturbations will result in the Bragg wavelength shift that affects both strain and temperature. For any practical applications where a single parameter is to be measured, there is a need for compensation for the other parameter.

3.2.2 Pressure sensing of FBG

The shift in wavelength $\Delta\lambda_B$ is used to demodulate the pressure caused by the strain. For a pressure change of ΔP, the shift in wavelength is described by [4];

$$\frac{\Delta\lambda_{B|P}}{\lambda_B} = \left(\frac{1}{n_{eff}}\frac{\partial n_{eff}}{\partial P} + \frac{1}{\Lambda}\frac{\partial \Lambda}{\partial P}\right)\Delta P \tag{3.7}$$

Considering the change of grating period is exactly the same as that of optical fibre length, the normalized pitch-pressure and the index-pressure coefficients are given by [4];

$$\frac{\Delta\Lambda}{L} = \frac{\Delta L}{L} = -\frac{(1-2\nu)\Delta P}{E} \tag{3.8}$$

$$\frac{\Delta n_{eff}}{n_{eff}} = \frac{n_{eff}^2 \Delta P}{2E}[(1-2\nu)(2P_{11}+P_{12})] \tag{3.9}$$

Substituting equations 3.8 and 3.9 into equation 3.6, the shift in the Bragg wavelength as a result of pressure is given as [4];

$$\lambda_{B|P} = \lambda_B \left[-\frac{(1-2\nu)}{E} + \frac{n_{eff}^2 P}{2E}[(1-2\nu)(2P_{11}+P_{12})] \right] \Delta P \tag{3.10}$$

where E is the Young's modulus of the fibre. This shows that the shift in Bragg wavelength is directly proportional to the change in pressure ΔP, and this change is due to both change in the effective refractive index of the fibre and the change in grating length of the fibre. Previous work on FBG has shown to have pressure sensitivity of $48\, pm/kPa$ [3], though higher sensitive FBG have been achieved. It is shown that induced strain, temperature and pressure are measurable when applied to FBG.

3.3 Method, modelling and simulation of FBG

To model the FBG, the CMT will be considered since it is one of the best tools in understanding the optical properties of gratings. The CMT is a powerful mathematical tool for obtaining quantitative information of the spectral

dependence of FBG and the diffraction efficiency. It is one of the popular tools used in describing the behaviour of Bragg gratings by analysing the wave propagation and interactions in optical waveguides. This is mainly due to its simplicity and accuracy in modelling the optical properties of most fibre gratings. CMT allows the second order differential equation to be expressed as one or more uncoupled first order differential equations. The following assumptions are generally made with CMT in solving the Maxwell equations: Linearity, time-reversal symmetry, time-invariance, weak mode coupling (small perturbation of uncoupled modes) and energy conservation.

3.3.1 Models of FBG and the coupled-mode theory (CMT)

When a fibre is subjected to varying pattern of ultra-violet light, the refractive index perturbation that produces an FBG is formed. The relationship between the spectral dependence and the grating structure of the fibre grating is often described by the CMT. It aims to solve the Maxwell equations for a perturbed waveguide, see Appendix A for the detailed derivation of the CMT. For simplicity, the fabricated FBG perturbation on the effective refractive index n_{eff} of the guided modes is expressed as [5]

$$\partial n_{eff}(z) = \overline{\partial n_{eff}}(z)\left[1 + V\cos\left(\frac{2\pi}{\Lambda}z + \varphi(z)\right)\right] \tag{3.11}$$

where $\overline{\partial n_{eff}}$ is the mean refractive index, V is the fringe visibility of the index change, Λ is the grating period and $\varphi(z)$ denotes the grating chirp. The change of the refractive index along the region of the FBG can be divided into a

constant offset (mean amplitude) and a variable part (sinusoidal variation). For a single mode FBG, the simplified coupled mode equations are given as [5]

$$\frac{dR}{dz} = i\hat{\sigma}R(z) + i\kappa S(z) \tag{3.12}$$

$$\frac{dS}{dz} = -i\hat{\sigma}S(z) - i\kappa^{*}R(z) \tag{3.13}$$

Where $R(z) = A(z)\exp(i\partial(z) - \frac{\varphi}{2})$ and $S(z) = B(z)\exp(-i\partial(z) + \frac{\varphi}{2})$, are the amplitudes of forward-propagating and backward-propagating modes respectively. κ is the continuous coupling and $\hat{\sigma}$ is the general self-coupling coefficient. They are defined as [5];

$$\hat{\sigma} = \partial + \sigma - \frac{1}{2}\frac{d\varphi}{dz} \tag{3.14}$$

$$\kappa = \kappa^{*} = \frac{\pi}{\lambda} v\overline{\partial n_{eff}} \tag{3.15}$$

The detuning ∂ and σ in equation 3.14 are defined as [5]

$$\partial = \beta - \frac{\pi}{\Lambda} = 2\pi n\left(\frac{1}{\lambda} - \frac{1}{\lambda_D}\right) \tag{3.16}$$

$$\sigma = \frac{2\pi}{\lambda}\overline{\partial n_{eff}} \tag{3.17}$$

For a uniform FBG, in which β is the mode propagation constant, $\overline{\partial n_{eff}}$ is a constant and the grating chirp $\frac{d\varphi}{dz} = 0$, and thus κ, σ, and $\hat{\sigma}$ in equations 3.14, 3.15 and 3.17 are constants. Given appropriate boundary condition, one may arrive at a close form solution to these equations. For a uniform fibre grating length L, assuming a forward propagation wave incident from $z \to -\infty$ and no backward propagation wave exit for $z \geq \frac{L}{2}$, the reflectivity can be determined. The amplitude is expressed as $\rho = \frac{S\left(-\frac{L}{2}\right)}{R\left(-\frac{L}{2}\right)}$ and the power reflectivity coefficients $R = |\rho|^2$ By specifying the appropriate boundary conditions $R(-L/2) = 1$, $S(-L/2) = 0$ the analytical expression of the power reflection coefficient is obtained as [5, 6]

$$\rho = \frac{-\kappa \sinh\sqrt{(\kappa L)^2 - (\sigma L)^2}}{\kappa \sinh\sqrt{(\kappa L)^2 - (\sigma L)^2} + i\sqrt{\kappa^2 - \sigma^2}\cosh\sqrt{(\kappa L)^2 - (\sigma L)^2}} \tag{3.18}$$

and

$$R = \frac{\sinh^2\sqrt{(\kappa L)^2 - (\sigma L)^2}}{-\frac{\sigma^2}{\kappa^2} + \cosh^2\sqrt{(\kappa L)^2 - (\sigma L)^2}} \tag{3.19}$$

The transfer matrix method is applied to solve the coupled mode theory equations and to obtain the spectral response of FBG. The FBG with grating length L is divided into sections of M as shown in Figure 3.3. The larger the number of M, the more accurate this method is. During design, care should be taken not to make M arbitrarily too large as the coupled mode theory becomes difficult to implement for a uniform grating section of just few periods long.

Figure 3.3 The transfer matrix method applied to obtain the spectra characteristics of a FBG

The amplitude of the forward-propagation mode and the backward-propagation mode before and after the i^{th} uniform sections are represented in a matrix of the form F_i as;

$$\begin{bmatrix} R_i \\ S_i \end{bmatrix} = F_i \begin{bmatrix} R_{i-1} \\ S_{i-1} \end{bmatrix} = \begin{bmatrix} F_{11} & F_{12} \\ F_{21} & F_{22} \end{bmatrix} \begin{bmatrix} R_{i-1} \\ S_{i-1} \end{bmatrix} \tag{3.20}$$

where R_i and S_i are the amplitudes of the forward-propagation mode and backward-propagation mode after the i^{th} uniform sections and R_{i-1} and S_{i-1} are the amplitudes of the forward-propagation mode and backward-propagation mode before the i^{th} uniform sections. The elements in the transfer matrix are represented as;

$$F_{11} = F^*{}_{22} = \cosh(\gamma_B \Delta z) - i\frac{\hat{\sigma}}{\gamma_B}\sinh(\gamma_B \Delta z) \tag{3.21}$$

$$F_{12} = F^*{}_{21} = -i\frac{\kappa}{\gamma_B}\sinh(\gamma_B \Delta z) \tag{3.22}$$

where Δz is the length of the i^{th} uniform section, $\gamma_B = \sqrt{\kappa^2 - \sigma^2}$ is the imaginary part for which $|\hat{\sigma}| > \kappa$ [5] , and $'*'$ represent the complex conjugate. The output amplitude are obtained by multiplying all the matrices for individual sections as

$$\begin{bmatrix} R_M \\ S_M \end{bmatrix} = F \begin{bmatrix} R_0 \\ S_0 \end{bmatrix} \tag{3.23}$$

where $F = F_M . F_{M-1} \dots \dots F_1$

The output amplitudes for the non-uniform FBG are obtained by applying the boundary conditions, $R_0 = R(L) = 1$ and $S_0 = S(L) = 1$. The amplitude reflection coefficient $\rho = {R_M}/{S_M}$, and the power reflection coefficient $R = |\rho|^2$ are calculated by the transfer matrix method.

The reflectivity of a uniform Bragg grating is calculated from equation 3.19 for $\kappa L = 2$ and $\kappa L = 6$. Reflectivity is plotted against the normalized wavelength as shown in Figure 3.4. The total number of grating periods $N = {L}/{\Lambda}$. The maximum reflectivity for Bragg grating derived from equation 3.19 is given as

$$R_{max} = \tanh^2(\kappa L) \tag{3.24}$$

and this occurs when $\hat{\sigma} = 0$, or at a wavelength of

$$\lambda_{max} = \left(1 + \frac{\overline{\partial n_{eff}}}{n_{eff}}\right)\lambda_D \tag{3.25}$$

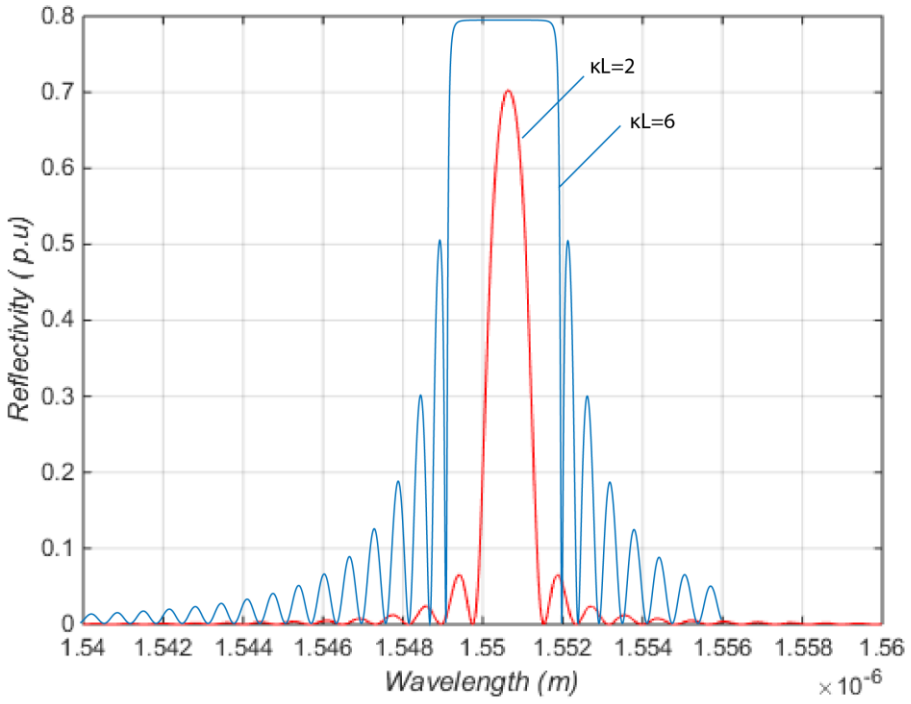

Figure 3.4 Reflectivity spectra response against normalized wavelength for a uniform Bragg grating with $\kappa L = 2$ and $\kappa L = 6$

It can be observed that the bandwidth of the FBG is extremely narrow, this means at a $1550\,nm$ wavelength, one can achieve a relatively narrow bandwidth of $0.03 - 0.05\,nm$. For low value of κL ($\kappa L = 2$), the reflectivity is less than 1 but as κL increases to $\kappa L = 6$, the reflectivity approaches the value of 0.8, and the bandwidth of the FBG increases. By using a FBG with the right design parameters a perfect reflection of the signal can be obtained from the FBG.

3.3.2 Simulation of FBG

The spectral dependency on a number of various parameters has been investigated and reported, such as grating length [7-10], number of grids [11], changes in refractive index [12], strain [13], temperature [14, 15]. By applying equation 3.19, the spectral response of a uniform FBG is obtained and

simulated. The simulation was carried out in MATLAB and the parameters of the uniform FBG used for the simulation are listed in Table 3.1.

Table 3.1 Simulation parameters for FBG [10]

Parameter	Symbol	Value
Effective refractive index	n_{eff}	1.447
Grating length changes	L	$1 - 8\,mm$
Bragg wavelength	λ_B	$1550\,nm$
Change in refractive index	∂_n	$0.0005 - 0.002$
Grating period	Λ	$535.59\ nm$

3.3.3 Investigation of spectral reflectivity dependence on grating length

The spectral response of a uniform FBG is affected by changing the length of the grating by external perturbations such as strain, temperature and pressure. The dependency of the spectral reflectivity on different grating lengths were observed and analysed by varying the grating length from $1 - 10\,mm$.

Figure 3.5 shows the simulated results of the relationship between reflectivity and wavelength for different lengths of the grating. Clearly from the graphs, the reflectivity of the uniform FBG increases with increase in the grating length. When the grating length $L = 1\,mm,\ 2\,mm,\ 3\,mm,\ 4\,mm$ and $5\,mm$ the maximum reflectivity is $58.83\%,\ 93.28\%,\ 99.09\%,\ 99.88\%$ and 99.98% respectively. At $L = 6\,mm$, the reflectivity reaches 100%. When the grating length is increased further to $L = 10\,mm$, it is observed that the maximum reflectivity maintains at 100%.

Figure 3.6 shows a linear relationship between the change in grating length and the shift in centre wavelength. It is observed from the graph, as the grating length changes, there is a corresponding shift in the centre wavelength.

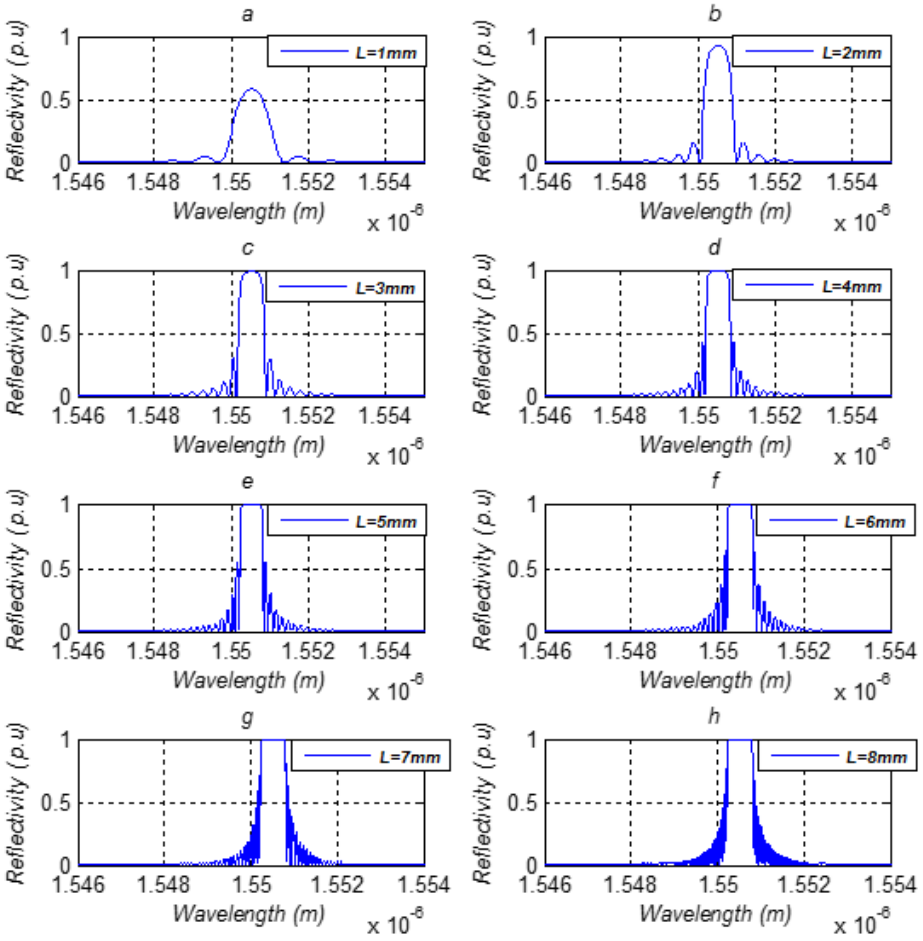

Figure 3.5 Spectral reflectivity characteristics of FBG for different grating length $1-8\,mm$ $(a-h)$

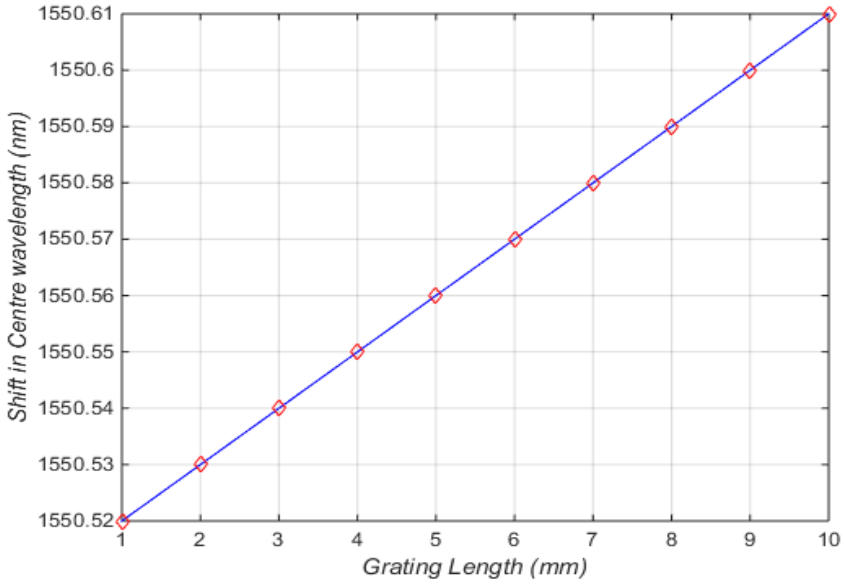

Figure 3.6 Effect of grating length on FBG

3.3.4 Investigation of spectral reflectivity on refractive index

The spectral reflectivity dependence on varying refractive indices were also studied and analysed. Figure 3.7 shows the results of the simulation of a uniform FBG with grating length of $L = 1\,mm$ as the change in refractive index is varied from $\partial_n = 0.0005 - 0.003$. For grating with refractive index of $\partial n = 0.0005,\ 0.0006,\ 0.0007,\ 0.0008,\ 0.0009$ and 0.001 the maximum reflectivity is 58.83%, 70.28%, 79.07%, 85.51%, 90.09% and 99.01% respectively. 100% maximum reflectivity was achieved at ∂_n = 0.002 and maintains this value when the refractive index is further increased. Figure 3.8 shows the linear relationship between the refractive index change and the shift in centre wavelength. As the change in refractive index increases, there is a corresponding increase in the centre wavelength which is in agreement with the findings of Sunita and Mishra [12]. The shifts in centre wavelength is used for calculating the external perturbations like strain, temperature, pressure etc.

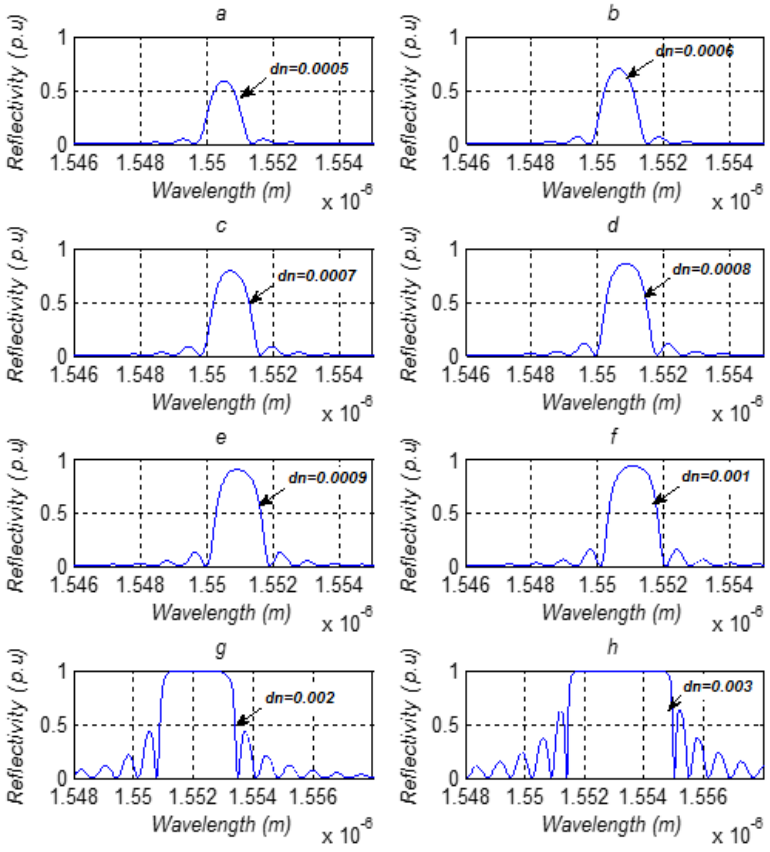

Figure 3.7 Spectral reflectivity characteristics of FBG for different refractive index change $0.0005 - 0.003$ from a to h

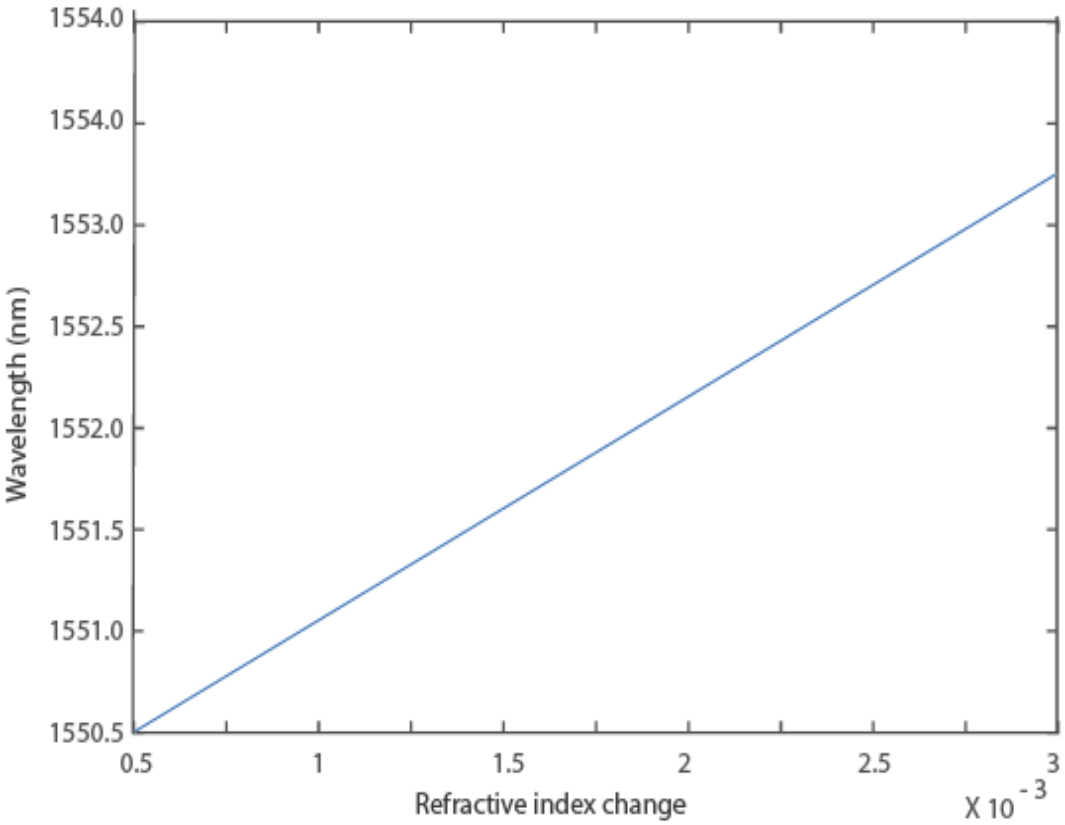

Figure 3.8 Effect of refractive index change on centre wavelength

3.3.5 Investigation of bandwidth dependence on grating length and refractive index

The dependence of bandwidth on grating length was observed and analysed, the bandwidth values of FBG with different grating lengths were obtained from Figure 3.5 and plotted in Figure 3.9. It can be observed that the bandwidth reduces with increase in grating length but increases with increase in change in refractive index of a FBG. In Figure 3.9, it can be seen that when the grating length is $5\,mm$ with a refractive index change of 0.0005 the bandwidth is $0.6\,nm$. As the grating length reduces to $2\,mm$, the bandwidth increases to $0.75\,nm$. Theoretically, larger bandwidth of a FBG can be achieved with smaller grating length. Thus, for a strong grating with a large bandwidth to be achieved, the

grating length has to be small and the refractive index change must be large. However, for a strong grating with smaller bandwidth, the grating length must be long and the refractive index change must be small. Also, it is worth noting that the strength of the side-lobes in the reflection spectrum increases with increase in both the grating length and the change in refractive index as indicated in Figure 3.5 and Figure 3.7.

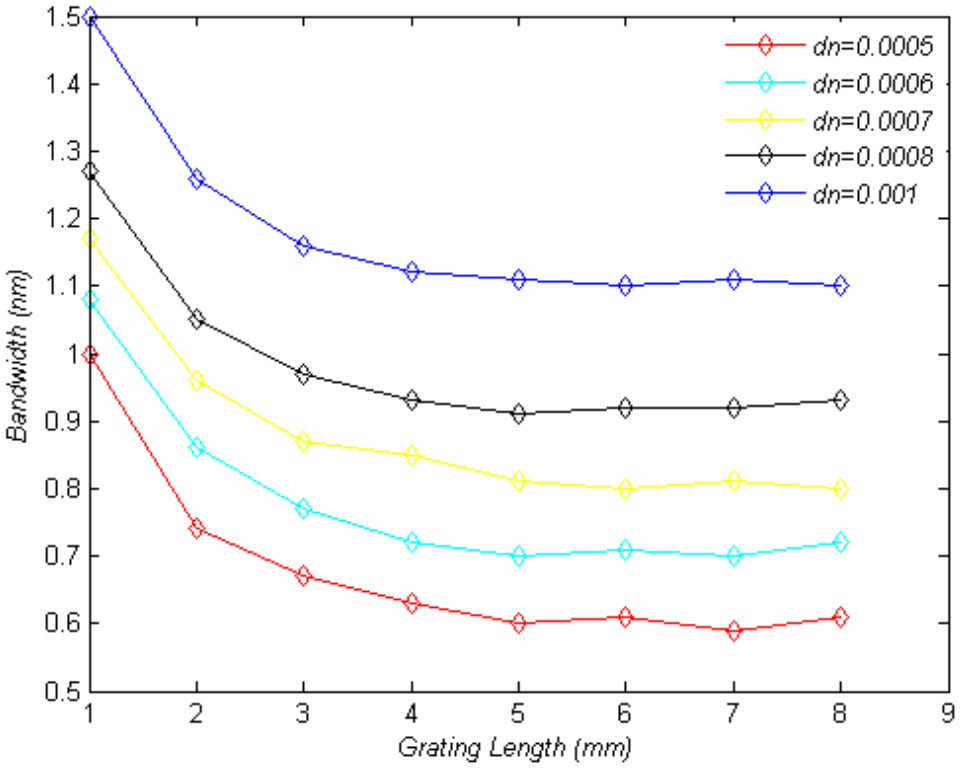

Figure 3.9 Effect of grating length on bandwidth for different refractive index change $0.0005 - 0.001$

In summary, by applying the coupled mode theory, it can be shown that a larger bandwidth can be achieved with short grating length with good design. The modelling, simulation and characterization of optical FBG were presented. The spectra reflectivity, bandwidth and side-lobes were analysed with changes in grating length and refractive index. The reflectivity increases with

increase in grating length and refractive index change. The bandwidth of FBG decreases by increasing the grating length and it increases by increasing the refractive index change. The strength of the side-lobes increases with increase in the grating length and the refractive index change which can be suppressed by apodization (also called a tapering function or window function which is a function used to smoothly bring a sampled signal down to zero at the edges of the sampled region).

These analysis give better understanding of FBG characteristics and suggest possible ways of designing high performance FBG sensors for oil and gas applications.

3.4 Sensitivity Analysis of FBG

In this section, theoretical models and simulation of the cross-sensitivity function in multi-parameter FBG based sensor for oil and gas applications has been developed and analysed. Simulation results show that the interactions between the physical properties of FBG sensors and that of cross-sensitivity would change widely when external parameters and fibre material effects are very large.

3.4.1 Cross sensitivity analysis of FBG based sensor for oil and gas applications

The sensing capability of FBGs has been intensively studied and developed for the past two decades [16]. This technology is now gaining wide acceptance in oil and gas sensing applications because of their wavelength multiplexing capability, good linearity, relatively small size and ability to operate in a harsh environment [17-19]. The relatively small size and light weight of FBGs makes them very attractive for sensing strain distribution in micro-structures by embedding it into the structures without affecting the internal properties of the

structures. One of the major challenges of measuring external parameters like temperature, axial strain and pressure simultaneously using a FBG in most practical applications is the issue of cross sensitivity. While the effect of cross sensitivity due to double parameters like temperature and strain or temperature and pressure have been reported in the literature [20, 21], the effect of cross sensitivity on all three parameters (temperature, strain and pressure) are scarce in the literature. This analysis is based on the fact that in most practical oil and gas applications such as the downhole measurements and underwater pressure measurement, all three parameters act simultaneously on the FBG sensor. There is the need to analyse the effect of cross sensitivity of FBG sensor when used as a multi-parameter sensor for oil and gas based applications.

In this work, theoretical models of the cross sensitivity function of an FBG and its physical mechanism has been developed and analysed. This analysis was based on the fact that FBG sensor was in the state in which the strain, temperature and pressure were simultaneously functioning on. The simulated results show that the interactions between the physical properties of FBG sensors and the properties of cross sensitivity would change widely when the external parameters and fibre material effects are very large.

3.4.2 Theoretical analysis of FBG cross sensitivity

The Bragg wavelength λ_B is given as [5]

$$\lambda_B = 2n_{eff}\Lambda \tag{3.26}$$

where n_{eff} is the effective refractive index of the optical mode propagation along the fibre and Λ is the grating of the variation of the refractive index. Different applications for which of FBG sensor for which external perturbations (temperature, pressure, strain) cause changes in n_{eff} and Λ in most oil and gas applications leading to shift in the Bragg wavelength will be considered and analysed theoretically. For example, when FBG sensor is affected by both temperature and pressure, the Bragg wavelength will be a function of both temperature T, and pressure P, expressed as [20]

$$\lambda_B = \lambda_B(T, P) \tag{3.27}$$

This equation can be expanded using the Taylor's series expansion technique given as [20];

$$\lambda_B = \lambda_B(T_0, P_0) + \lambda_B\left(\Delta T\frac{\partial}{\partial T} + \Delta P\frac{\partial}{\partial P}\right) + \frac{1}{2!}\lambda_B\left(\Delta T\frac{\partial}{\partial T} + \Delta P\frac{\partial}{\partial P}\right)^2 + \cdots\cdots \tag{3.28}$$

where ΔT and ΔP are the changes in temperature and pressure respectively and (T_0, P_0) is the reference state. The shift in Bragg wavelength $\Delta\lambda_B$ as a function of temperature and applied pressure is derived from the Taylor's series expansion as;

$$\Delta\lambda_B = \Delta T\frac{\partial\lambda_B}{\partial T} + \Delta P\frac{\partial\lambda_B}{\partial P} + \Delta T\Delta P\frac{\partial^2\lambda_B}{\partial T\partial P} + \frac{1}{2}\left(\Delta T^2\frac{\partial^2\lambda_B}{\partial T} + \Delta P^2\frac{\partial^2\lambda_B}{\partial P}\right) \tag{3.29}$$

Equation 3.29 shows that $\Delta\lambda_B$ is not only affected by ΔT and ΔP, but also by a cross-sensitivity term and other higher order terms. The Bragg wavelength

shift caused by higher order terms increases with an increase of ΔT and ΔP. On the one hand, if ΔT and ΔP are large enough, a nonlinear Bragg wavelength shift would be created by them. On the other hand, if ΔT and ΔP are not large enough, the higher order terms can be neglected compared to the first order terms and cross sensitivity terms. Also, higher order terms do not capture the cross sensitivity terms. Therefore, higher order terms without cross product of both change in temperature and pressure are dropped. Equation 3.29 can be simplified as:

$$\Delta\lambda_B = \Delta T \frac{\partial \lambda_B}{\partial T} + \Delta P \frac{\partial \lambda_B}{\partial P} + \Delta T \Delta P \frac{\partial^2 \lambda_B}{\partial T \partial P} \tag{3.30}$$

which can be further be simplified to:

$$\Delta\lambda_B = \Delta T \cdot K_T + \Delta P \cdot K_P + \Delta T \Delta P \cdot K_{TP} \tag{3.31}$$

where K_T, K_P, and K_{TP} are the temperature sensitivity, pressure sensitivity and cross sensitivity respectively which are expressed as [20]:

$$K_T = \frac{\partial \lambda_B}{\partial T} = 2 \cdot \left(\frac{\partial n_{eff}}{\partial T} \cdot \Lambda + \frac{\partial \Lambda}{\partial T} \cdot n_{eff} \right) = \lambda_B (\alpha + \xi) \tag{3.32}$$

$$K_P = \frac{\partial \lambda_B}{\partial P} = 2 \cdot \left(\frac{\partial n_{eff}}{\partial P} \cdot \Lambda + \frac{\partial \Lambda}{\partial P} \cdot n_{eff} \right)$$

$$= \lambda_B \left[-\frac{(1-2\nu)}{E} + \frac{n_{eff}^2 P}{2E} [(1-2\nu)(2P_{11} + P_{12})] \right] \tag{3.33}$$

$$K_{TP} = \frac{\partial^2 \lambda_B}{\partial T \partial P} = \frac{K_T K_P}{\lambda_B} + 2\xi \left(K_P + \frac{\lambda_B (1 - 2\nu)}{E} \right) \tag{3.34}$$

Equations 3.32 – 3.34 show that temperature sensitivity K_T as a function of the coefficient of thermal expansion, α and thermo-optic coefficient, ξ and the pressure sensitivity K_P is a function of the fibre parameters (Young's modulus E, Poisson's ratio ν, effective refractive index n_{eff}, and the components of the fibre optic strain tensor $(P_{11},\ 2P_{11})$ also known as the Pockels constants of the fibre). The coefficient of cross-sensitivity term K_{TP}, from equation 3.35 shows the nonlinear relationship between the Bragg wavelength shift $\Delta\lambda_B$ and changes in either temperature ΔT or pressure ΔP. The cross sensitivity term χ_{cs} is derived from equation 3.31 as:

$$\chi_{cs} = \Delta T \Delta P \cdot K_{TP} = \Delta T \Delta P \frac{K_T K_P}{\lambda_B} + 2\xi \left(K_P + \frac{\lambda_B (1 - 2\nu)}{E} \right) \tag{3.35}$$

when the FBG sensor is affected by three parameters (temperature, strain and pressure), the Bragg wavelength shift will be a function of temperature axial strain and transverse pressure represented by [20]:

$$\lambda_B = \lambda_B(T, \varepsilon, P) \tag{3.36}$$

Expanding equation 3.36 using the Taylor's series expansion technique given as;

$$\lambda_B = \lambda_B(T_0,\ \varepsilon_0,\ P_0) + \lambda_B \left(\Delta T \frac{\partial}{\partial T} + \Delta\varepsilon \frac{\partial}{\partial \varepsilon} + \Delta P \frac{\partial}{\partial P} \right)$$

$$+ \frac{1}{2!} \lambda_B \left(\Delta T \frac{\partial}{\partial T} + \Delta\varepsilon \frac{\partial}{\partial \varepsilon} + \Delta P \frac{\partial}{\partial P} \right)^2 + \frac{1}{3!} \lambda_B \left(\Delta T \frac{\partial}{\partial T} + \Delta\varepsilon \frac{\partial}{\partial \varepsilon} + \Delta P \frac{\partial}{\partial P} \right)^3 + \cdots\cdots \tag{3.37}$$

The shift in Bragg wavelength $\Delta\lambda_B$ as a function of temperature, strain and applied pressure is derived from the Taylor's series expansion as;

$$\Delta\lambda_B = \lambda_B(T, \varepsilon, P) - \lambda_B(T_0,\ \varepsilon_0,\ P_0)$$
$$= \lambda_B\left(\Delta T\frac{\partial}{\partial T} + \Delta\varepsilon\frac{\partial}{\partial\varepsilon} + \Delta P\frac{\partial}{\partial P}\right) + \frac{1}{2!}\lambda_B\left(\Delta T\frac{\partial}{\partial T} + \Delta\varepsilon\frac{\partial}{\partial\varepsilon} + \Delta P\frac{\partial}{\partial P}\right)^2$$
$$+ \frac{1}{3!}\lambda_B\left(\Delta T\frac{\partial}{\partial T} + \Delta\varepsilon\frac{\partial}{\partial\varepsilon} + \Delta P\frac{\partial}{\partial P}\right)^3 + \cdots\cdots \quad (3.38)$$

Expanding equation 3.38, $\Delta\lambda_B$ can be expressed as:

$$\Delta\lambda_B = \Delta T\frac{\partial\lambda_B}{\partial T} + \Delta\varepsilon\frac{\partial\lambda_B}{\partial\varepsilon} + \Delta P\frac{\partial\lambda_B}{\partial P} + \Delta T\Delta\varepsilon\frac{\partial^2\lambda_B}{\partial T\partial\varepsilon} + \Delta T\Delta P\frac{\partial^2\lambda_B}{\partial T\partial P} + \Delta\varepsilon\Delta P\frac{\partial^2\lambda_B}{\partial\varepsilon\partial P}$$
$$+ \frac{1}{2}\Delta T^2\Delta\varepsilon\frac{\partial^3\lambda_B}{\partial T^2\partial\varepsilon} + \frac{1}{2}\Delta T\Delta\varepsilon^2\frac{\partial^3\lambda_B}{\partial T\partial\varepsilon^2} + \frac{1}{2}\Delta T^2\Delta P\frac{\partial^3\lambda_B}{\partial T^2\partial P} + \frac{1}{2}\Delta T\Delta P^2\frac{\partial^3\lambda_B}{\partial T\partial P^2}$$
$$+ \frac{1}{2}\Delta\varepsilon^2\Delta P\frac{\partial^3\lambda_B}{\partial\varepsilon^2\partial P} + \frac{1}{2}\Delta\varepsilon\Delta P^2\frac{\partial^3\lambda_B}{\partial\varepsilon\partial P^2} + +\Delta T\Delta\varepsilon\Delta P\frac{\partial^3\lambda_B}{\partial T\partial\varepsilon\partial P} + \cdots \quad (3.39)$$

Equation 3.39 shows the $\Delta\lambda_B$ is not only affected by ΔT, $\Delta\varepsilon$ and ΔP, but also by a cross sensitivity term and other higher order terms. $\Delta\lambda_B$ increases with geometry increase in ΔT, $\Delta\varepsilon$ and ΔP. Neglecting the higher order terms, if ΔT, $\Delta\varepsilon$ and ΔP values are small enough, the Bragg wavelength shift can be represented as:

$$\Delta\lambda_B \approx \Delta T\cdot K_T + \Delta\varepsilon\cdot K_\varepsilon + \Delta P\cdot K_P + \chi_{cs} \quad (3.40)$$

where K_T, K_P, and K_ε are the coefficient of temperature, strain and pressure sensitivities respectively and χ_{cs} is the cross sensitivity term.

The expression for K_ε is given by

$$K_\varepsilon = \lambda_B\,(1 - P_e) \tag{3.41}$$

where P_e is the effective strain-optic constant defined as;

$$P_e = \frac{n_{eff}^2}{2}[P_{12} - \nu(P_{12} + P_{12})]$$

The expression for $K_T, and\ K_P$ are already obtained in equations 3.32 and 3.33. The cross-sensitivity term χ_{cs}, in equation 3.39 is expressed as:

$$\begin{aligned}\chi_{cs} = {} & \Delta T\Delta\varepsilon\frac{\partial^2\lambda_B}{\partial T\partial\varepsilon} + \Delta T\Delta P\frac{\partial^2\lambda_B}{\partial T\partial P} + \Delta\varepsilon\Delta P\frac{\partial^2\lambda_B}{\partial\varepsilon\partial P} + \frac{1}{2}\Delta T^2\Delta\varepsilon\frac{\partial^3\lambda_B}{\partial T^2\partial\varepsilon} + \frac{1}{2}\Delta T\Delta\varepsilon^2\frac{\partial^3\lambda_B}{\partial T\partial\varepsilon^2} \\ & + \frac{1}{2}\Delta T^2\Delta P\frac{\partial^3\lambda_B}{\partial T^2\partial P} + \frac{1}{2}\Delta T\Delta P^2\frac{\partial^3\lambda_B}{\partial T\partial P^2} + \frac{1}{2}\Delta\varepsilon^2\Delta P\frac{\partial^3\lambda_B}{\partial\varepsilon^2\partial P} + \frac{1}{2}\Delta\varepsilon\Delta P^2\frac{\partial^3\lambda_B}{\partial\varepsilon\partial P^2} \\ & + +\Delta T\Delta\varepsilon\Delta P\frac{\partial^3\lambda_B}{\partial T\partial\varepsilon\partial P} + \cdots\end{aligned} \tag{3.42}$$

From equation 3.42, the cross sensitivity for double parameters ($K_{T\varepsilon}$, $K_{\varepsilon P}$, and K_{TP}) and triple parameters $K_{T\varepsilon P}$ can be derived as:

$$K_{T\varepsilon} = \frac{\partial^2\lambda_B}{\partial T\partial\varepsilon} = \frac{K_\varepsilon K_T}{\lambda_B} + 2\xi(K_\varepsilon - \lambda_B) \tag{3.43}$$

$$K_{TP} = \frac{\partial^2\lambda_B}{\partial T\partial P} = \frac{K_T K_P}{\lambda_B} + 2\xi\left(K_P + \frac{\lambda_B(1-2\nu)}{E}\right) \tag{3.44}$$

$$K_{\varepsilon P} = \frac{\partial^2\lambda_B}{\partial\varepsilon\partial P} = \frac{3K_\varepsilon K_P}{\lambda_B} - 2\left(K_P + \frac{(1-2\nu)}{E}K_\varepsilon - \frac{\lambda_B(1-2\nu)}{E}\right) \tag{3.45}$$

$$K_{T\varepsilon P} = M_1 \cdot K_T + M_2 \cdot K_\varepsilon + M_3 \cdot K_P + M_4 \cdot K_\varepsilon K_T + M_5 \cdot K_T K_P + M_6 \cdot K_\varepsilon K_P$$

$$+M_7 \cdot K_\varepsilon K_P K_T + M_8 \tag{3.46}$$

where $M_i, i = 1 - 8$ are all coefficients and are represented in Table 3.2

Table 3.1 Equation 3.46 coefficient expressions

Coefficient	$\boldsymbol{M_1}$	$\boldsymbol{M_2}$	$\boldsymbol{M_3}$	$\boldsymbol{M_4}$	$\boldsymbol{M_5}$	$\boldsymbol{M_6}$	$\boldsymbol{M_7}$	$\boldsymbol{M_8}$
Expression	$\frac{2(1-v)}{E}$	$\frac{10\xi(1-v)}{E}$	6ξ	$\frac{2(1-2v)}{\lambda_B E}$	$\frac{-2}{\lambda_B}$	$\frac{-4\xi}{\lambda_B}$	$\frac{4-\lambda^2{}_B}{\lambda^2{}_B}$	$\frac{-8\xi\lambda_B(1-2v)}{E}$

Substituting ($K_{T\varepsilon}$, $K_{\varepsilon P}$, K_{TP}) and $K_{T\varepsilon P}$ into equation 3.42, the expression for the cross sensitivity term can be simplified as;

$$\chi_{cs} = \Delta T \Delta\varepsilon \cdot K_{T\varepsilon} + \Delta T \Delta P \cdot K_{TP} + +\Delta T \Delta\varepsilon \Delta P \cdot K_{T\varepsilon P} \tag{3.47}$$

The cross sensitivity coefficients show the interactions between the mechanical and thermal effects on FBG when used for simultaneous measurement of temperature, strain and pressure.

3.5 Results and analysis of FBG cross sensitivity

The theoretical analysis and numerical simulation of the interactions between the physical properties of FBG sensors and the effect of external perturbations was performed. In equations 3.6 and 3.23, it can be shown that the cross sensitivity terms are affected not only by the external perturbations (temperature ΔT and pressure ΔP) but also by the fibre materials properties (Young's modulus E, Poisson's ratio v, effective refractive index n_{eff} and the

components of the fibre optic strain tensor (P_{11}, P_{11}) also known as the Pockels constants of the fibre). The cross sensitivity effect of a FBG based sensor in most oil and gas applications is crucial and should be minimized.

3.5.1 Cross sensitivity changes resulting from external perturbations

The parameters of a uniform FBG are constant in most practical applications. Using silica fibre in the simulation in this case, the parameters are listed in the Table 3.3. Parameters used for the simulation are for analytical and illustrative purposes.

Table 3.2 Silica fibre parameters for the cross sensitivity numerical simulation [3]

Parameter	$\boldsymbol{\alpha}(/℃)$	$\boldsymbol{\xi}(/℃)$	$\mathbf{n_{eff}}$	**v**	$\mathbf{E(N/m^2)}$	$\boldsymbol{\lambda_B(nm)}$	$\mathbf{P_{11}}$	$\mathbf{P_{12}}$
Value	0.5×10^{-6}	7×10^{-6}	1.47	0.17	7×10^{10}	1550	0.121	0.27

3.5.1.1 Double parameters (Temperature and pressure)

The cross sensitivity term χ_{cs} in equation 3.47 was plotted and analysed against the external perturbation and the parameter used in this simulation are temperature $T = 0 - 200\,℃$ and pressure $P = 0 - 200\,MPa$. As shown in Figure 3.10, the cross sensitivity term increases as the temperature and pressure increase. In addition, the growth rate of the cross sensitivity term increases with the increase in temperature and pressure. From the graph, it can be seen that the cross sensitivity term is greater than $4\,pm$ when the change in temperature ΔT and pressure ΔP get to about $180\,℃$ and $180\,MPa$ simultaneously.

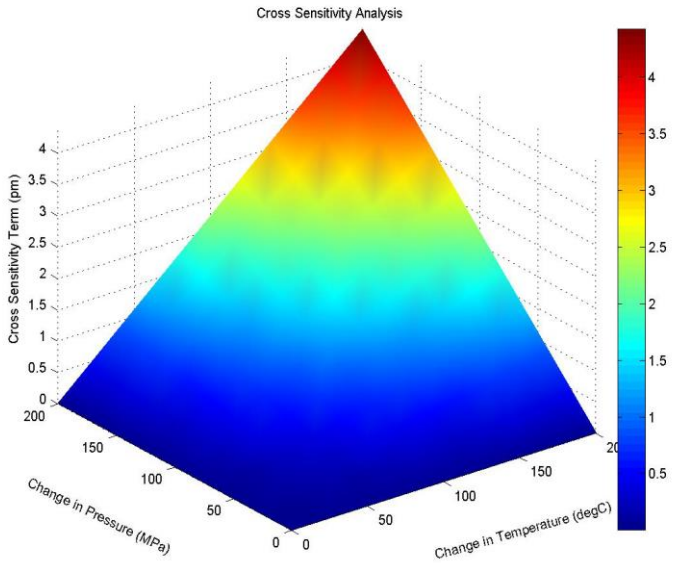

Fig 3.10 Cross sensitivity term changes with respect to both change in temperature and pressure

The results of this analysis indicate that in most FBG based oil and gas applications where temperature and pressure measurements are relatively high, in order to obtain more accurate results, the cross sensitivity term must be taken into consideration and the effect minimized.

3.5.1.2 Triple parameters (Temperature, strain and pressure)

The parameters of silica fibre shown in Table 3.3 and the expressions of parameters for the triple parameters cross sensitivity $K_{T\varepsilon P}$ in Table 3.2 for equation 3.47 are used for the simulation. The external perturbation parameters ($T, \varepsilon \; and \; P$.) used are $T = 0 - 100\,℃$, $\varepsilon = 0 - 1000\,\mu\varepsilon \; and \; P = 0 - 100\,MPa$. The simulation results illustrated in a 4D colour graph in Figure 3.11

shows the cross sensitivity term when the FBG is affected by external perturbations. In order to reach a smaller value of χ_{cs}, the absolute value of K_ε and K_P should be large enough, on the contrary, K_T should be small. However, if we use a FBG with a small value of K_T, the measurement for temperature will be inaccurate. In other words, we should design the FBG to have a smaller value of χ_{cs} and an effective value of single-parameter sensitivity (i.e., K_T, K_ε and K_P) in practical applications, rather than just considering the smallest value of χ_{cs}. This term increases as ΔT and $\Delta\varepsilon$ increase. However, the effect of ΔP on the cross sensitivity term χ_{cs} is so small that it can be neglected. From the graph, it can be seen that the maximum value for χ_{cs} is $0.4pm/(℃ \cdot \mu\varepsilon \cdot MPa)$. This value is very small that it can be hardly detected by most optical instrumentations and therefore, the effect of a triple parameter cross sensitivity can be neglected.

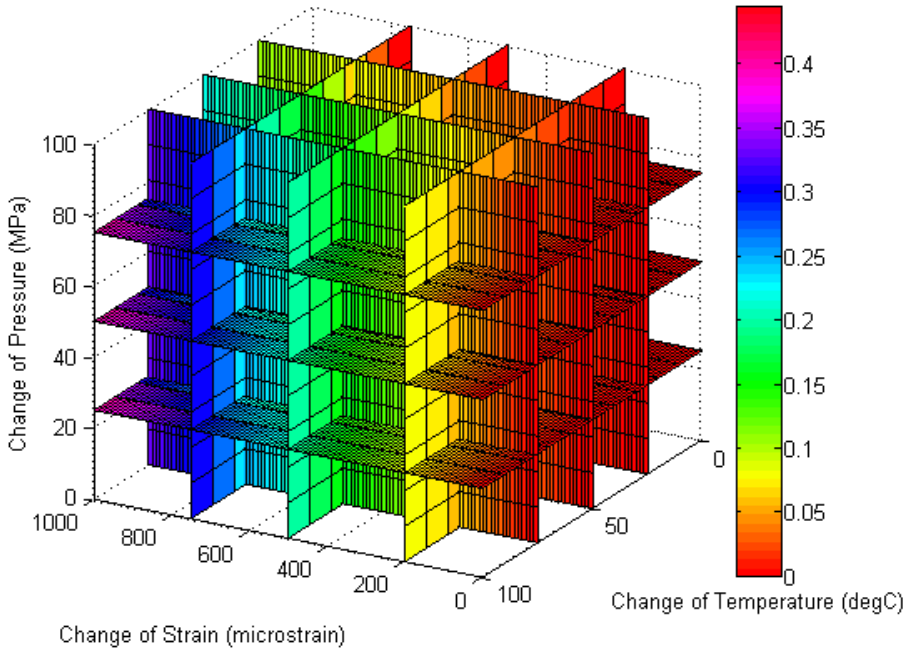

Figure 3.11 Cross sensitivity term changes with respect to change in temperature, strain and pressure

3.5.2 Cross sensitivity changes resulting from the effect of fibre materials

The influence of temperature sensitivity and pressure sensitivity on the cross sensitivity term while the external perturbations are kept constant was analysed and simulated.

3.5.2.1 Double parameters (Temperature sensitivity and pressure sensitivity)

Assuming the external perturbations $\Delta T = 200\,℃$ and $\Delta P = 200\,MPa$. From equation 3.35, χ_{cs} is a function of both K_T and K_P and then their relationship indicates that χ_{cs} is mainly affected by the pressure sensitivity K_P but not the temperature sensitivity K_T. Meanwhile, with the increase of K_P in the negative direction from $-1\,pm/MPa$ to $-6\,pm/MPa$, χ_{cs} decreases from $-1\,pm$ to $-5\,pm$, which is not large enough to be separated by most of the spectral instruments. Therefore, the effect of fiber material on the cross sensitivity term could be ignored in this case.

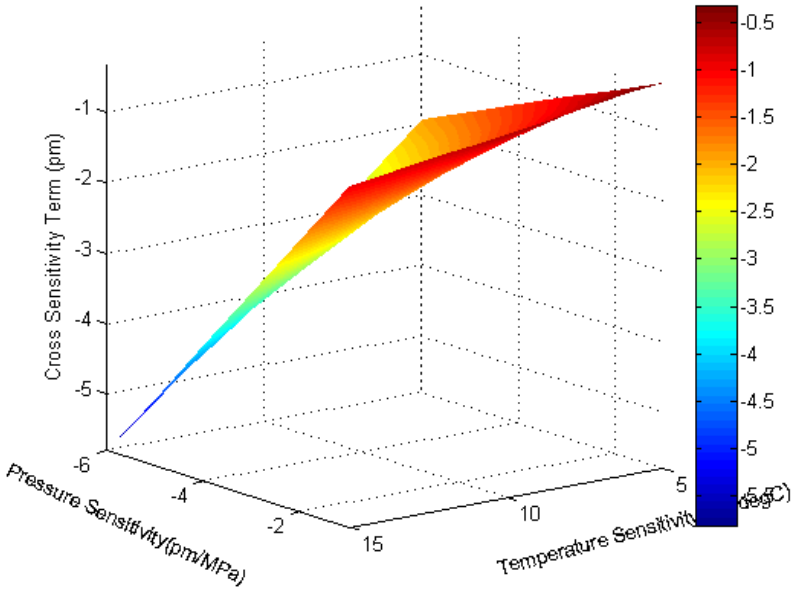

Figure 3.12 Cross sensitivity term changes with respect to change in the fibre materials for double parameters

3.5.2.2 Triple parameters sensitivity (Temperature, strain and pressure)

In this case, the effect of the triple parameters sensitivity (K_T, K_ε and K_P) on cross sensitivity term χ_{cs} while the external perturbations are kept constant was simulated and analysed. The values of the external parameters used are $\Delta T = 100\,℃$, $\Delta\varepsilon = 500\,\mu\varepsilon$, and $\Delta P = 100\,MPa$. The sensitivities values used are $K_T = 5 - 20pm/℃$, $K_\varepsilon = 0 - 10\,pm/\mu\varepsilon$ and $K_P = -10pm/MPa$ to $-1\,pm/MPa$. Figure 3.13 shows the simulated result for the cross sensitivity term χ_{cs} as a function of K_T, K_ε and K_P. From the figure, it is evident that as the absolute values of K_ε and K_P increase, χ_{cs} decreases. This shows that for χ_{cs} to be minimized, the relative values of K_ε and K_P must be very high. However, the value of K_T decreases as χ_{cs} decrease which depicts that it should be small in value for the effect of χ_{cs} to be minimized.

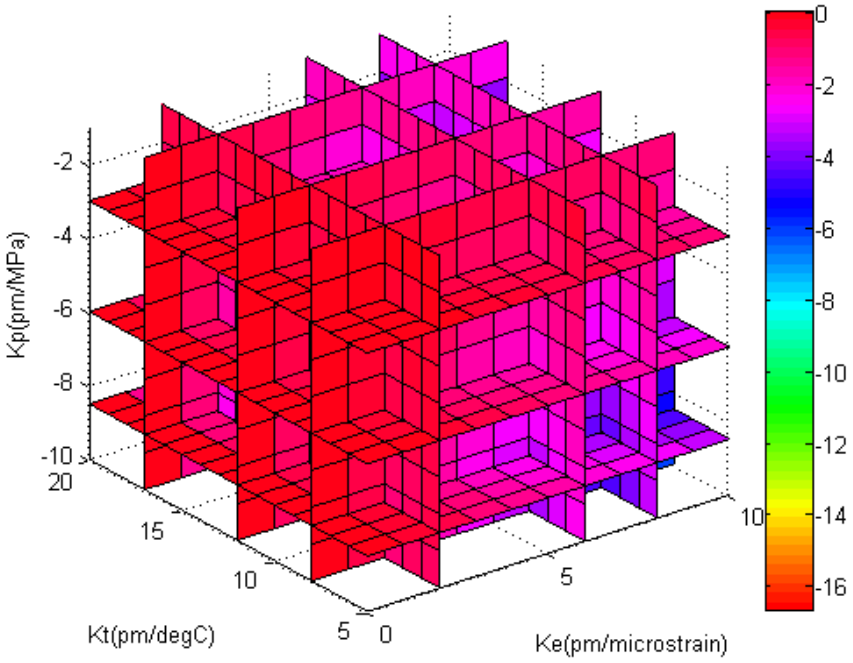

Figure 3.13 Cross sensitivity term changes with respect to change in the fibre materials for triple parameters

3.6 Identification of problem and summary

To enhance the measurement accuracy of FBG and minimize the effect of cross sensitivity for multi-parameter fibre sensor for oil and gas based applications, the theoretical models of the cross sensitivity function have been developed and analysed. The simulated results which show the interactions between the physical properties of FBG and cross sensitivity depict that the cross sensitivity would change widely when external perturbations and fibre materials effects are very large. This is particularly very important for the selection of fibre parameters and coating materials during fabrication.

To resolve the problem of cross sensitivity and improve the measurement accuracy of the FBG, the theoretical models of the cross sensitivity term affected by external fields, fibre material are deduced. The effects of the cross sensitivity on the measurement results are discussed by the numerical simulation with external fields. We can conclude that if the changes of external parameters are great enough, a theoretical correction can be conducted according to different environment. Besides, certain parameters of the fibre can be selected to fabricate FBG to reduce the effect of the cross sensitivity on the measurement results.

The interaction of the physical parameters and light wave properties pose a serious cross sensitivity challenge to the reliability of the sensor [21 21]. Unfortunately theoretical models and analysis in addressing this challenge have been missing in literature. An effective model to address the behaviour of this interaction between the physical parameters and light wave properties is desired. This research addresses this problem by considering several sensor design configurations and analysed this interaction.

Chapter 4 introduces the well-known FP interferometer sensor configuration to investigate and analyse the spectral characterization of an FP sensor and the interaction with physical parameters. Preliminary results of this configuration is used to eliminate the issue of temperature-pressure cross-sensitivity and effectively improve the resolution of the sensor system.

The concept of a metal coated hybrid sensing system is proposed in chapter 5. The theoretical design and analysis of a metal coated sensor is carried out. In this chapter, the model combines both optical and structural analysis to develop an optimal sensor system design that effectively tackle the issue of cross sensitivity.

Lastly, miniature optical fibre sensor for high pressure and high temperature harsh environments using graphene diaphragm is reported in chapter 6. The interaction between the graphene layer, light properties and the physical parameters is analysed. This numerical analysis and simulation showed that the propose sensor exhibits; an excellent temperature response with good linearity and high sensitivity. The effect of temperature pressure cross sensitivity was eliminated.

3.7 References

[1] S. Shaari and S. Mah Chee, "Characteristics of large bandwidth fiber Bragg grating with short grating length," in *ICSE 2000. 2000 IEEE International Conference on Semiconductor Electronics. Proceedings*, pp. 203-206, 2000.

[2] W. Ecke, K. H. Jäckel, J. Schauer, and R. Willsch, "High Temperature Interferometric Displacement Measuring System for Fibre Optic Seismic

Sensors in Deep Borehole Applications," in *Optical Fiber Sensors*, Sapporo, 1996.

[3] A. Othonos and K. Kalli, *Fiber Bragg Gratings: Fundamentals and Applications in Telecommunications and Sensing*: Artech House, 1999.

[4] Y.-J. Rao, "In-fibre bragg grating sensors," Measurement science and technology, vol. 8, pp. 355–375, 1997

[5] T. Erdogan, "Fiber grating spectra," *Journal of Lightwave Technology,* vol. 15, pp. 1277-1294, 1997.

[6] W. W. Morey, G. Meltz, and W. H. Glenn, "Fiber Optic Bragg Grating Sensors," pp. 98-107, 1990.

[7] M. Yamada and K. Sakuda, "Analysis of almost-periodic distributed feedback slab waveguides via a fundamental matrix approach," *Applied Optics,* vol. 26, pp. 3474–3478, 1987.

[8] K. Ravijot and S. B. Manjit, "Effect of Grating Length on Reflection Spectra of Uniform Fiber Bragg Gratings," *IJITT,* vol. 3, pp. 63-67, 2011.

[9] I. Abdallah, H. Rachida, and C. Mohamed, "Uniform Fiber Bragg Grating Modeling and Simulation used Matrix Transfer Method," *IJCSI,* vol. 9, pp. 368-374, 2012.

[10] H. S. Phing, J. Ali, R. A. Rahman, and B. A. Tahir, "Fiber Bragg Grating Modeling, Simulation and Characteristics with different Grating Lengths," *Journal of Fundamental Sciences,* vol. 3, pp. 167-175 2007.

[11] A. Dinesh, P. Jai, S. Hardeep, and W. Amit, "Reflectivity and Bragg Wavelength in FBG," *International Journal of Engineering Science and Technology,* vol. 5, pp. 341-349, 2011.

[12] U. Sunita and V. Mishra, "Fiber Bragg Grating Modeling, Characterisation and Optimization with different Index Profiles," *International Journal of Engineering Science and Technology,* vol. 2, pp. 4463-4468, 2010.

[13] A. Tahir, J. Ali, and R. A. Rahman, "Strain Measurement using FBG Sensor," *American Journal of Applied Science,* pp. 40-48, 2005.

[14] R. Yun-Jiang, D. J. Webb, D. A. Jackson, Z. Lin, and I. Bennion, "In-fiber Bragg-grating temperature sensor system for medical applications," *Journal of Lightwave Technology,* vol. 15, pp. 779-785, 1997.

[15] C. G. Askins, M. A. Putnam, and E. J. Friebele, "Instrumentation for interrogating many-element fiber Bragg grating arrays,", pp. 257-266, 1995.

[16] A. D. Kersey, M. A. Davis, H. J. Patrick, M. LeBlanc, K. P. Koo, C. G. Askins, M. A. Putnam, and E. J. Friebele, "Fiber grating sensors," *Journal of Lightwave Technology,* vol. 15, pp. 1442-1463, 1997.

[17] A. D. Kersey, T. A. Berkoff, and W. W. Morey, "Multiplexed fiber Bragg grating strain-sensor system with a fiber Fabry–Perot wavelength filter," *Optics Letters,* vol. 18, pp. 1370-1372, 1993.

[18] A. D. Kersey, J. R. Dunphy, and A. D. Hay, "Optical Reservoir Instrumentation System.", Offshore Technology Conference, 4-7 May, Houston, Texas, 1998.

[19] K. T. V. Grattan and T. Sun, "Fiber optic sensor technology: an overview," *Sensors and Actuators A: Physical,* vol. 82, pp. 40-61, 2000.

[20] M. f. Zhao, S. f. Wang, B. b. Luo, N. b. Zhong, and X. m. Cao, "Theoretical Study on the Cross Sensitivity of Fiber Bragg Grating Sensor Affected by Temperature and Transverse Pressure," *Symposium on Photonics and Optoelectronics*, pp. 1-4, 2010.

[21] G.-h. Han and W.-g. Zhang, "Method of correlation function for analyzing cross-sensitivity of strain and temperature in fiber grating sensors," *Optoelectronics Letters,* vol. 3, pp. 195-198, 2007.

Chapter 4

4 Preliminary Investigation of Temperature and Pressure Measurement System for FBG/EFPI Sensing Technique

4.1 Introduction

As described from the theoretical analysis and numerical simulation in Chapter 3, when an FBG sensor is subject to external parameters, the interactions between the physical properties of the sensor and the properties of cross sensitivity could change widely when external parameters and fibre material effects are very large. To overcome this limitation and minimise the effect of cross sensitivity in a FBG sensor, a multiplexed FBG/EFPI sensor for simultaneous measurement of temperature and pressure is presented. The optical fibre used is made of fused silica for downhole monitoring in oil and gas wells. Analysis of the spectral characterizations (basic sensor system configuration, finesse, fringe visibility, sensor mechanical analysis which includes diaphragm deflection, frequency response and stress distribution) are presented and a de-multiplexing mathematical model for the multiplexed sensor is proposed. This configuration is used to eliminate the issue of temperature-pressure cross-sensitivity and effectively improve the resolution of the sensor system. Experimental results show good linear relationship between the Bragg wavelength shift and the physical parameters (temperature and pressure), high sensitivity and high accuracy.

In this work, the following contributions are made:

- Design and development of a sensor head comprising the use of FBG and EFPI for simultaneous measurement of temperature and pressure in permanent downhole monitoring of oil and gas wells.
- Analysis of the spectral characterization of the multiplexed FBG and EFPI and the proposed mechanism for separating the FBG response from the EFPI.
- Establishing a de-multiplexing mathematical model for the FBG and EFPI multiplexed sensor for temperature and pressure measurements respectively.

The EFPI sensors have been designed and implemented for various physical parameter measurements such as temperature and pressure for downhole monitoring [1-8]. This is due to its high accuracy, resolution and reliability [6]. Its unique structure makes it possible to measure high pressure with minimal temperature cross-sensitivity. However, an EFPI sensor cannot be multiplexed, therefore it cannot perform distributed sensing along the fibre. FBG sensors are another type of optical based sensor used in downhole monitoring of temperature and pressure measurement [4, 9-11]. The FBG based sensors have distinctive advantages over the conventional electronic sensors and other optical fibre sensors due to its multiplexing capability that allows a single fibre with tens of gratings to carry out a wide range of parameter measurements with a simple package structure [12]. The limitation of FBG in measuring physical parameters is the issue of high temperature-pressure cross-sensitivity [13].

In this work, we present a sensor system design that combines the advantages of the simple structure of FBG for temperature measurement and high accuracy low temperature-pressure cross-sensitivity of the EFPI pressure sensor. This

configuration is used to eliminate the issue of temperature-pressure cross-sensitivity and effectively improve the resolution of the sensor system.

4.2 Theory and principles of fibre Bragg grating (FBG) and extrinsic Fabry-Perot interferometer (EFPI)

Charles Fabry and Alfred Perot first proposed the concept of FPI to analyse the wavelength of light spectrum [14]. The schematic structure of the multiplexed FBG/EFPI sensor is shown in Figure 4.1. The white light broadband source is coupled into the single mode fibre. The light is propagated to the sensing head and the coupled reflected interference signal from the sensing head is passed through a 2x2 $3\,dB$ fibre coupler to an optical spectrum analyzer. As shown in Figure 4.1, the light propagation is reflected at the FBG, the end-face of the fibre and the inside and outside interfaces of the diaphragm. The end-face of the fibre and the interfaces of the diaphragm formed a low-finesse EFPI. By 'low-finesse' it refers to a weak reflection created by these interfaces. The FBG has a narrow bandwidth with high reflectivity whereas in the low-finesse EFPI, a fraction of the incident light (4 %) is reflected first at the end-face of the fibre and is coupled back into the fibre. The remaining transmitted light propagates into the air cavity of the inside and outside interfaces of the diaphragm. The reflections at the interfaces are recoupled back into the fibre to form an interference pattern. The interference formed is as a result of the phase difference between the transmitted and reflected light which is dependent on the low-finesse EFPI cavity length l. Due to the weak reflection of the endface of the fibre, multiple reflections have negligible contribution to the interference pattern formed.

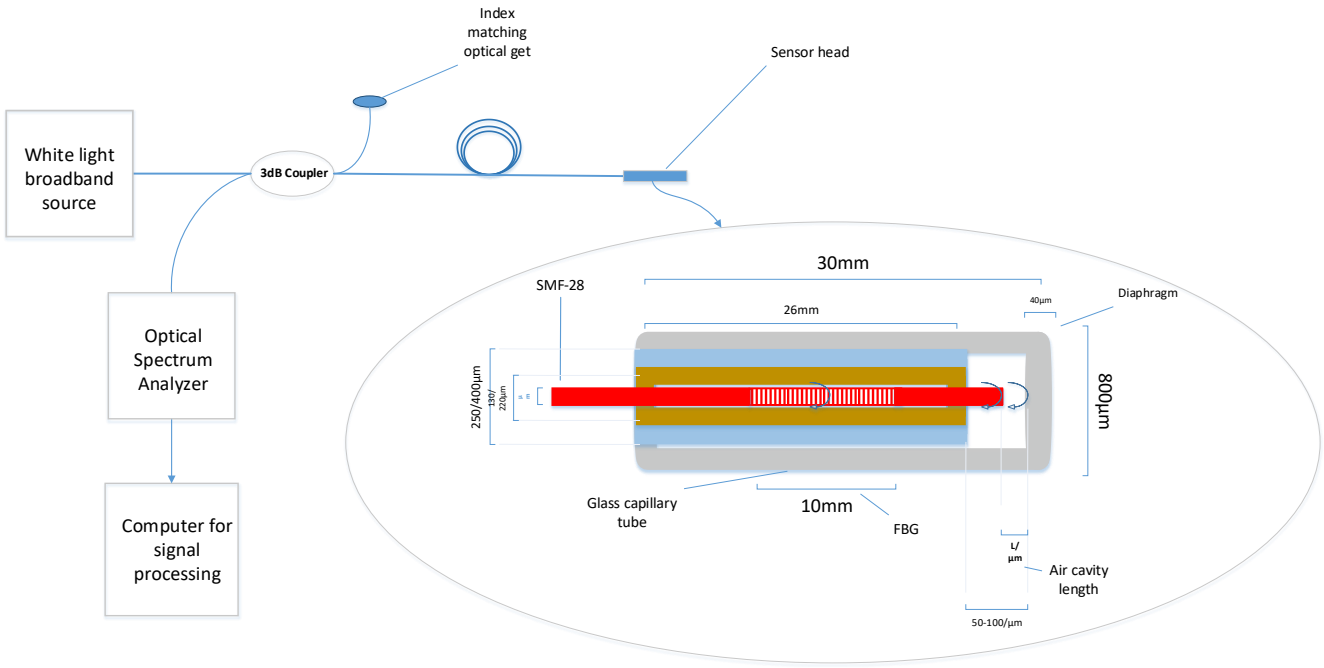

Figure 4.1 Schematic of the FBG/EFPI sensing configuration (sensing head showing configuration and dimensions)

A schematic of the EFPI cavity between the end-face of the optical fibre and the reflective mirror image is shown in Figure 4.1. It can be shown that the light is reflected back and forth between the fibre end-face and the reflected mirror image and others are transmitted from the cavity onto the reflected mirror image. Assuming normal incidence, the reflection coefficient r according to Fresnel law can be expressed as [6];

$$r = \frac{(n_1 - n_2)^2}{(n_1 + n_2)^2} \tag{4.1}$$

where n_1 and n_2 are the refractive indices of both the optical fibre and the reflective material respectively. For simplicity, the optical modulation of the signal is assumed to be two-beam interference and the optical path difference

between these two beams is given by Δd. Due to the weak reflection of the end-face of the fibre, multiple reflections have negligible contribution to the interference pattern formed. The interference pattern induced by the low-finesse EFPI can be expressed as [15, 16]

$$I(\lambda, L) = I_1^2 + I_2^2 + 2I_1 I_2 cos\left(\frac{4\pi nL}{\lambda} + \varphi_0\right) \quad (4.2)$$

where I_1 and I_2 are the light intensities reflected at the endface of the SMF-28 and the interface of the diaphragm respectively, n is the refractive index of the air cavity, L is the EFPI cavity length, φ_0 is the arbitrary initial phase difference and λ is the optical wavelength.

The analytical expression for the reflected light power of EFPI is given by [16]

$$P = \frac{Fsin\left(\frac{\varphi}{2}\right)^2}{1 + Fsin\left(\frac{\varphi}{2}\right)^2} \quad (4.3)$$

where P is the total light reflected power with respect to the phase φ, F is the coefficient of finesse defined as

$$F = \frac{4R}{(1-R)^2} \quad (4.4)$$

F measures the broadness of the spectrum peaks, R is the coefficient of reflection power. φ is the phase which is expressed as

$$\varphi = \frac{4n_c l}{\lambda} \quad (4.5)$$

$n_c l$ is the optical path difference, n_c is the index of refraction, l is the path length and λ is the wavelength.

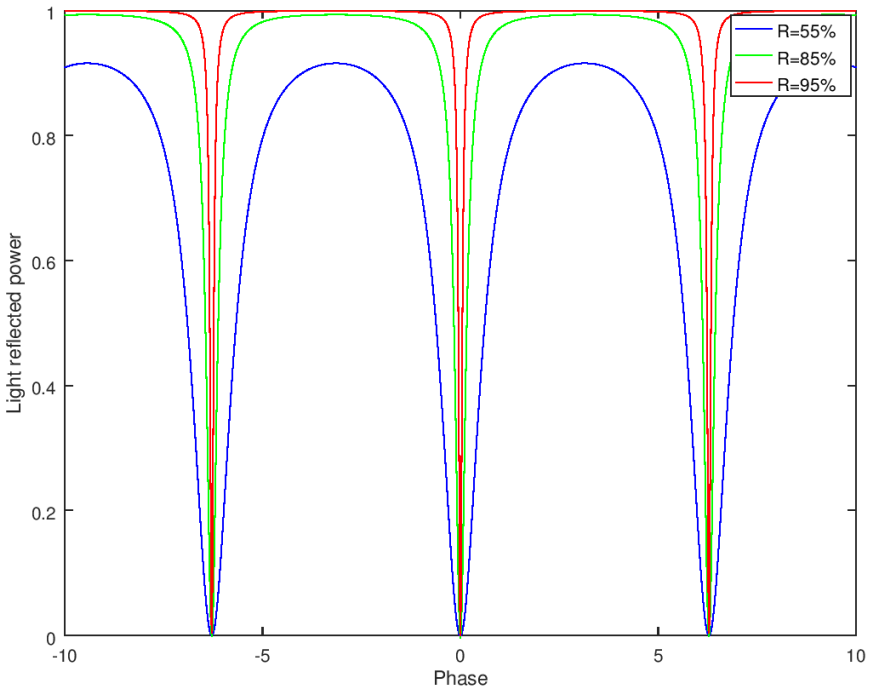

Figure 4.2 Intensity for mirror reflectivity of R=55%, R=85% and R=95%

The reflected intensity for the mirror reflectivities of $R = 55\%$, $R = 85\%$ and $R = 95\%$ is shown in Figure 4.2. As the reflectivity increases, the peak becomes flat and the bandwidth increases. This is as a result of the EFPI to conserve energy as the mirror reflectivity increases. Equation 4.5 showed the inverse relationship between the phase value and the wavelength. Figure 4.3(a) shows the calculated phase shift φ as a function of path length l for a standard SMF at a wavelength of $\lambda = 1550\, nm$. The phase shift increases from 30° to $98°$ when the path length is changed from 0 to $100\, \mu m$. As the phase value decreases, the wavelength increase as shown in Figure 4.3(b).

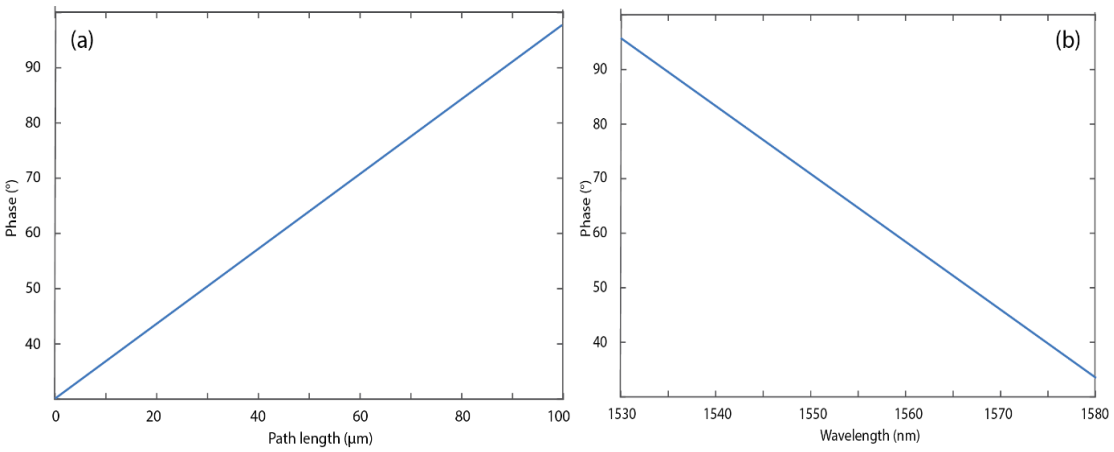

Figure 4.3 Calculated phase shift as a function of both path length and wavelength. (a) Phase shift as a function of path length l (b) Phase shift as function of wavelength λ

The coefficient of finesse F also increases as R increase resulting in narrow peak. The maximum reflected power occurs when $sin\left(\frac{\varphi}{2}\right)^2 = 1$ (criterion for both constructive and deconstructive interference). $\varphi = (2m+1)\pi$ for constructive interference and $\varphi = 2\pi m$ for destructive interference, where m is an integer, both leading to ${}^{m\lambda}/_{4} = nl$ and ${}^{m\lambda}/_{2} = nl$ respectively.

Assuming the index of refraction n_c to be 1, the constructive interference will be a multiple of a quarter wavelength of the optical thickness while for deconstructive interference, the wavelength will be a multiple of the optical thickness.

The finesse is one important parameter that measures the performance of the EFPI. It is referred to as the ratio of the free spectra range (FSR) to the full width at half maximum (FWHM) which is expressed as;

$$\mathcal{F} = \frac{FSR}{FWHM} \tag{4.6}$$

The FSR is defined by

$$FSR = \frac{{\lambda_0}^2}{2nl} \tag{4.7}$$

where λ_0 is the wavelength of the first reflectance minima, and nl is the optical thickness of the FP. The equation indicates that FSR has an inverse relationship with nl which shows that as FSR decreases, the cavity length increases.

4.2.1 Fringe Visibility of EFPI sensor

Fringe visibility is another measure of performance of the EFPI. This performance parameter is so important because it helps in the design, optimization and fabrication of the sensor. The visibility is the measure of depth of the reflectivity peak which is defined as

$$V = \frac{P_{max} - P_{min}}{P_{max} + P_{min}} \tag{4.8}$$

where P_{max} is the maximum reflected power, P_{min} is the minimum reflected power in the reflected mode. For a non-converging beam, the visibility is always 1 [19]. In practical applications, the fringe visibility can be measured in two different ways depending on the light source of that application. For laser-based FP sensor systems, where the fringes are a function of the path length and the light wavelength is fixed, the fringe visibility is measured by carefully tuning the path length of the FP cavity and reading the maximum and minimum output of the power. In a white-light sensor systems, spectrometer is used to measure spectral fringes directly and the maximum and minimum output power are easily readable. Also, the two surfaces on the FP sensor system are not parallel to each other because of the limitation in fabrication accuracy. This causes the

FP cavity thickness to vary and has the cavity geometry to become that of a wedge. Here, the impact of the wedge on fringe visibility is studied and analysed. The surface roughness of the lead-in fibre and the mirror image caused as a result of the wedge is considered in this design. Due to the extreme high temperature operations, the fibre in the sensor system could easily deform which can introduce most of the surface roughness, imperfection and misalignment.

In this analysis, the assumption that the reflectivity of the surface plane of the lead-in fibre is perpendicular to the fibre axis z, while the reflectivity is tilted to form a wedge angle of θ with respect to the reflectivity of the of the surface plane of the lead-in fibre. The essence of this wedge is to produce a linear phase change across the beam and a spatial displacement between the electric fields of both the lead-in fibre and the reflected mirror at the surface plane of the mirror image. From the expression of the interference signal

$$I(\lambda, l) = (E_1 + E_2)(E_1 + E_2)^*$$

$$= I_0(\lambda)K\left[1 + |\eta|\cos(\frac{4\pi l}{\lambda} + \pi - \varphi(\lambda, l))\right] \quad (4.9)$$

where $I(\lambda, l)$ is the initial light source power spectrum, K is a transmission and reflection loss at the two ends and η is the coupling coefficient. The normalised spectrum is then expressed as

$$I(\lambda, l) = 1 + |\eta|\cos(\frac{4\pi l}{\lambda} + \pi - \varphi(\lambda, l)) \quad (4.10)$$

This expression shows that the interferometer signal is not only affected by the length of the propagation in free space but also the light coupling from free space back to the lead-in fibre. The effect of the FP cavity optical path length between the end-faces on the fringe visibility is shown in Figure 4.4. This shows the fringe visibility as a function of the path length at different wedge angles. Overall, its seen that the fringe visibility decreases with increase in path length.

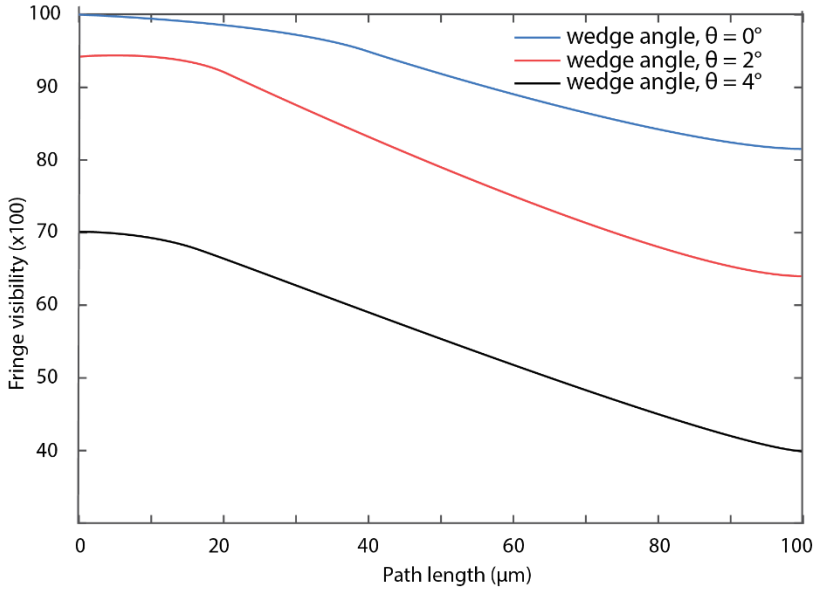

Figure 4.4 Fringe visibility as a function of path length for different wedge angles

For a perfect sensor (sensor with no surface roughness, wedge angle = $0°$), the fringe visibility drops from 100% to 81% (by 19%) when the path length increases from 0 to $100\ \mu m$, 95% to 65% (30%) for the sensor with wedge angle of $2°$ and 30% (from $70\%\ to\ 40\%$) for the sensor with wedge angle of $4°$. The fringe visibility decreases more quickly as the path length decreases for each wedge. For the perfect sensor with wedge angle of $0°$, the visibility decreases by 19% when the path length increases from 0 to $100\ \mu m$. However, the visibility

drops by 3.9% when the path length increases for 0 to $40\,\mu m$. In most practical applications, the path length of the sensor is usually less than $100\,\mu m$. Therefore, the fringe visibility degradation with respect to the path length is acceptable to most practical applications. Significant large wedge angles can cause a decrease of fringe visibility; in this case, care must be taken when focusing laser light to obtain a more acceptable fringe visibility.

4.2.2 Diaphragm model and analysis

The diaphragm mechanical model and analysis considers the deflection of the diaphragm under static and dynamic pressure. The EFPI cavity length l changes with deflection of the diaphragm when there is difference in pressure between the inside and outside surfaces of the diaphragm. The diaphragm theory is particularly important in understanding the key parameters that can influence the diaphragm performance. The thickness, diameter and thickness can all be optimised to enhance the sensor performance. Some of the diaphragm characteristics to be covered in this section are the diaphragm deflection, frequency response and pressure sensitivity.

4.2.3 Diaphragm deflection under pressure

The variation of the cavity length ΔL under the influence of pressure difference ΔP is expressed in equation 4.11 [17], where r is the radius of the diaphragm defined by the inner diameter of the outer capillary tube, h is the thickness of the diaphragm, E is Young's Modulus and ν is Poisson's ratio.

$$\Delta L = \frac{3(1-\nu^2)r^4}{16Eh^3}\Delta P \tag{4.11}$$

The structure of the diaphragm when pressure is applied is depicted in Figure 4.5.

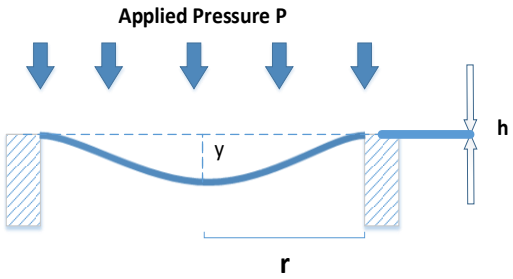

Figure 4.5 Deflection curve of diaphragm under Pressure

The sensitivity of the diaphragm can be expressed as [15]

$$\partial_{dia} = 1.71 \times 10^{-8} \times \frac{r^4}{h^3} \quad (^{\mu m}/_{kPa}) \tag{4.12}$$

The deflection curve when subject to pressure difference is given as

$$y = \frac{3(1-\nu^2)r^4}{16Eh^3}\left[1-\left(\frac{a}{r}\right)^2\right]^2 = y_{max}\left[1-\left(\frac{a}{r}\right)^2\right]^2 \tag{4.13}$$

This expression is only valid when the deflection is less than or equal to 30% of the diaphragm thickness (i.e $y_{max} \leq 0.3h$)

Figure 4.6 shows the deflection variation from the minimum point at the edges to the maximum point at the centre for a circular diaphragm.

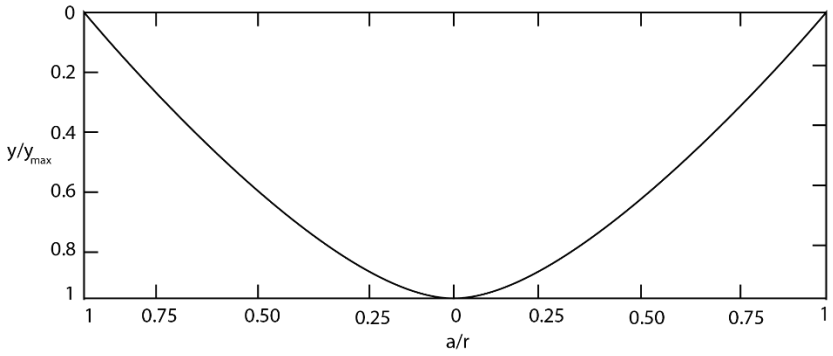

Figure 4.6 Diaphragm deflection curve when subject to applied pressure

MATLAB was used to carry out a three dimensional simulation of the diaphragm deflection as shown in Figure 4.7

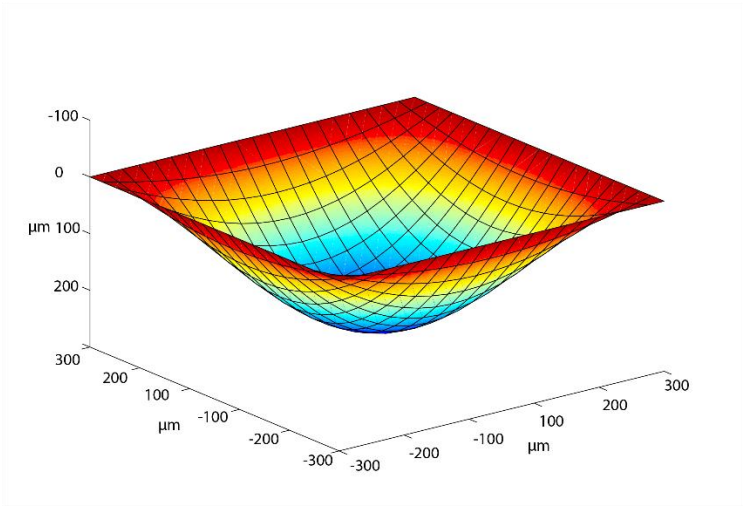

Figure 4.7 Three dimensional simulation of the diaphragm deflection under applied pressure

For measurement of static and dynamic high pressure with high sensitivity, the EFPI cavity length, the thickness and diameter of the diaphragm are key parameters that need to be properly analysed. The diaphragm diameter is usually measured or determined from the capillary geometry. In this case, the

radius of the diaphragm is the same as the radius of the inner diameter of the outer capillary tube.

Knowing the pressure range to be measured, the minimum thickness of the diaphragm needs to be ascertained. This is expressed in the following equation [18].

$$h_{min} = r\left(\frac{5(1-\nu^2)P_{max}}{8E}\right)^{\frac{1}{4}} \tag{4.14}$$

In Figure 4.8(a), it can be seen that to sense high pressure, the thickness of the diaphragm and the diameter must be reasonably high. As a rule of thumb, in order to obtain a linear response of the diaphragm, the maximum deflection due to applied pressure should not exceed 30% of the diaphragm thickness.

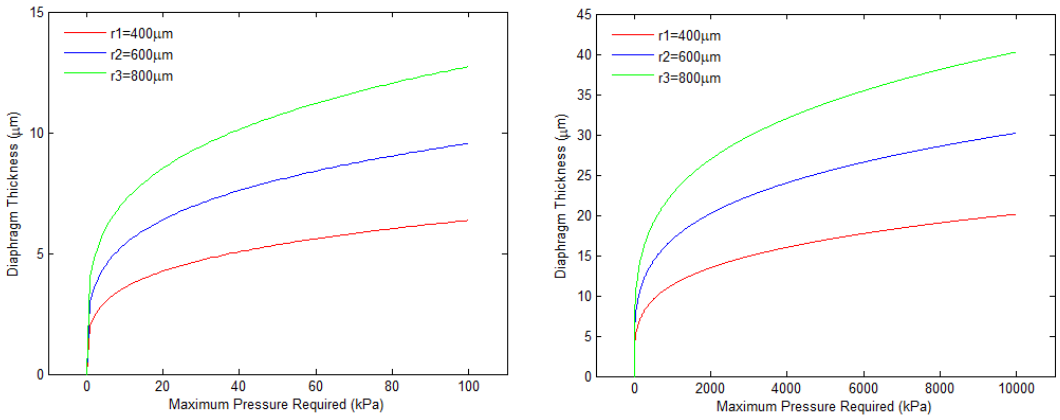

Figure 4.8 Simulated diaphragm thickness against maximum pressure required (a) shows for large pressure range (b) small pressure range

Figure 4.8(a) shows that for a diaphragm thickness with radius of $600\,\mu m$, for applied pressure of $5000 - 10000\,psi$, the thickness should be approximately between $25 - 30\,\mu m$. For applied pressure of $10 - 20\,kPa$, the thickness should be approximately between $5 - 10\,\mu m$ as shown in Figure 4.8(b). This shows that

for pressure measurement, a diaphragm with high diaphragm deflection sensitivity is required.

4.2.4 Diaphragm sensitivity

The sensitivity of the diaphragm to pressure difference, as one of the most important performance indexes, is defined by the ratio of the deflection y to the applied pressure [15].

$$\partial_{dia} = \frac{y}{P} = \frac{3(1-\nu^2)r^4}{16Eh^3} \tag{4.15}$$

The simulation result of the pressure sensitivity with respect to the diaphragm thickness is shown in Figure 4.9. This shows that the pressure sensitivity is inversely proportional to the diaphragm thickness.

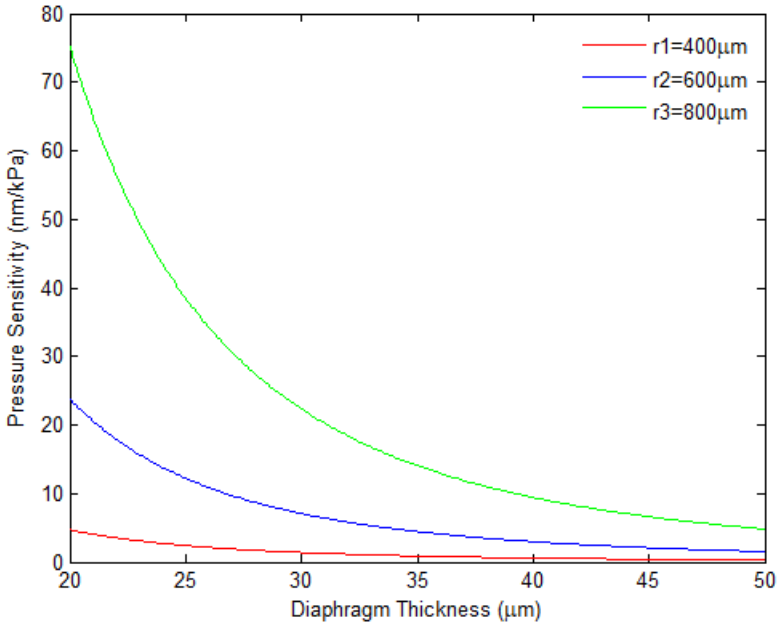

Figure 4.9 Simulated pressure sensitivity of the sensor for different diaphragm effective radius

4.2.5 Diaphragm frequency response

The diaphragm frequency response is another very important design consideration for the sensing head performance after the sensitivity of the diaphragm. When the diaphragm is modelled at a free vibrating circular plate that is clamped solidly at the edge, the natural frequency $f_{mn}\,(Hz)$ is expressed as [17]

$$f_{mn} = \frac{\alpha_{mn}}{4\pi}\sqrt{\frac{E}{3w(1-\nu^2)}}\left(\frac{h}{r^2}\right) \tag{4.16}$$

where α_{mn} is a constant related to the vibrating modes of the diaphragm and w is the mass density of the diaphragm material. For aluminium, the lowest natural frequency, $\alpha_{00} = 10.21$ [19], the frequency response of the diaphragm can be calculated as

$$f_{00} = 2.742 \times 10^9 \times \frac{h}{r^2} \quad (Hz) \tag{4.17}$$

For the diaphragm to respond to dynamic applied pressure, the sensor natural frequency should be at least $3-5$ times higher than the applied frequency [16]. Figure 4.10 shows that the natural frequency response of the sensor is proportional to the diaphragm thickness and inversely proportional to the square of the effective radius. This is contrary to the sensitivity of the diaphragm as depicted in Figure 4.9. Therefore, a trade-off is applied to the sensor design. For the purpose of this work, a diaphragm thickness of $40\,\mu m$ and effective radius of $800\,\mu m$ is selected. This gives the pressure sensitivity of $9.4\,nm/kPa$ and a natural frequency of $271.4\,kHz$.

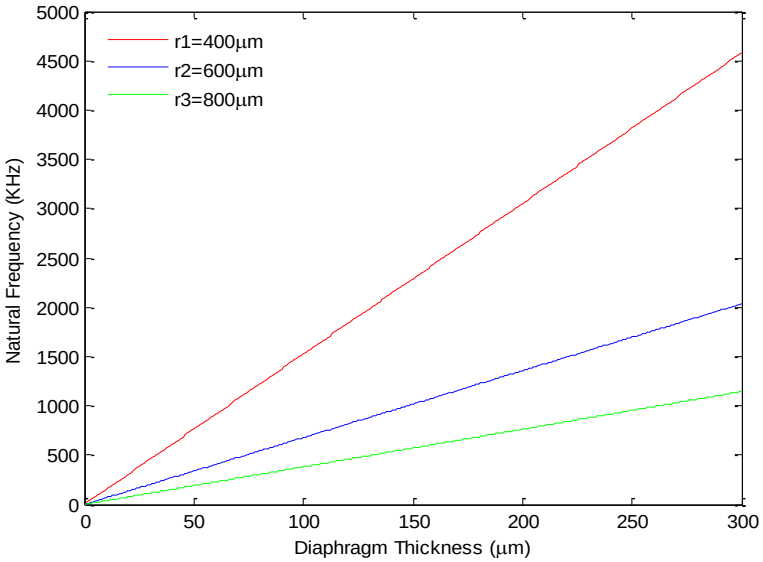

Figure 4.10 Simulated natural frequency of the sensor as against diaphragm thickness

4.3 FBG sensor model analysis

The shift in Bragg wavelength is related to the coefficient of thermal expansion, refractive index variations and the grating period. The shift in wavelength $\Delta\lambda_{B|T}$ as a result of temperature changes ΔT is described by [20]

$$\Delta\lambda_{B|T} = \lambda_B(\alpha + \xi)\Delta T \tag{4.18}$$

$$\alpha = \frac{1}{\Lambda}\left(\frac{\partial\Lambda}{\partial T}\right)$$

$$\xi = \frac{1}{n_{eff}}\left(\frac{\partial n_{eff}}{\partial T}\right)$$

where α is the thermal expansion coefficient and ξ is the thermo-optic coefficient. Study has also shown that the temperature sensitivity of a typical bare optical fibre is given as $13.7\,pm/℃$ at a wavelength of $1550\,nm$, corresponding to a change of $13.7\,pm$ for applying a temperature of $1℃$ to the fibre grating [20]. An example of a Bragg wavelength shift due to applied temperature on a $1548.20\,nm$ gratings is shown in Figure 4.11.

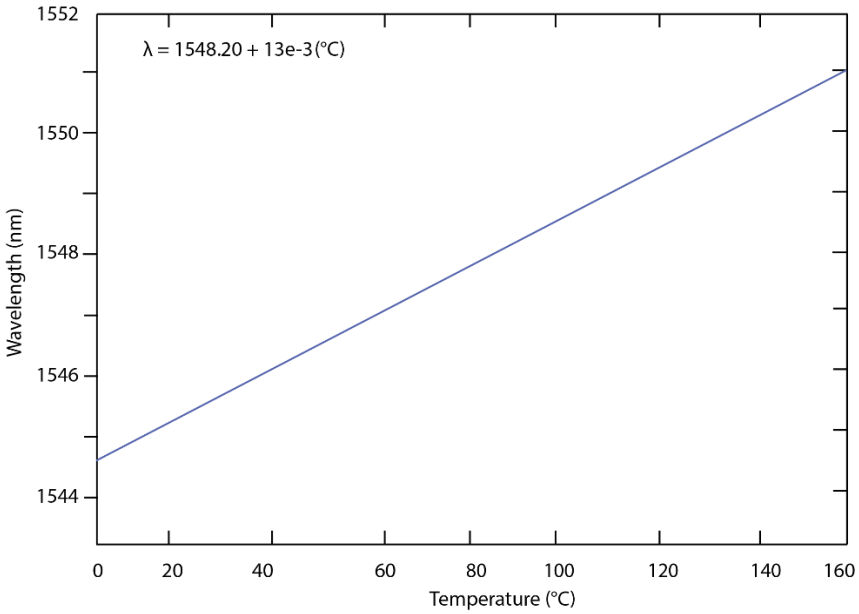

Figure 4.11 Bragg wavelength shift with applied temperature on a $1548.20\,nm$ gratings

4.4 Fabrication of the multiplexed sensor head

The performance of the sensor is very much dependent on the material selection. The properties of the selected material such as the thermal expansion coefficient, strength of the material, thermal conductivity, melting and boiling points etc affect the performance of the sensor. Also, the quality during fabrication affects the sensor performance. In this section, the detail of the sensor head fabrication is described.

The multiplexed sensor was fabricated (Figure 4.12) using a single mode SMF-28 $9/125\ \mu m$, $120/220\ \mu m$ inner/outer diameter glass capillary and a diaphragm made of aluminum with thickness of $40\,\mu m$ and diameter of $800\,\mu m$ from design specification shown in Figure 4.1. The end-face of the SMF-28 and the glass capillary were polished to give smooth surfaces and the SMF-28 was fed into the glass capillary making sure that the FBG was placed centrally within the glass capillary. The $120/220\ \mu m$ glass capillary with the SMF-28 was inserted into another glass capillary of $250/800\ \mu m$ inner/outer diameter to keep the FBG from external strain and pressure. The SMF-28 was bonded to the inner glass capillary providing a displacement of approximately $100\,\mu m$ from the tip of the SMF-28 to the diaphragm and the inner capillary also was bonded to the outer capillary. The cleaved end of the outer capillary was bonded to the diaphragm.

Figure 4.12 Fabricated multiplexed FBG/EFPI sensor head (The sensing head placed close to a pound coin to show the small size)

4.5 Sensor signal processing and interrogation

The normalised reflection spectrum of the FBG/EFPI based multiplexed sensor is shown in Figure 4.13. The reflected Bragg wavelength peak of the FBG can be easily detected and read by the optical spectrum analyzer (Yokogawa AQ6375B OSA) at $1550\,nm$ which makes the temperature to be modulated independent from the effect of pressure.

The EFPI cavity reflection interference spectrum relationship of the sensor head is given in equation 4.2. When the cavity length of the EFPI changes, there is a corresponding shift in the spectrum and the interference frequency fringe changes in the wavelength domain. The cavity length can be measured by tracking the variation of the interference frequency fringe.

From literature, signal processing methods such as two-point peak wavelength interrogation [19], wavelength-tracking [20] and Fourier transform [21] techniques have been widely reported and used to calculate the cavity length of EFPI based sensors. All these spectral domain signal processing methods are based on equation 4.2 which relates the interference frequency fringe to the cavity length of the EFPI sensor.

The two-point interrogation method is simple, and capable of absolute measurement. It has high resolution, accuracy and speed of measurement. The linear range is also very high. The peak wavelength-tracking method is not capable of absolute measurement and the measurement range is very limited. The Fourier transform method is capable of absolute measurement and has a large linear range. It has a high resolution but the accuracy is rather low.

In this work, the two-point interrogation method of signal processing is applied to demodulate the interference signal because of its simple nature and advantages. The FP cavity length can be expressed as

$$L = \frac{\lambda_1 \lambda_2}{2(\lambda_1 - \lambda_2)} \tag{4.19}$$

where $\lambda_1 > \lambda_2$ and they are the wavelength of the two adjacent peak points in the interference spectrum.

The interference spectrum of the multiplexed sensor head must be de-multiplexed by the signal processing instrumentation before accurate measurement of temperature and pressure can be determined. In order to accurately model the de-multiplexed FBG/EFPI sensor head, the noise in the interference signal must be removed. This is true because the noise in an FBG and EFPI demodulated signal is seen as mainly Gaussian white noise.

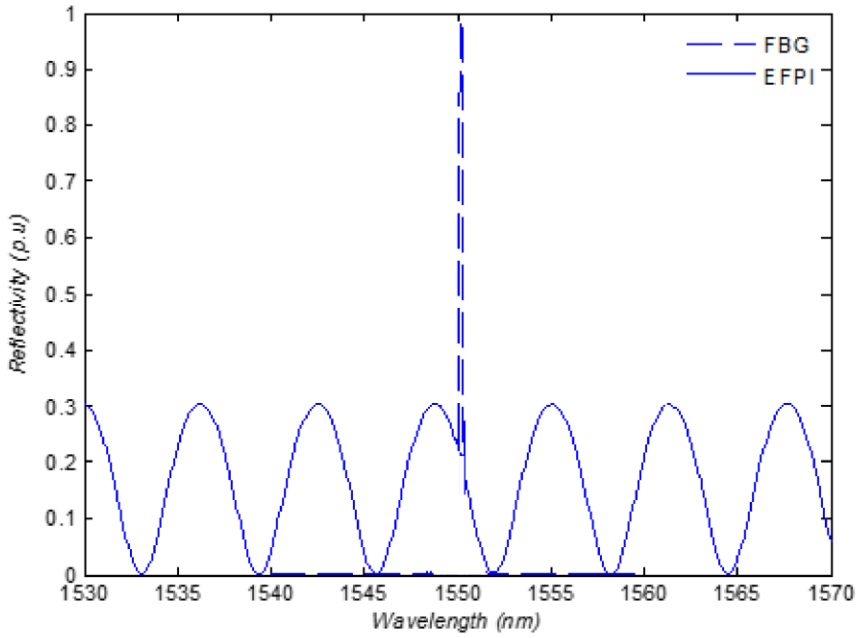

Figure 4.13 Reflection spectrum of FBG/EFPI multiplexed sensor

When the light with intensity I_{in} from the white light broadband source is incident on the FBG, there is a narrow band reflection which can be expressed as $I_1 = I_{in}\, F_{fbg}(\lambda)$

where $F_{fbg}(\lambda)$ is the reflection spectrum of FBG which can be described by the Gaussian function, where ε_i is the measurement error.

$$F_{fbg}(\lambda) = R\ exp\left\{\frac{-(\lambda_1-\lambda_B)^2}{c^2}\right\} + \varepsilon_i \qquad (4.20)$$

The remaining light signal is transmitted through the FBG and it is represented as I_2 which can be expressed as

$$I_2 = I_{in} - I_1 = I_{in}\,(1 - F_{fbg}(\lambda)) \tag{4.21}$$

The transmitted light signal I_2 is incident on the EFPI cavity sensor which is reflected to form an interference fringe pattern I_3 expressed as $I_3 = I_2 F_{fp}(\lambda)$ where $F_{fp}(\lambda)$ is the reflection spectrum of the EFPI interference fringe pattern and this is expressed as an approximation of Equation 4.2 to be

$$F_{fp}(\lambda) = 2r\left[1 + cos\left(\frac{4\pi L}{\lambda} + \varphi\right)\right] \tag{4.22}$$

where r is the low-finesse reflectivity of the SMF-28 endface, φ is the arbitrary initial phase difference, L is the cavity length and λ is the reflected wavelength. The reflected signal from the EFPI cavity is transmitted through the FBG again to give a signal of I_4 expressed as

$$I_4 = I_3\left(1 - F_{fbg}(\lambda)\right) = I_{in}\left(1 - F_{fbg}(\lambda)\right)^2 * F_{fp}(\lambda) \tag{4.23}$$

The total reflected signal from the multiplexed sensor head is given as $I_{out} = I_1 + I_4$

$$I_{out} = I_{in}\left[F_{fbg}(\lambda) + (1 - F_{fbg}(\lambda))^2 * F_{fp}(\lambda)\right] \tag{4.24}$$

From equation 4.24, the reflection spectrum of the interference pattern is not just a simple sum of both the FBG and EFPI reflection spectra. During the signal processing, the FBG reflection peak wavelength along with the EFPI spectrum will cause the result to offset the effect of temperature measurement accuracy of the FBG. To get the accurate FBG reflection spectrum signal of the FBG, equation 4.24 is expanded to form a quadratic equation and the solution gives the accurate FBG reflection spectrum. A Gaussian nonlinear curve fit is used to obtain the peak of the spectrum.

$$F_{fp}(\lambda) * {F_{fbg}}^2(\lambda) + \left(1 - 2F_{fp}(\lambda)\right) * F_{fbg}(\lambda) + F_{fp}(\lambda) + \frac{I_{out}}{I_{in}} = 0 \quad (4.25)$$

The FBG demodulated signal is obtained as the solution of the quadratic equation of the multiplexed signal given as

$$F_{fbg}(\lambda) = \frac{-\left(1-2F_{fp}(\lambda)\right) \pm \sqrt{\left(1-2F_{fp}(\lambda)\right)^2 - 4F_{fp}(\lambda)(F_{fp}(\lambda) - {I_{out}}/{I_{in}})}}{2F_{fp}(\lambda)} \quad (4.26)$$

4.6 Experiment and Discussion

To evaluate the signal processing, demodulation system performance and the developed sensor head, a testing system was setup. This experiment was carried out in collaboration with the International School of Photonics, Cochin University of Science and Technology, Cochin, India. A temperature controlled oven for temperature measurement was used. The temperature range of the oven is from room temperature to $400\ ℃$. Also, hydrostatic pressure was applied to the sensor head as shown in Figure 4.14. A water column of height $80\ cm$ was filled with water. The sensor head was immersed into the water column to

a height of $20\,cm$ from the top of the water level and the initial spectrum was taken by the OSA. The hydrostatic pressure was then increased by incrementing the height by $10\,cm$ and further spectral readings were taken. The pressure varies linearly as a function of height.

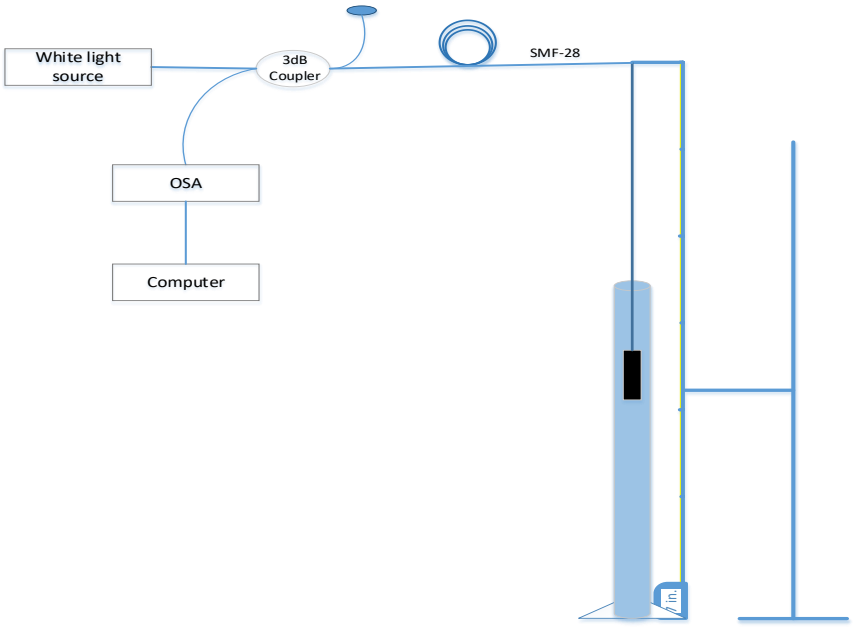

Figure 4.14 Experimental setup for pressure measurement

Figures 4.15 and 4.16 show the calibration curves of the temperature and pressure multiplexed sensor respectively. These results show that the Bragg wavelength shift increased with an increase in temperature and decreased with an increase in pressure. Furthermore, these results show good linearity, high sensitivity and good degree of fitting. The temperature sensitivity coefficient was found to be 18 /℃ . The pressure sensitivity was found to be 12 pm/MPa, which is about four times the value of 3.04 pm/MPa reported in [22].

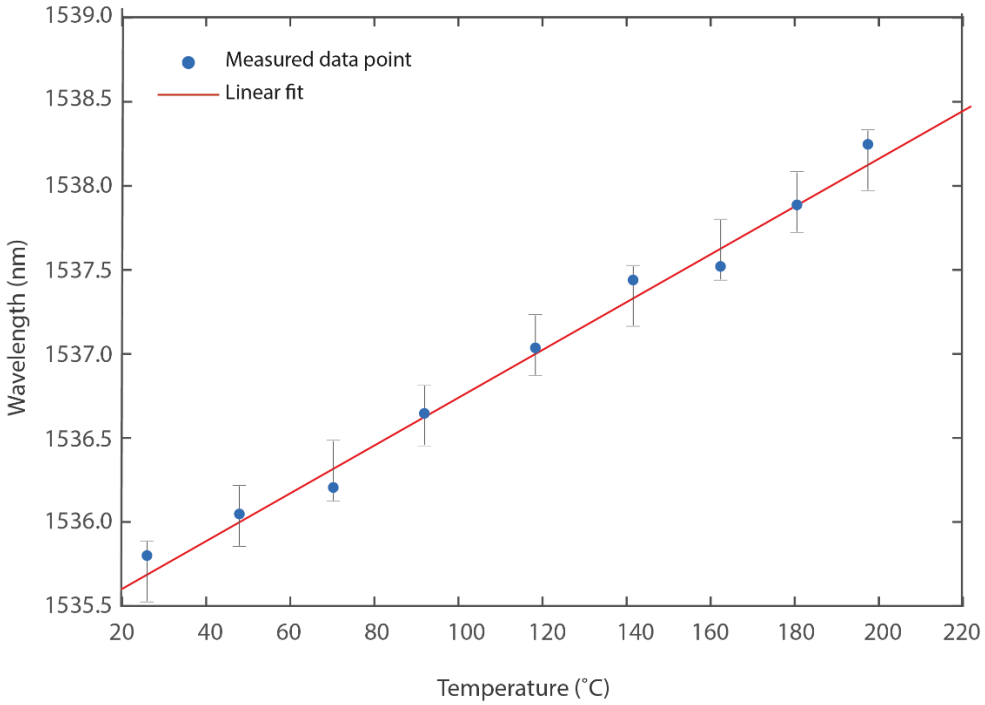

Figure 4.15 Bragg wavelength shift as a result of temperature variation

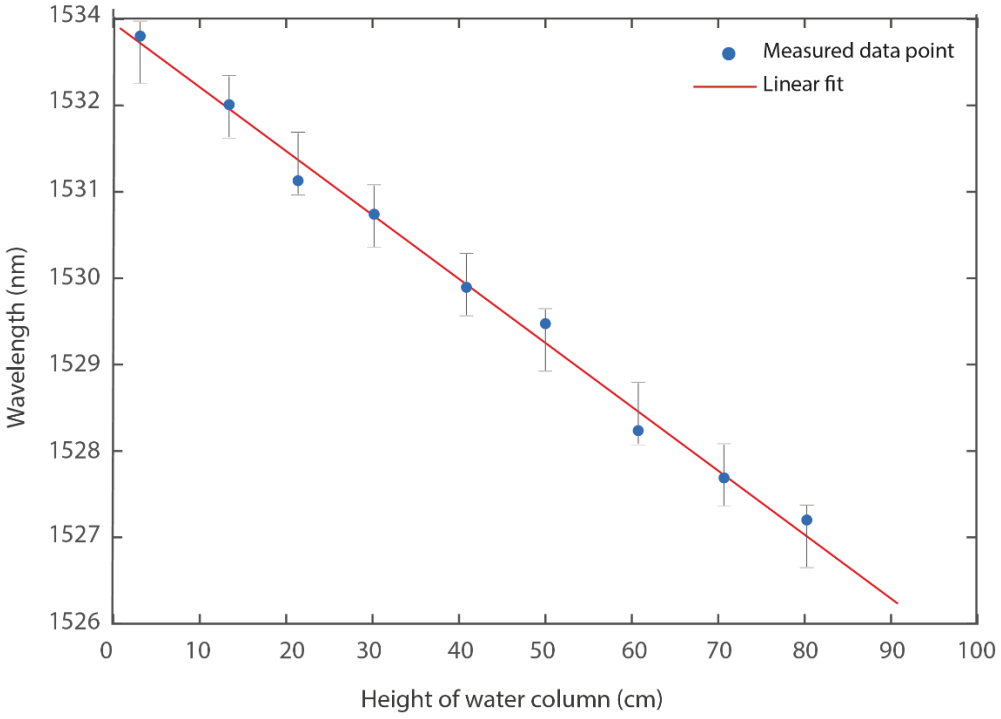

Figure 4.16 Bragg wavelength shift as a result of pressure variation

4.7 Summary

In this chapter, the design and development of a multiplexed FBG/EFPI sensor head for simultaneous measurement of temperature and pressure in permanent downhole monitoring of oil and gas wells was presented. The theoretical characteristics of a circular diaphragm when subject to external pressure is were analysed and studied.

A demultiplexing mathematical model for the FBG/EFPI multiplexed sensor for temperature and pressure measurements respectively is proposed. Preliminary results investigating the effect of pressure and temperature on the Bragg wavelength shows good linearity, high sensitivity and good degree of fitting thereby making the sensor suitable for downhole monitoring of oil and gas wells. The sensor system design combines the advantages of the simple structure of FBG for temperature measurement and high accuracy low temperature-pressure cross-sensitivity of the EFPI pressure sensor. This configuration is used to eliminate the issue of temperature-pressure cross-sensitivity and effectively improve the resolution of the sensor system. However, the major limitation to this dual sensing configuration is the fact that the glass capillary and the aluminium material used for the sensor coating have inherent fragility when the external parameters exceed beyond certain limit. Technique for protecting the fibre when exposed to HPHT environments while still have the capacity to minimise the effect of cross sensitivity of the sensor is investigated in Chapter 5.

4.8 Reference

[1] A. D. Kersey, "Optical Reservoir Instrumentation System," *Offshore Technology Conference,* vol. 2, pp. 469-472, May 1998.

[2] A. D. Kersey, A Review of Recent Developments in Fiber Optic Sensor Technology, Optical Fiber Technology, vol. 2, pp 291-317, 1996.

[3] K. T. V. Grattan and T. Sun, "Fiber optic sensor technology: an overview," *Sensors and Actuators A: Physical,* vol. 82, pp. 40-61, 2000.

[4] A. D. Kersey, "Optical Fiber Sensors for Permanent Downwell Monitoring Applications in the Oil and Gas Industry," *IEICE Trans. Electron,* vol. E83-C, pp. 400-404, 2000.

[5] J. A. Greene, T. A. Tran, K. A. Murphy, M. F. Gunther, R. G. May, and R. O. Claus, "Applications of the extrinsic Fabry-Perot interferometer," pp. 165-171, 1995.

[6] J. Dakin and B. Culshaw, *Optical Fiber Sensors: Principles and components*: Artech House, 1988.

[7] S. Webster, R. McBride, J. S. Barton, and J. D. C. Jones, "Air flow measurement by vortex shedding from multimode and monomode optical fibres," *Measurement Science and Technology,* vol. 3, p. 210, 1992.

[8] W. J. Bock, W. Urbanczyk, J. Wojcik, and M. Beaulieu, "White-light interferometric fiber-optic pressure sensor," in *Instrumentation and Measurement Technology Conference, IMTC Conference Proceedings. 10th Anniversary. Advanced Technologies in I & M., IEEE*, pp. 406-411 vol.1, 1994.

[9] K. O. Hill and G. Meltz, "Fiber Bragg grating technology fundamentals and overview," *Journal of Lightwave Technology,* vol. 15, pp. 1263-1276, 1997.

[10] S. J. Mihailov, "Fiber Bragg Grating Sensors for Harsh Environments," *Sensors,* vol. 12, pp. 1898-1918, 2012.

[11] A. D. Kersey, M. A. Davis, T. A. Berkoff, D. G. Bellemore, K. P. Koo, and R. T. Jones, "Progress toward the development of practical fiber Bragg grating instrumentation systems," pp. 40-63, 1996.

[12] A. Kersey, M. A. Davis, H. J. Patrick, M. Leblanc, K. P. Koo, C. G. Askins, M. A. Putnam, and E. J. Friebele, "Fiber grating sensors," *Lightwave Technology, Journal of,* vol. 15, pp. 1442-1463, 1997.

[13] M. G. Xu, J. L. Archambault, L. Reekie, and J. P. Dakin, "Discrimination between strain and temperature effects using dual-wavelength fibre grating sensors," *Electronics Letters,* vol. 30, pp. 1085-1087, 1994.

[14] M. Vaughan, *The Fabry-Perot Interferometer: History, Theory, Practice and Applications*: Taylor & Francis, 1989.

[15] Z. Yizheng and W. Anbo, "Miniature fiber-optic pressure sensor," *Photonics Technology Letters, IEEE,* vol. 17, pp. 447-449, 2005.

[16] Z. Yizheng and W. Anbo, "Miniature fiber-optic pressure sensor," *IEEE Photonics Technology Letters,* vol. 17, pp. 447-449, 2005.

[17] D. Giovanni, *Flat and Corrugated Diaphragm Design Handbook*: Taylor & Francis, 1982.

[18] X. Juncheng, G. Pickrell, W. Xingwei, P. Wei, K. Cooper, and W. Anbo, "A novel temperature-insensitive optical fiber pressure sensor for harsh environments," *Photonics Technology Letters, IEEE,* vol. 17, pp. 870-872, 2005.

[19] M. Han, "Theoretical and Experimental Study of Low-Finesse Extrinsic Fabry-Perot Interferometric Fiber Optic Sensors," PhD PhD, Electrical and Computer Engineering. , Virginia Tech. USA, 2006.

[20] X. Hai, D. Jiangdong, G. Pickrell, R. G. May, and W. Anbo, "Single-crystal sapphire fiber-based strain sensor for high-temperature applications," *Lightwave Technology, Journal of,* vol. 21, pp. 2276-2283, 2003.

[21] S. A. Egorov, A. N. Mamaev, I. G. Likhachiev, Y. A. Ershov, A. S. Voloshin, and E. Nir, "Advanced signal processing method for interferometric fiber optic sensors with straightforward spectral detection," pp. 44-48, 1998.

[22] M. G. Xu, L. Reekie, Y. T. Chow, and J. P. Dakin. (Optical in-fibre grating high pressure sensor. *Electronics Letters 29(4),* 398-399, 1993.

Chapter 5

5 Design and analysis of a sensing system for high pressure and temperature measurement

5.1 Introduction

In this chapter, the technique for protecting the optical fibre sensor when exposed to HPHT environments while still having the capacity to minimise the cross sensitivity effect of the sensor is investigated. The optical fibre mainly composed of germanium silicate is so fragile that it tends to fail or suffer damage when used in HPHT environments due to the high non-uniform stress, strain or thermal loads. In particular, a protective metal layer is necessary to overcome the problems. The technique for chemical plating and electroplating of nickel are both well-documented, however, application of these techniques for acquiring high-quality metal-coatings of desired thickness on optical fibre with in-fibre Bragg grating requires future research. It is necessary to study the characterization of the metal coat as well as the behaviour of the sensor under thermal loads. It is found that FBG with different metal coating thickness have different temperature sensitivities.

The theoretical design and analysis of a metal coated hybrid sensing system of FBG and EFPI cavity for HPHT measurement in harsh environments is presented. The FBG and EFPI are used to measure temperature and pressure respectively. An opto-mechanical model that assesses the measurement of HPHT for downhole applications with hybrid sensing system was developed.

In this model, the effect of metal coating on a sensor is studied. The model combines both optical and structural analysis for developing an optimal sensor system design. The optical analysis is carried out to obtain the spectral response of the sensor while the structural analysis is used to obtain the change in optical properties of the sensor due to photo-elastic effect. Analytical results showed that the temperature sensitivity of the hybrid sensor with double layer metal coated FBG increased to $23.89\,pm/°C$ when compared with single metal coated FBG of $13.95\,pm/°C$ from previous study and the associated pressure range to be measured up to $5000\,kPa$. Furthermore, the proposed sensor design has shown good linearity. While the single coated FBG sensor shows little sensitivity, the sensitivity increases with the metal coating of the sensor.

The effect of temperature on FBG is due to two factors: (i) the dependence of the refractive index of the glass to temperature and (ii) the thermal expansion of the of the glass. In silica fibres, approximately 95% of the observed shift in the Bragg wavelength occurs due to the shift in the refractive index of the fibre with respect to temperature changes. A bare FBG temperature sensor with a wavelength of $1.3\ \mu m$ over the range of 5 ℃ to 85 ℃ gives a normalized responsivity of 6.67×10^{-6} ℃$^{-1}$[1]. A typical value for thermal response at $1550\ nm$ is $0.01\ nm$/℃. At higher temperature the sensitivity is higher and the response becomes slightly nonlinear [2]. An FBG is essentially not very sensitive to the change of the external refractive index [3]. By attaching the FBG to passive devices, the thermal characteristics of the materials can be used to control the sensitivity of the FBG wavelength to temperature.

An hybrid FBG/EFPI sensor based on single metal layer coating has been reported [4-6]. However, the single coated sensors suffer significantly from low sensitivity when use in elevated HPHT environments in the oil and gas industry. The sensitivity requirement of FBG sensors in oil and gas applications is very important and is usually of high magnitude.

Several techniques of metallic coating on FBG have been studied [7-9]. Some metallic coatings applied to optical fibre using techniques such as electrodeless plating, physical vapour deposition (PVD), and thermal spraying are silver, aluminium, copper, nickel, gold, titanium and lead. The electrodeless plating is the most commonly use method of coating because of its simplicity and low cost. Li *et al* [9] used lead cladding to enhance temperature sensitivity of FBG sensor. He found out that metal with a high thermal expansion coefficient produces better sensitivity performance (five times more) than the bare fibre. Silicon piezo-resistive and capacitive based pressure sensors have been reported and developed [10-12]. However, silicon based pressure sensors have suffered serious mechanical performance degradations when used in harsh environment. For temperature sensors, enhancing temperature sensitivity is one of the key technologies. There have been many efforts for the exploration of the thermal performance of metal-coated FBG. Zhan et al. [13] studied the temperature characteristics of FBG encapsulated by aluminum groove. Shiue et al. [14] and Xieet al. [15] studied the thermal sensitivity of nickel-coated FBGs with different thickness. Zhang et al. [16] enhanced the temperature sensitivity using a wavelength shift detection system based on matching FBG. Rajini-Kumar et al. [17] reported that indium-recoated FBG sensors showed a higher sensitivity at around $15\,K$ compared with Al, Cu, and Pb-coated FBG sensors. In general, metal coating with large thermal expansion coefficient can

enhance the temperature sensitivity of FBG. One of the key causes of stress in a body is non uniform expansion or contraction as temperature fluctuates. For a double metal-coated FBG sensor, each layer tends to expand or contract when temperature fluctuates. However, such expansion or contraction generally cannot proceed freely due to the different thermal expansion coefficients and the boundary limits. Thermal stresses are set up due to the restriction in such thermal deformation, they have significant effects on the temperature sensitivity of FBG. When the coated fibre is subject to high temperature, there is an increase in the thermal expansion coefficients of the coating metals. This in turns creates axial and radial stresses on the fibre which cause the FBG sensitivity to increase.

The metal coating also protects the FBG. Lupi *et al*. [18] coated the FBG with zinc and copper using the traditional electroextraction or electrodeposition process, after an aluminum pre-coating of the sensor. However, if an abrupt thermal stress (occurring at much lower temperature) occurs during the coating process, this can permanently affect the optical features of the FBG and the optical properties will also be slightly affected by the coating process. Tian [19] and Song [20] bonded FBGs to the lower CTE side of a bimetal and used it as a sensor to measure temperature and strain. Work on the preliminary investigation of temperature and pressure measurement system for downhole monitoring of oil wells using FBG/EFPI sensing had previously been discussed to overcome the issue of temperature and pressure cross sensitivity in Chapter 4 [21]. A de-multiplexing mathematical model was also proposed for separating the FBG spectrum from the EFPI. The FBG/EFPI sensor is a diaphragm based sensor with the referenced FBG to eliminate the effect of temperature cross sensitivity. However, with the many advantages of

this sensor type, it suffers low sensitivity when used in elevated temperature environments.

To overcome these limitations, this chapter proposes an analytical model of metal coated hybrid sensing system of FBG and EFPI cavity for HPHT measurement in downhole monitoring applications. These sensors are made using two dissimilar metals and the sensors are spectrally encoded. Theoretical analysis was carried out to obtain the spectral response of the hybrid sensor and the structural analysis is used to obtain the change in optical properties of the sensor due to photo-elastic effect. Copper and nickel were chosen as the coating materials for this work. While copper was selected as the outer protective layer due to its large thermal expansion coefficient and good extension, nickel was chosen as the conductive layer for its high melting point, non-susceptible to corrosion and oxidation, good conductivity and also large thermal expansion coefficient [22]. Silicon carbide (SiC) is the choice material for the EFPI diaphragm owing to its chemical inactiveness and mechanical robustness when used in harsh environment. The operating temperature of EFPI pressure based sensor is limited by the choice of the diaphragm being used. Here we propose a hybrid FBG/EFPI sensor with the FBG coated with outer protective layer of copper and inner layer of nickel. The EFPI has a SiC diaphragm.

Copper was used as the outer coat metal because of it physical property such as high thermal expansion, high ductility, good tensile strength, ability to withstand corrosion when used in harsh environment, strong resistance to creep (deformation) and has melting and boiling points of 1083.4 +/- 0.2 °C

and 2567 °C respectively. The Young's modulus of Cu is between $110 - 128\ GPa$ and the Poisson ratio is 0.34.

5.2 Analytical Model

The schematic of the wavelength encoded hybrid sensor is shown in Figure 5.1. The sensing head is made up of FBG and EFPI sensors connected in series for HPHT measurements. The FBG is sensitive to temperature as a result of the thermo-optic effect and thermal expansion of the fibre material while the EFPI is used to measure high pressure. A convoluted combined signal is derived from the configuration but first, each individual signal was first analysed and modelled.

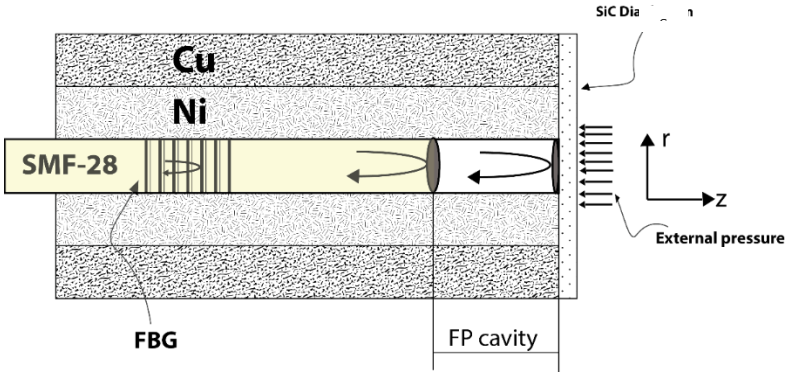

Figure 5.1 Schematic Representation of the proposed FBG/EFPI Hybrid Sensing Head

To analyse the effect of the metal coating on the sensitivity of the hybrid sensor and obtain the optimum thickness of the coated metal, an opto-mechanical model was developed. This model is based on the photo-elastic and thermo-optic properties of the fibres.

5.2.1 FBG sensor opto-mechanical model and response

The FBG sensor is wavelength encoded and the wavelength varies with the period of the grating. The FBG is produced by radiating the optical fibre with intense ultra-violet beams originated from the same laser source. The beams which are coherent, constructively and destructively interfere. The standard germanium doped FBG was used with wavelength of $1550\,nm$, the pressure sensitivity and temperature sensitivity are $-3\,pm/MPa$ and $13\,pm/℃$ [23,24] respectively.

The opto-mechanical model of the FBG sensor predicts the shift in Bragg wavelength with respect to temperature and pressure functions at various thickness of the coated metals. To study the temperature sensitivity of a metal coated FBG, first the analysis of a coated FBG subject to the effect of strain by temperature changes is carried out.

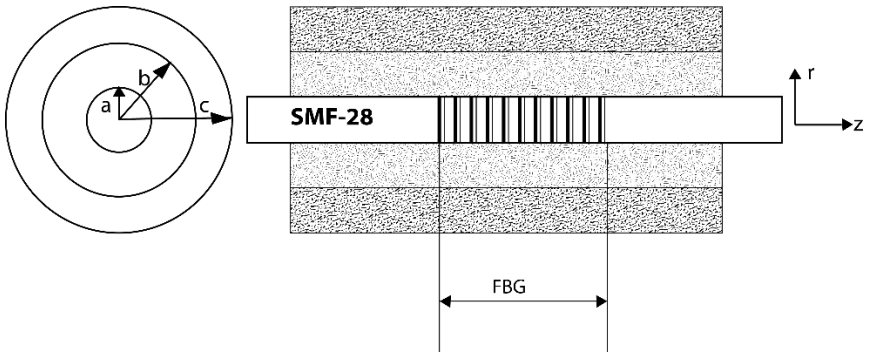

Figure 5.2 Sensing Schematic of an FBG System

Figure 5.2 shows the schematic of the coordinate system of an FBG sensor with both the axial and radial directions. The components of this system subject to both temperature and pressure are analysed analytically using MATLAB. To measure temperature change ΔT, the wavelength shift $\Delta\lambda_B$ when exposed to thermal strain variation is given by [3]

$$\Delta\lambda_B = \lambda_B(\alpha + \xi)\Delta T + \lambda_B\left\{\varepsilon_z - \frac{n_{eff}^2}{2}[\nu(p_{11} + p_{12})\varepsilon_r + p_{12}\varepsilon_z]\right\} \quad (5.1)$$

where λ_B is the Bragg wavelength, n_{eff} is the effective refractive index of the fibre, p_{11} and p_{12} are the components of the fibre optic strain tensor also known as the Pockels constants of the fibre determined experimentally, ε_z is the applied strain along the longitudinal axis, ε_r represent the radial thermal strain, α is the thermal expansion coefficient for the fibre, ξ is the thermo-optic coefficient and ν is the Poisson's ratio.

Also, to measure pressure change ΔP, the shift in wavelength $\Delta\lambda_B$ is given by [3]

$$\Delta\lambda_B = \left[-\frac{(1-2\nu)}{E} + \frac{n_{eff}^2}{2E}(1-2\nu)(2p_{12} + p_{11})\right]\Delta P \quad (5.2)$$

where E is the Young's Modulus of the fibre. To measure the combined effect of both temperature and pressure simultaneously, the shift in Bragg wavelength is expressed as

$$\Delta\lambda_B = \Delta T \cdot K_T + \Delta P \cdot K_P + \Delta T \cdot \Delta P \cdot K_{TP} \quad (5.3)$$

where K_T, K_P and K_{TP} are the temperature sensitivity, pressure sensitivity and cross sensitivity respectively. This model is based on some certain assumptions. The metal coatings, thermal expansion coefficient of the fibre α,

the thermo-optic coefficient ξ and the Poisson's ratio ν are all constant and independent of the thermal variations. Also we assume that there is no relative displacement between the metal coating and the FBG.

To carry out the opto-mechanical model of the FBG sensor, the infinite circular thin wall of a hollow cylinder model is employed. This is made of three-layered materials with the first material representing the copper coating, the second material representing nickel coating and the third representing FBG. The cylinder is considered to be an isotropic linear elastic composite material with free ends. Lame's formula and strain-stress relationship is use in this model [25]. The parameters for the model are α_i for thermal expansion coefficient, E_i for Young's modulus, v_i for the Poisson ratio and r_i for radius of the fibre (i = 1, 2, 3 for the FBG, nickel and copper coating respectively).

The axial and radial characteristics of the metal coating are studied and analysed. For the axial stress, let Δl_1, Δl_2, Δl_3 be the free axial elongations of the FBG, Ni coating, Cu coating respectively and the change in temperature be ΔT. These can be expressed as follows:

$$\Delta l_1 = \alpha_1 \Delta T L$$

$$\Delta l_2 = \alpha_2 \Delta T L$$

$$\Delta l_3 = \alpha_3 \Delta T L$$

Since no relative displacement exists between the metal coating and the FBG, the elongation of the FBG, nickel coating and copper coating are expressed as:

$$\alpha_1 \Delta T L + \varepsilon_{1z} L$$

$$\alpha_2 \Delta T L - \varepsilon_{2z} L$$

$$\alpha_3 \Delta T L + \varepsilon_{3z} L$$

The boundary condition is defined as

$$\sigma_{1z} A_1 + \sigma_{2z} A_2 = \sigma_{3z} A_3$$

where A_i is the cross section of the layer i. Bringing all together and applying Hooke's theorem [25], the strain of the FBG as a result of the axial thermal stress is given by

$$\varepsilon_{1r} = v_1 K_1 \Delta T$$

where K_1 is the thermal axial coefficient given by [25]

$$K_1 = \frac{(\alpha_3 - \alpha_1) E_3 (r_3^2 - r_2^2) + (\alpha_2 - \alpha_1) E_2 (r_2^2 - r_1^2)}{E_1 r_1^2 + E_2 (r_2^2 - r_1^2) + E_3 (r_3^2 - r_2^2)} \quad (5.4)$$

For radial stress model, let $\Delta\delta r_1$, $\Delta\delta r_2$, $\Delta\delta r_3$ be the free radial elongations of the FBG, nickel coating, copper coating respectively and the change in temperature be ΔT. These can be expressed as follows:

$$\Delta\delta r_1 = \alpha_1 r_1 \Delta T$$

$$\Delta\delta r_2 = \alpha_2 r_2 \Delta T$$

$$\Delta\delta r_3 = \alpha_3 r_3 \Delta T$$

The nickel coating is viewed as a hollow cylinder with inner and outer radii as a and b subjected to uniform pressures p_1 and p_2 on the surfaces respectively. The radial stress can be derived based on Lame solutions as [26]:

$$\delta r_2 = \frac{p_1 a^2(r_2^2 - b^2) + p_2 b^2(a^2 - r_2^2)}{r_2^2(b^2 - a^2)} \tag{5.5}$$

and the radial displacement is expressed as [26]

$$u_{2r} = \frac{1}{E_2}\left\{\frac{(1-v_2)(a^2 p_1 - b^2 p_2}{b^2 - a^2} - \frac{(1+v_2)a^2 b^2(p_1 - p_2)}{(b^2 - a^2)r_2}\right\} \tag{5.6}$$

and the radii final elongations are expressed as [26]

$$\Delta r_{2a} = \alpha_2 a \Delta T + \left\{\frac{p_1 a[(1-v_2)a^2 + (1+v_2)b^2] - 2p_2 a b^2}{E_2(b^2 - a^2)}\right\} \tag{5.7}$$

$$\Delta r_{2b} = \alpha_2 a \Delta T + \left\{\frac{2p_1 a b^2 - p_2 a[(1-v_2)b^2 + (1+v_2)a^2]}{E_2(b^2 - a^2)}\right\} \tag{5.8}$$

The copper coating is also viewed as a hollow cylinder with inner and outer radii as b and c which is only subjected to uniform internal pressure p_2 The outer surface is not considered in this model. The inner radius of the nickel coating final elongation is expressed as:

$$\Delta r_{3b} = \alpha_3 b \Delta T + \left\{ \frac{p_2 b[(1+v_3)c^2 + (1-v_3)b^2]}{E_3(c^2 - b^2)} \right\} \quad (5.9)$$

For the FBG sensor, the final elongation is expressed as

$$\Delta r_{1a} = \alpha_1 a \Delta T + (1 - v_2)\frac{p_1 a}{E_1}$$

Applying the boundary conditions,

$$\Delta r_{1a} = \Delta r_{2a}$$

$$\Delta r_{2a} = \Delta r_{3a}$$

Combining equations 5.7 – 5.9 the following equations can be obtained to determine the values of p_1 and p_1

$$M_3 \Delta T = M_1 p_1 + M_2 p_2$$

$$M_6 \Delta T = M_4 p_1 + M_5 p_2$$

p_1 and p_1 can then be obtained as:

$$p_1 = \left\{ \frac{M_2 M_6 - M_3 M_5}{M_2 M_4 - M_1 M_5} \right\} \Delta T$$

$$p_1 = \left\{ \frac{M_3 (M_2 M_4 - M_1 M_5) - M_1 (M_2 M_6 - M_3 M_5)}{M_2 (M_2 M_4 - M_1 M_5)} \right\} \Delta T \quad (5.10)$$

For FBG in the metal coated model, it is worth noting that the radial strain of the FBG as a result of the radial thermal stress, and the axial strain as a result of the axial thermal stress can are expressed as:

$$\varepsilon_{1r} = (1 - v_1)\frac{p_1}{E_1}$$

$$\varepsilon_{1z} = -2v_1\frac{p_1}{E_1} \tag{5.11}$$

substituting equation 5.10 into 5.11 and the radial and axial strains can be expressed as:

$$\varepsilon_{1r} = \frac{1 - v_1}{E_1}K_2\Delta T$$

$$\varepsilon_{1z} = \frac{-2v_1}{E_1}K_2\Delta T$$

where K_2 is known as the radial thermal stress coefficient expressed as:

$$K_2 = \frac{M_2 M_6 + M_3 M_5}{M_2 M_4 + M_1 M_5} \tag{5.12}$$

where the respective expressions for M_i are shown in the table below

Table 5.1 Expressions for M_i

M_i	Expressions
M_1	$E_2(b^2 - a^2)(1 - v_1) - E_1a^2(1 - v_2) - E_1b^2(1 + v_1)$
M_2	$2E_1b^2$

M_3	$E_1E_2(b^2 - a^2)(\alpha_2 - \alpha_1)$
M_4	$2E_3(c^2 - b^2)a^2$
M_5	$E_2(b^2 - a^2)(1-v_3)b^2 + E_2(b^2 + a^2)(1+v_3)c^2 - E_3(c^2 - b^2)(1+v_2)a^2 - E_3(c^2 - b^2)(1-v_2)b^2$
M_6	$E_2E_3(b^2 - a^2)(c^2 - b^2)(\alpha_2 - \alpha_3)$

The final strains ε_r and ε_z of the coated FBG are the combination of both the radial and the axial thermal stresses and it is expressed as:

$$\varepsilon_r = \left(\frac{1-v_1}{E_1}K_2 - v_1K_1\right)\Delta T$$

$$\varepsilon_z = \left(K_1 - \frac{2v_1}{E_1}K_2\right)\Delta T$$

substituting these into the equation 5.1 the wavelength shift $\Delta\lambda_B$ when exposed to thermal strain variation;

$$\Delta\lambda_B = \lambda_B\left\{(\alpha + \xi) + (1 + p_{12})\left(K_1 - \frac{2v_1}{E_1}K_2\right) + \frac{n_{eff}^2}{2}(p_{11} + p_{12})\left(\frac{1-v_1}{E_1}K_2 - v_1K_1\right)\right\}\Delta T \quad (5.13)$$

$$\Delta\lambda_B = K_{mT}\lambda_B\Delta T \quad (5.14)$$

$$S_T = \alpha + \xi$$

$$S_z = (1 + p_{12})\left(K_1 - \frac{2v_1}{E_1}K_2\right)$$

$$S_r = -\frac{n_{eff}^2}{2}(p_{11} + p_{12})\left(\frac{1 - v_1}{E_1}K_2 - v_1K_1\right)$$

Where K_{mT} is the sensitivity coefficient of the coated materials and optical fibre, S_T is the temperature sensitivity coefficient of the bare FBG whose constants are determined by the fibre material, S_z is the axial thermal strain sensitivity coefficient and S_r is the radial thermal strain sensitivity coefficients. The parameters M_1, M_2 M_3, M_4, and M_5 are affected by the properties of the FBG material.

5.3 The Effect of Metal Coated FBG on Temperature Sensitivity

To properly investigate the effect of the metal coating properties on the sensitivity of FBG, the variation of temperature sensitivity and the material properties were first studied using the double layered opto-mechanical model shown in equation 5.14. In this design, a $Cu - Ni$ coated FBG with diameter $62.5\,nm$ was used.

The parameters used for the simulation are listed as follow [26]; the FBG parameters are $E_1 = 74\,GPa$, $\alpha_1 = 0.55 \times 10^{-6}/℃$, $\xi = 6.3 \times 10^{-6}/℃$, $p_{11} = 0.121$, $p_{12} = 0.27$, $n_{eff} = 1.456$, $v_1 = 0.17$, and $a = 62.5\,\mu m$ [26]

The parameters for nickel coating are $E_2 = 220\,GPa$, $\alpha_2 = 14.2 \times 10^{-6}/℃$, and $v_1 = 0.31$. The parameters for copper coating are $E_3 = 120G\,Pa$, $\alpha_3 = 17.2 \times 10^{-6}/℃$, and $v_1 = 0.32$.

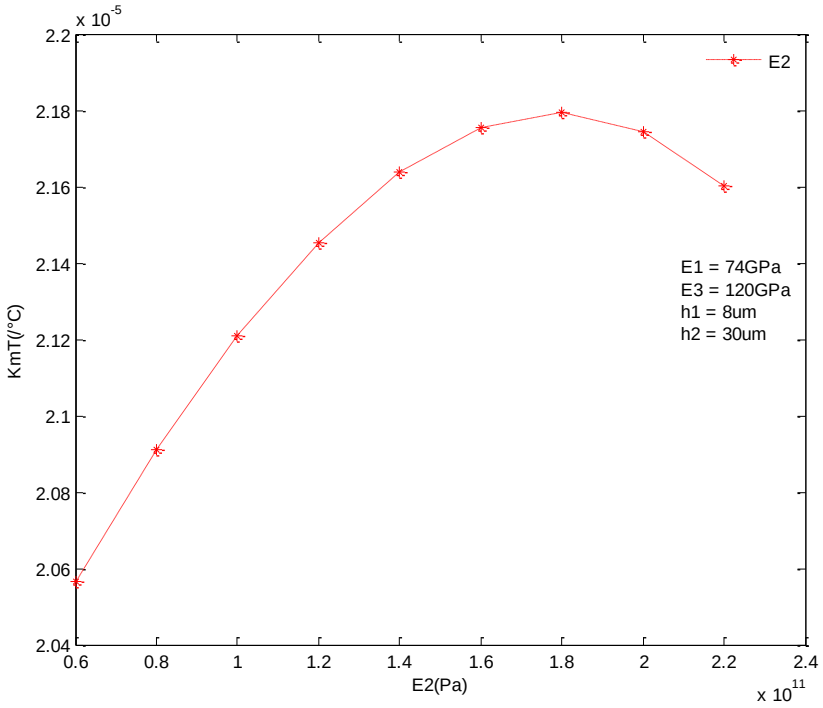

Figure 5.4. Effect of elastic modulus E_2 on temperature sensitivity K_{mT}

Figure 5.4 presents the effect of the nickel metal coating property E_2 on temperature sensitivity of the metal coated FBG. As depicted in the figure, the temperature sensitivity at first has a linear trend but has the tendency to decline with increase in elastic modulus. The temperature sensitivity varies from $20.57\,pm/℃$ to $21.79\,pm/℃$ at $E_2 = 180\,GPa$ before starting to decline as E_2 increases. This response is as a result of the linear structural properties of the metal coat and the linear characterisation of FBG.

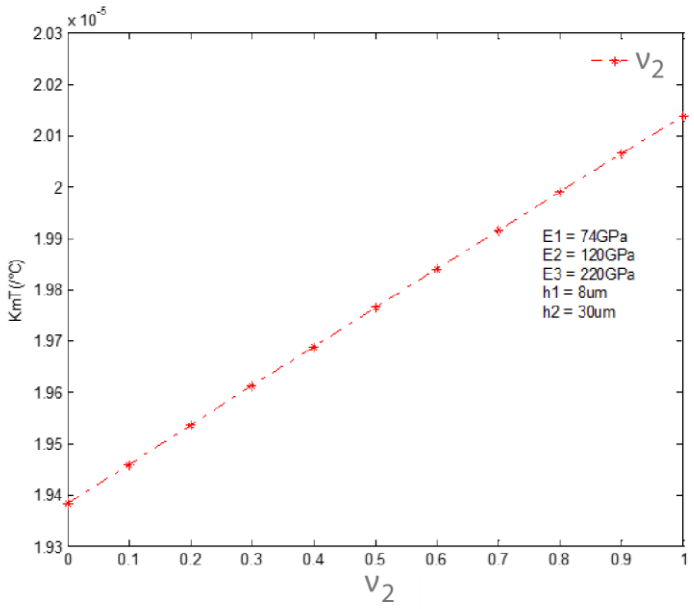

Figure 5.5 Effect of Poisson's ratio v_2 with respect to temperature sensitivity K_{mT}

Figure 5.5 shows that if other given factors remain constant, Poisson's ratio has a linear relationship with respect to temperature sensitivity within a certain range. It shows that temperature sensitivity has a linear relationship with Poisson's ratio. Also, Figure 5.6 depicts the effect of thermal expansion coefficient with temperature sensitivity. Within a certain range, the temperature sensitivity increases with increase in coefficient of thermal expansion which shows a linear relationship. It is important to note that the material properties discussed above are interrelated. For example, the elastic modulus and the Poisson's ratio are dependent on each other. If the elastic modulus increases, the Poisson's ratio decreases. Therefore, in a practical scenerio, these properties cannot be separated from each other when studying the effects on the sensitivity of metallic coated FBG.

The parameters for the $Cu - Ni$ coated FBG are shown in Figures 5.4 and 5.5 above. The thickness of Ni is represented as *h2* while that of Cu is *h1*.

According to Figure 5.7, the $Cu - Ni$ coated FBG shows the relationship between temperature sensitivity with change in *h1* and *h2*. It can be seen that when the coating thickness *h2* is between 0 and $90\,\mu m$, the temperature sensitivity increases to $22.5 \times 10^{-6}/°C$ and then rises slowly to $23.6 \times 10^{-6}/°C$ before it reaches steady state at $23.89 \times 10^{-6}/°C$ with the increase of $h2$. This when compared with a single metal coated FBG that has a temperature sensitivity of $13.9 \times 10^{-6}/°C$ as reported by [23,24] , the temperature sensitivity is higher for the same value of $h1$. The result shows that the double metal layer coated FBG enhances temperature sensitivity more than a single layer coated FBG. The theoretical analysis shows that the temperature sensitivity of FBG changes with the variation of metal coating thickness.

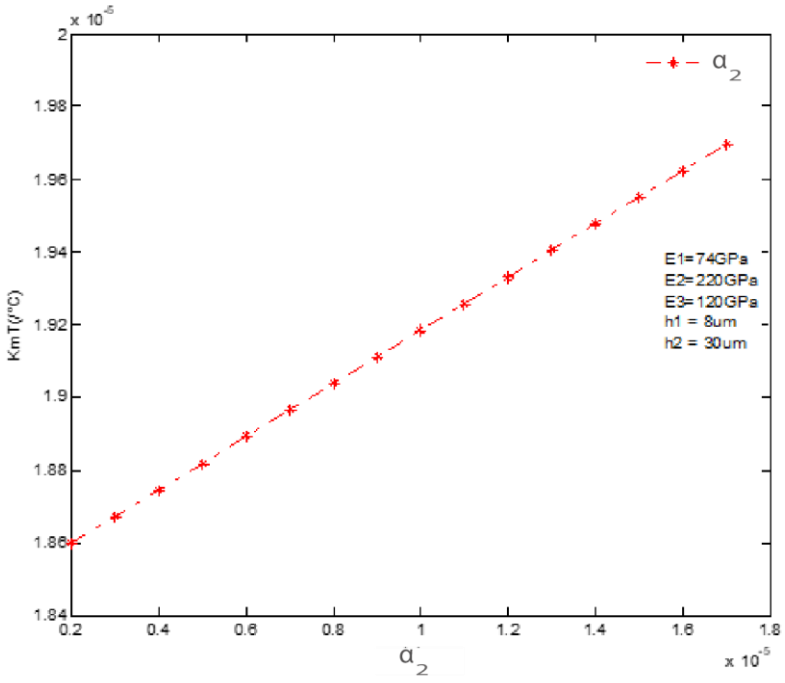

Figure 5.6 Effect of thermal expansion coefficient α_2 on temperature sensitivity K_{mT}

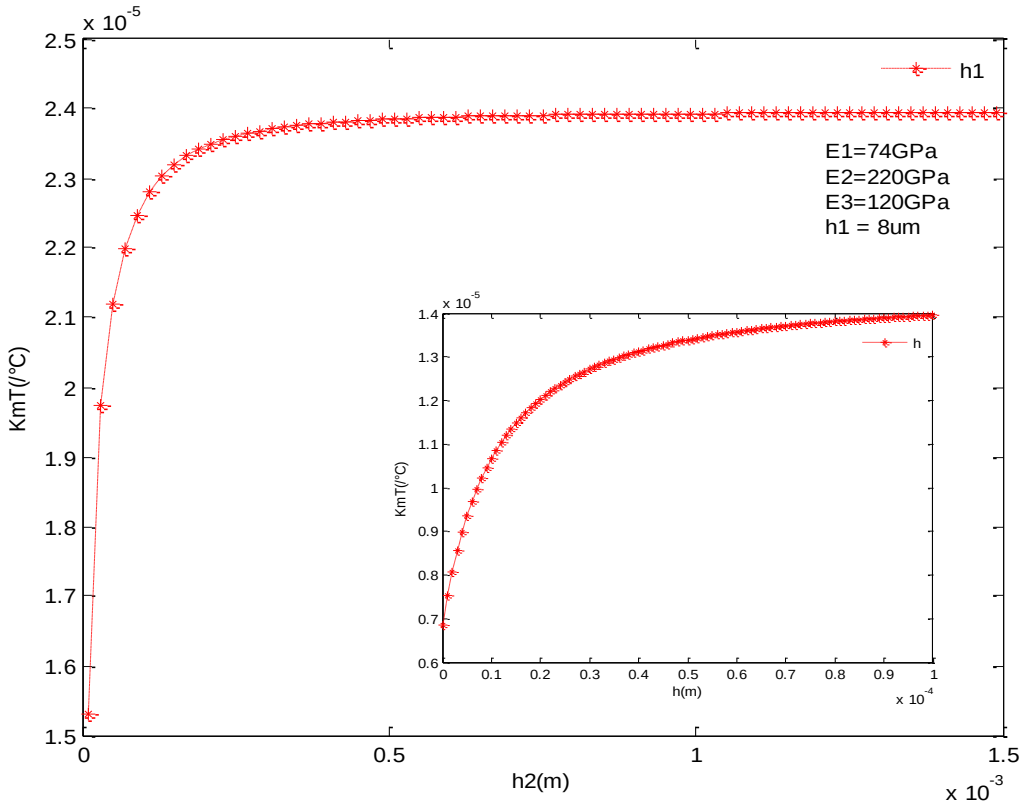

Figure 5.7 The Effect of Metal Coated FBG on Temperature Sensitivity, the inset shows the sensitivity on a single metal coating.

With the same temperature range, the coefficient of thermal expansion of Cu is larger than the coefficient of Ni. The change in wavelength of FBG have been theoretically analysed and simulated with both Δl_1 (the free axial elongation of Ni) and Δl_2 (the free axial elongation of Cu) to be $8\,mm$, $10\,mm$ and $10\,mm$, $8\,mm$ in the range of $0-500\,℃$. The result are shown in Figure 5.8. From the graph, it can be seen that the shift in peak wavelength almost has a linear relationship with temperature in the range of $0-500\,℃$ having a shift in wavelength of $6.65\,nm$. The sensitivity of the sensor is enhanced with Cu having higher coefficient of thermal expansion and longer axial elongation than Ni with

small coefficient of thermal expansion. This can be confirmed in Figure 5.7 showing the slope of curve (a) higher than that of curve (b).

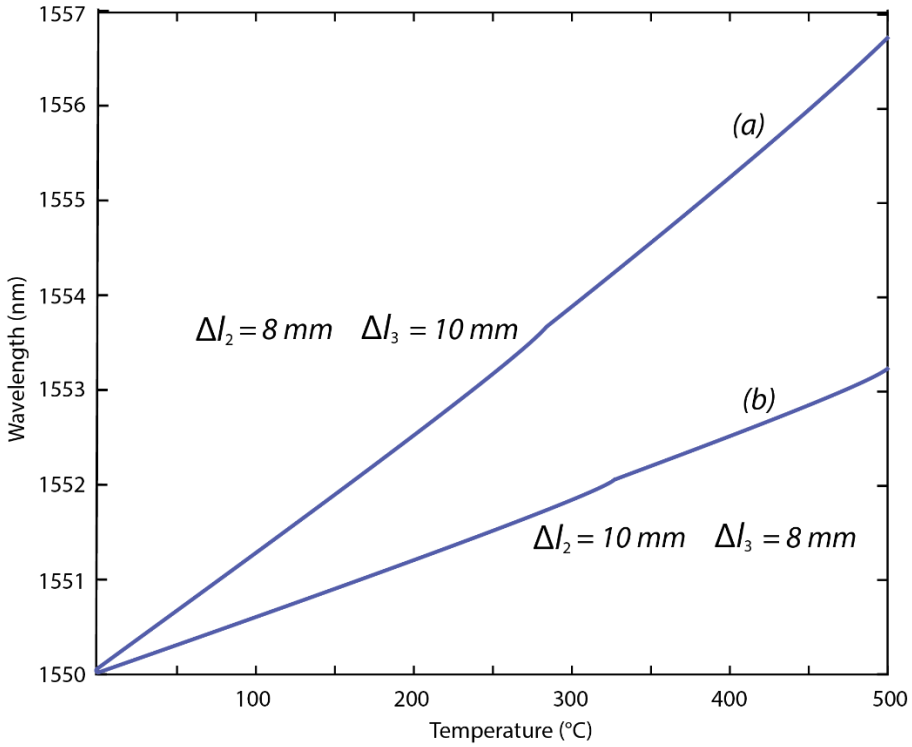

Figure 5.8 Change in wavelength of metal coated FBG with temperature and free axial elongation.

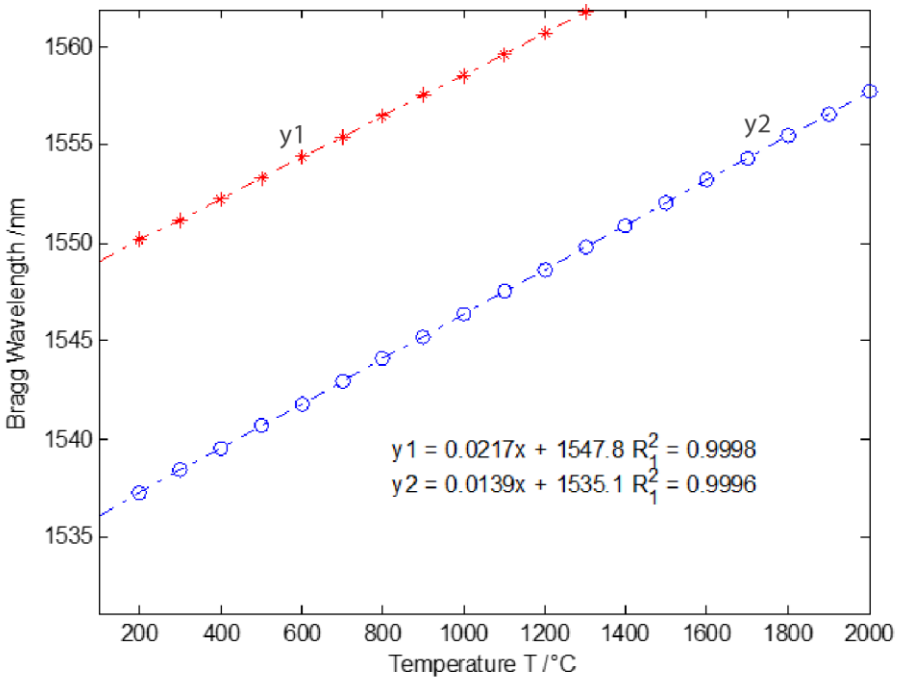

Figure 5.9 Bragg wavelength shift as a function of temperature for double and single coated FBG

Figure 5.9 shows the simulated response of a double metal coated $Cu - Ni$ FBG sensor temperature sensitivity with single coated FBG, temperature value used for the model ranges from $100 - 2000\,°C$. The simulation was done for different wavelength shifts and temperature variations to ensure repeatability and reliability.

Results show Bragg wavelength peaks increase linearly with various coating thickneses. The double coated metal FBG peak wavelength increases linearly with a temperature sensitivity of $21.7 \times 10^{-6}/°C$ while that of single coated metal is $13.9 \times 10^{-6}/°C$. The result also shown that the Bragg wavelength shifted down by almost $12.7\,nm$. This shows that different variation of metal coated FBG thickness can be attributed to the change in temperature sensitivity

and increase in the coated FBG thickness increases the the temperature sensitivity of FBG.

5.4 EFPI Sensor Model and Response

The schematic diagram of the EFPI sensor is shown in Figure 5.10. The EFPI is formed at the end face of the fibre and the SiC diaphragm. The SiC diaphragm deflects under any kind of stress which provides the pressure sensing signal. The optical path distance known as the cavity length between the endface of the fibre and the diaphragm will change as a result of the lateral and longitudinal compressions of both the coating metals and the diaphragm. When the metal coated sensor head is subjected to an applied pressure, the longitudinal air-gap distance ΔL of the EFPI will change as a result. The relationship between the applied pressure ΔP and the cavity length ΔL of the hybrid sensor assuming the lead-in fibre and the reflecting diaphragm is expressed as [26];

$$\Delta L = \frac{3(1-v^2)r^4}{16Eh^3}\Delta P \tag{5.15}$$

where r is the radius of the SiC diaphragm defined by the inner diameter of Cu coat metal, h is the thickness of the diaphragm, E is Young's Modulus and v is Poisson's ratio of the diaphragm. This model describes the deflection of a circular diaphragm when subjected to uniform distributed applied pressure. The diaphragm pressure sensitivity (Y) is define as the ratio of the deflection and the pressure difference.

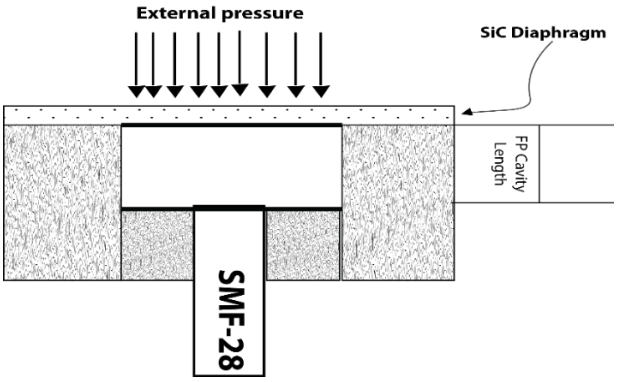

Figure 5.10 Schematic of the structure of EFPI Pressure Sensor depicting a rigidly clamped SiC diaphragm when subject to a uniform distributed pressure

Table 5.2 Material properties of SiC [26]

Density	ρ	3100	$kg\ m^{-3}$
Young's modulus	E	410	GPa
Poisson's ratio	v	0.14	
Tensile stress	σ_m	3900	Pa

The material properties of SiC used for the design and simulation are shown in Table 5.2. The simulated results of the SiC diaphragm deflection when subjected to uniformly distributed pressure using the finite element method (FEM) in MATLAB is shown in Figure 5.11. The model is designed with $1\,mm$ diaphragm radius, $40\,\mu m$ thickness, $30\,\mu m$ cavity length and operates under pressure of $5000\,kPa$. Figure 5.11(a) shows the deflection with the uniformly applied pressure and Figure 5.11(b) shows the profile of pressure distribution

on the diaphragm. The deflection varies from zero at the diaphragm edge to a maximum value at the centre.

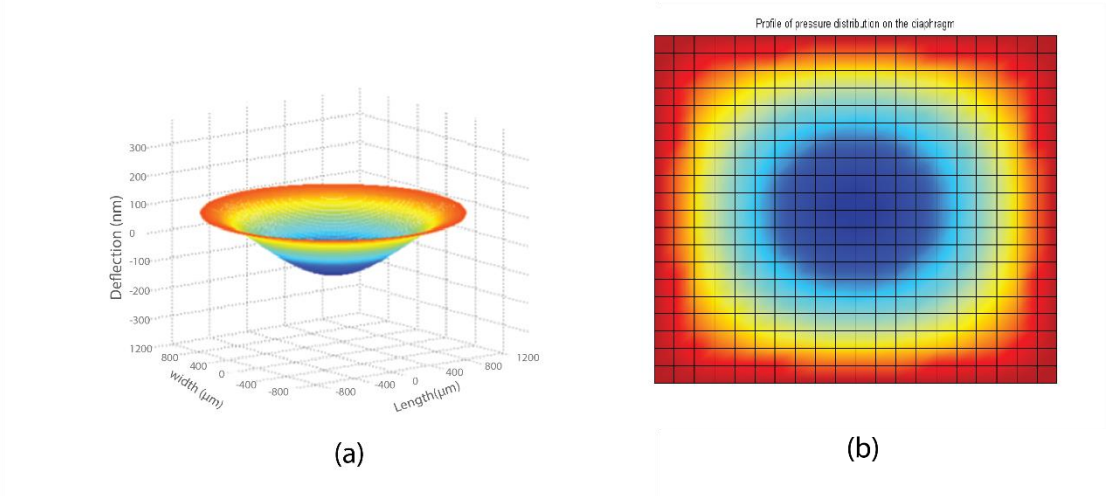

Figure 5.11 Simulated deflection of the SiC diaphragm when subject to uniform distributed pressure in MATLAB

The normal interference spectrum of the EFPI pressure sensor is shown in Figure 5.12 using the EFPI expression in section 4.2 of the previous chapter. The relationship between the pressure sensitivity and the diaphragm thickness is depicted in Figure 5.13. It shows that pressure sensitivity increases with increase in diaphragm radius and decreasing thickness. Considering the design objective of the HPHT, the diaphragm radius is taken to be $1\,mm$ and the thickness to be $40\,\mu m$.

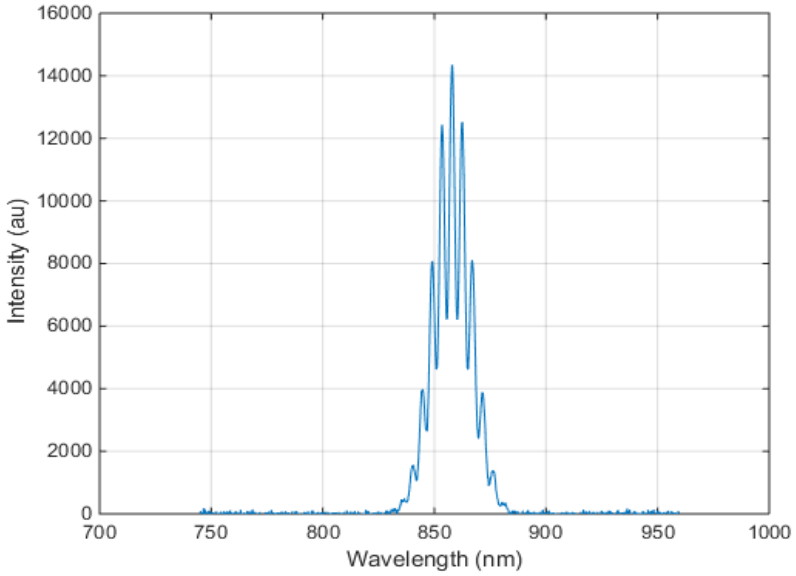

Figure 5.12 Interference spectrum of an EFPI pressure sensor

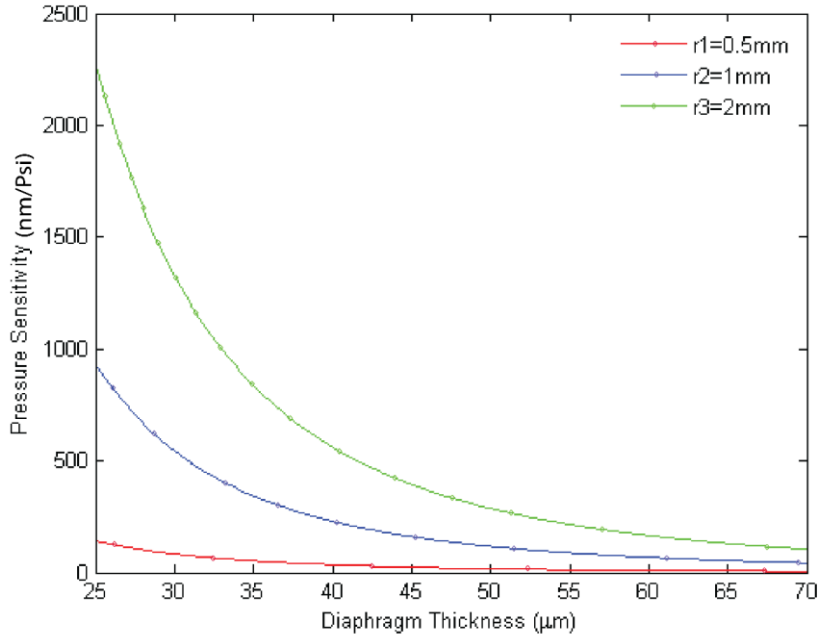

Figure 5.13 Pressure sensitivity against SiC diaphragm thickness and radius. The sensitivity is inversely proportional to the diaphragm thickness but directly proportional to the square of the effective radius.

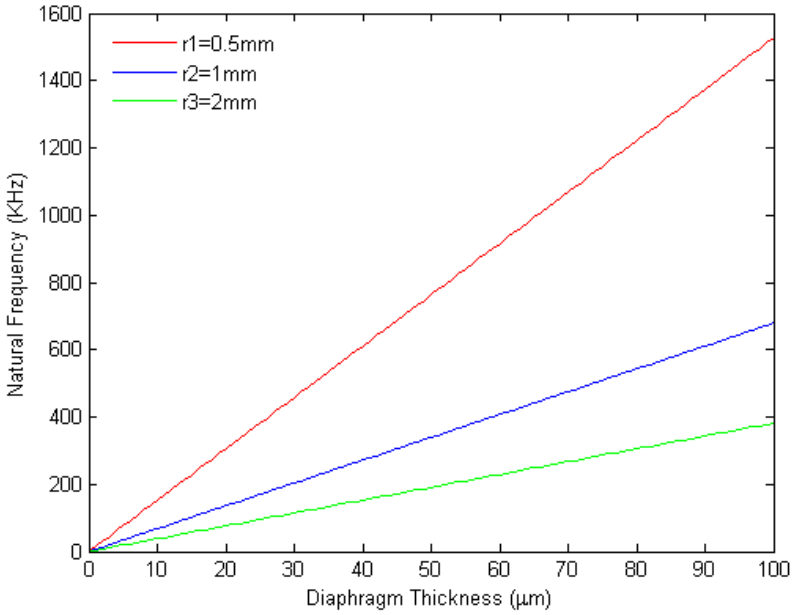

Figure 5.14 Natural frequency response as a function of SiC diaphragm thickness with different radius.

The frequency response of the SiC diaphragm against the thickness was also illustrated in this work. The frequency response is also a very important performance parameter when dynamic pressure range is considered. For the SiC diaphragm to operate within a linear range of dynamic pressure, the resonance frequency should be at least three to five times the highest applied frequency [27]. The analytical results for the frequency response is shown in Figure 5.14. The normalised frequency response increases with increase in SiC diaphragm thickness but decreases with increase in the diaphragm radius. For a thickness of $40\,\mu m$ and a diaphragm radius of $1\,mm$, the natural frequency of the SiC diaphragm is determined to be $225\,kHz$. This falls within the required specifications for most HPHT applications [28].

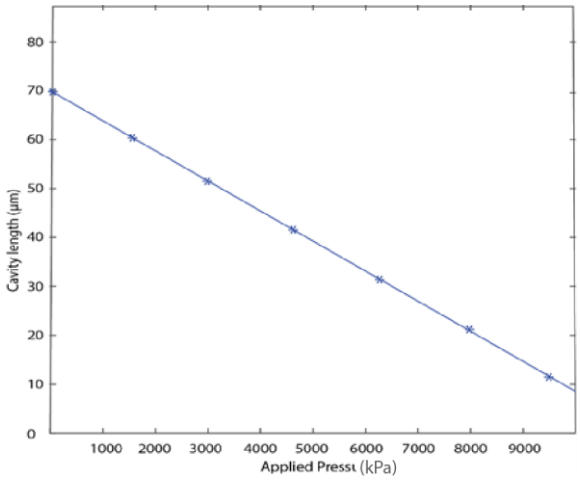

Figure 5.15 Pressure response as a function of cavity length.

Figure 5.15 derived from equation 5.15 shows that the result of the EFPI pressure sensor model is feasible. The relationship between the cavity length and the applied pressure on the metal coated sensing head remains linear from theoretical modelling and predictions. It shows that the cavity length decreases linearly with increase in pressure from $0 - 5000\,kPa$. The cavity length of the proposed sensor can be affected by the physical properties of the coated metals used like the thermal expansion coefficient and the thickness of the SiC diaphragm. The variation of the cavity length against the applied pressure was measured to be about $21\,\mu m\,kPa^{-1}$. However, temperature compensation may be necessary for high accuracy measurements. The proposed sensor was highly dependent on the material properties of the diaphragm. SiC has a Young's modulus of 420 GPa, making it very stiff and as such produced a very small deflection when the diaphragm was subjected to an external applied pressure. It should also be noted that the sensitivity of the proposed sensor was dependent on the stability of the cavity length. Due to the nature of the SiC

diaphragm, the cavity length tends not to drift over time which will enable the resolution and accuracy of the measurements to withstand long term reliability. Furthermore, the requirement for any specific cavity length in EFPI sensor design, depends on the pressure range for that applications. For subsea underwater applications, HPHT range measurements are required. Therefore, the proposed sensor design was carried out and could be used for reliable HPHT measurements in underwater applications. In this hybrid metal coated sensor design, there are few considerations to be noted. As a result of the usual high thermal expansion coefficient of metals, they may expand rapidly with higher temperature. Creeping tends to also occur on the metals with higher temperature. These characteristics of the metals will have influence over the performance of the proposed sensor.

5.5 Summary

This work detailed the description of a theoretical design of a hybrid FBG/EFPI sensor for measurements of temperature and pressure in harsh environments. The FBG is coated with outer protective layer of copper and inner layer of nickel, while the EFPI pressure sensor has an all SiC diaphragm with $1\,mm$ radius, thickness of $40\,\mu m$ and cavity length of $30\,\mu m$.

Theoretical models and analysis of this sensor were carried out. The optical analysis is carried out to obtain the spectral response of the sensor while the structural analysis is used to obtain the change in optical properties of the sensor due to photo-elastic effect. Also, the characteristics of a rigidly SiC diaphragm is used to determine the suitability of the sensing configuration.

The sensor was theoretically designed for ranges of temperature and pressure between $100 - 1000\,°C$ and $0 - 5000\,kPa$ respectively. Simulations of these models were done and results show that temperature sensitivity of the sensor

was enhanced from $13.95\,pm/°C$ to $23.89\,pm/°C$ and and the associated pressure range to be measured up to $5000\,kPa$ when compared to that of a single coated sensor. The proposed hybrid sensor maybe useful for measurements of HPHT in harsh environments.

This technique increases the measurement sensitivity of the sensor with respect to the wavelength shift peak when compared to the results obtained for the direct load on the glass capillary and aluminium material on the sensing configuration in chapter 4. Also, the double coating of the FBG is an effective protection to external stress and mechanical damages.

When the theoretical model of the coated metal sensor was simulated under harsh environmental conditions, the linear structural properties and the characterization of the sensor start to decrease. This shows that the technique is limited when the sensor is subject to extreme harsh environment. A robust, reliable and thin metal coating is desirable for such extreme environments. To effectively tackle the problem of temperature and pressure cross sensitivity in very extreme conditions like downhole operations and also address the limitation of the coated metal technique, the concept of ultra-thin sensing configuration with graphene diaphragm deposited in SiC is introduced in chapter 6.

5.6 References

[1] A. D. Kersey, "A Review of Recent Developments in Fiber Optic Sensor Technology," *Optical Fiber Technology,* vol. 2, pp. 291-317, 1996.

[2] K. T. V. Grattan and T. Sun, "Fiber optic sensor technology: an overview," *Sensors and Actuators A: Physical,* vol. 82, pp. 40-61, 2000.

[3] L. Y. Shao, A. P. Zhang, W. S. Liu, H. Y. Fu, and S. He, "Optical Refractive-Index Sensor Based on Dual Fiber-Bragg Gratings Interposed With a Multimode-Fiber Taper," *IEEE Photonics Technology Letters,* vol. 19, pp. 30-32, 2007.

[4] S. Webster, R. McBride, J. S. Barton, and J. D. C. Jones, "Air flow measurement by vortex shedding from multimode and monomode optical fibres," *Measurement Science and Technology,* vol. 3, p. 210, 1992.

[5] X. Li and F. Prinz, "Embedded Fiber Bragg Grating Sensors in Polymer Structures Fabricated by Layered Manufacturing," *Journal of Manufacturing Processes,* vol. 5, pp. 78-86, 2003.

[6] L. Xiao Chun, P. Fritz, and S. John, "Thermal behavior of a metal embedded fiber Bragg grating sensor," *Smart Materials and Structures,* vol. 10, p. 575, 2001.

[7] S. Sandlin, T. Kinnunen, J. Rämö, and M. Sillanpää, "A simple method for metal re-coating of optical fibre Bragg gratings," *Surface and Coatings Technology,* vol. 201, pp. 3061-3065, 2006.

[8] Y. Li, Y. Wang, and C. Wen, "Temperature and strain sensing properties of the zinc coated FBG," *Optik - International Journal for Light and Electron Optics,* vol. 127, pp. 6463-6469, 2016.

[9] L. Gang-Chih, L. Wang, C. C. Yang, M. C. Shih, and T. J. Chuang, "Thermal performance of metal-clad fiber Bragg grating sensors," *IEEE Photonics Technology Letters,* vol. 10, pp. 406-408, 1998.

[10] H. Kapels, R. Aigner, and C. Kolle, "Monolithic Surface-Micromachined Sensor System for High Pressure Applications," in *Transducers '01 Eurosensors XV: The 11th International Conference on Solid-State Sensors and Actuators June 10 – 14, 2001 Munich, Germany*, E. Obermeier, Ed., ed Berlin, Heidelberg: Springer Berlin Heidelberg, pp. 56-59, 2001.

[11] W. H. Ko and Q. Wang, "Touch mode capacitive pressure sensors," *Sensors and Actuators A: Physical,* vol. 75, pp. 242-251, 1999.

[12] K. Petersen, P. Barth, J. Poydock, J. Brown, J. Mallon, and J. Bryzek, "Silicon fusion bonding for pressure sensors," in *IEEE Technical Digest on Solid-State Sensor and Actuator Workshop*, pp. 144-147, 1988.

[13] Y. Zhan, C. Haiwen, J. Geng, R. Qu, S. Xiang, and X. Wang, *Study on aluminum groove encapsulating technique and sensing characteristics of FBG sensor* vol. 33, 2004.

[14] S.-T. Shiue, C.-H. Yang, R.-S. Chu, and T.-J. Yang, "Effect of the coating thickness and roughness on the mechanical strength and thermally induced stress voids in nickel-coated optical fibers prepared by electroless plating method," *Thin Solid Films,* vol. 485, pp. 169-175, 2005.

[15] X. Jian-Feng, Z. Hua, Z. Zhengqiang, X. Jian-Ning, H. Rong-Hua, and S. Lu-Fa, "A study of the temperature sensitivity of fiber Bragg gratings after metallization," *Smart Materials and Structures,* vol. 16, p. 1837, 2007.

[16] Z.-g. Zhang, F.-g. Su, M. Zhang, and P.-d. Ye, "Wavelength-shift detection system based on matching-FBG with enhanced temperature sensitivity," *Optoelectronics Letters,* vol. 2, pp. 139-141, 2006/03/01 2006.

[17] R. Rajini-Kumar, M. Suesser, K. G. Narayankhedkar, G. Krieg, and M. D. Atrey, "Performance evaluation of metal-coated fiber Bragg grating sensors for sensing cryogenic temperature," *Cryogenics,* vol. 48, pp. 142-147, 2008.

[18] C. Lupi, F. Felli, L. Ippoliti, M. A. Caponero, M. Ciotti, V. Nardelli, and A. Paolozzi, "Metal coating for enhancing the sensitivity of fibre Bragg grating sensors at cryogenic temperature," *Smart Materials and Structures,* vol. 14, p. N71, 2005.

[19] K. Tian, Y. Liu, and Q. Wang, "Temperature-independent fiber Bragg grating strain sensor using bimetal cantilever," *Optical Fiber Technology,* vol. 11, pp. 370-377, 2005.

[20] Y.-J. Chung, J.-S. Song, W.-T. Han, and U.-C. Paek, "New Compensation Method for Temperature Sensitivity of Fiber Brags Grating Using Bi-metal," *Journal of the Optical Society of Korea,* vol. 7, pp. 84-88, 2003

[21] S. Udoh, J. Njuguna, R. Prabhu, B. Chirappuram, and P. Radhakrishnan, "Preliminary Investigation of Temperature and Pressure Measurement System for Down-hole Monitoring of Oil Wells Using FBG/EFPI Sensing Technique.", SPE Nigeria Annual International Conference and Exhibition, 4-6 August, Lagos, Nigeria. 2015.

[22] Y.-S. Choi, Y.-H. Yoo, J.-G. Kim, and S.-H. Kim, "A comparison of the corrosion resistance of Cu–Ni–stainless steel multilayers used for EMI

shielding," *Surface and Coatings Technology,* vol. 201, pp. 3775-3782, 2006.

[23] R. Yun-Jiang, "In-fibre Bragg grating sensors," *Measurement Science and Technology,* vol. 8, p. 355, 1997.

[24] A. D. Kersey, M. A. Davis, H. J. Patrick, M. LeBlanc, K. P. Koo, C. G. Askins, M. A. Putnam, and E. J. Friebele, "Fiber grating sensors," *Journal of Lightwave Technology,* vol. 15, pp. 1442-1463, 1997.

[25] L. D. Landau, L. P. Pitaevskii, A. M. Kosevich, and E. M. Lifshitz, *Theory of Elasticity*: Elsevier Science, 2012.

[26] J. M. Gere and B. J. Goodno, *Mechanics of Materials*: Cengage Learning, 2012.

[27] D. Giovanni, *Flat and Corrugated Diaphragm Design Handbook*: Taylor & Francis, 1982.

[28] C. M. Zetterling, "Present and future applications of Silicon Carbide devices and circuits," in *Proceedings of the IEEE 2012 Custom Integrated Circuits Conference*, pp. 1-8, 2012.

Chapter 6

6 Analysing the applicability of multilayer graphene diaphragm for oil and gas sensing applications

6.1 Introduction

In this chapter, a novel thin-film fibre optic FBG/EFPI sensor with ultra-high pressure and temperature sensitivities is theoretically analysed using 16-layer graphene film deposited on SiC substrate as the diaphragm. The sensitive diaphragm structure breaks the sensitivity limitations imposed by the increased thickness and the decreased dimension of a diaphragm used in traditional FPI pressure sensors. The interaction between the multilayer graphene with an inner diameter of $125\,\mu m$ and the SiC substrate created a low finesse FP interferometer with a cavity length of $59.67\ \mu m$. It was observed in the numerical study that the sensitivity can be greatly increased by using multilayer graphene on SiC substrate. The performance parameters of the proposed sensor are investigated in terms of sensitivity at the operating wavelength of $1550\,nm$ and the proposed sensor exhibits an ultra-high pressure sensitivity of $2380\,nm\,kPa^{-1}$ and temperature sensitivity of $1.02\,nm\,°C^{-1}$. This addresses the temperature and pressure cross sensitivity for HPHT environments. This sensor is expected to have potential for monitoring oil and gas applications in harsh environments.

The recent renewed interest in utilizing miniature fibre optic sensors for pressure/temperature monitoring in the oil and gas industry due to their advantages over conventional sensors, such as immunity to electromagnetic interference, high resolution, fast response, and compact

size [1]. The pressure sensors that are based on the FPI have shown promising results for obtaining static and dynamic pressure measurements [2, 3]. The pressure sensitivity of the diaphragm in the FPI sensor is defined as the ratio of the FPI cavity's length variation to the pressure [4]. Among the key elements that determine the pressure sensitivity of the FPI sensor are the used materials and the thickness of the diaphragm. Several thin-film FPI pressure sensors have been reported in the literature and these sensors used different materials as the pressure-sensitive diaphragm. Some of the materials used are polymer, silicon, silver and graphene [3-9]. However, achieving a thin-film FPI sensor with high pressure sensitivity, leads to reduction in the thickness of the diaphragm for the most effective methods used in the literature.

Silica-based sensors have superior chemical stability, thermal stability and mechanical strength [10]. However, they usually have limited sensitivity due to the high elastic moduli of the material. In addition, the thickness of the silicon diaphragm is usually larger than $3\,\mu m$, and the mass production of a silicon-based diaphragm with a thickness of less than $1\,\mu m$ is difficult to achieve. In contrast, the polymer diaphragm can be thinned down to a few microns and is suitable for mass production. Thus, polymer-based pressure sensors can obtain higher sensitivity. However, the polymer diaphragm is limited in its sensing applications due to its porous cellar structure and instability in a water vapour environment [11]. In recent years, Xu et al reported a fibre-tip pressure sensor with $125\,\mu m$ diameter and $130\,nm$ thick silver diaphragm and achieved a pressure sensitivity of $70.5\ nm\,kPa^{-1}$ [6]. The aforementioned research indicated that a thinner material is much more promising for use as a high-sensitivity pressure-sensitive diaphragm.

Graphene, with a single layer thickness of $\sim 0.335\, nm$, has been utilized more since it was first isolated by Novoselov et al [12] because of its extreme elasticity [13], ultra-strong adhesion [14], and impermeability to gases [15]. The unique combination of electronic and mechanical properties makes graphene an ideal material for sensor applications involving electromechanical coupling, such as micro machined pressure sensor [16, 17]. The ultra-thin thickness of graphene can significantly improve the pressure sensitivity of FPI sensors. Recently, graphene membranes with thickness ranging from 0.26 to $0.76\, nm$ were used as deflectable diaphragms for FPI sensors. A pressure sensitivity of $39.2\, nm\, kPa^{-1}$ was exhibited using a diaphragm with a diameter of $25\, \mu m$ [18]. The small size of the diaphragm in a miniaturized sensor head imposes a limit on its sensitivity. By using a $\sim 100\, nm$ thick graphene diaphragm with a diameter of $125\ \mu m$, Ma $et\ al$ fabricated a FPI acoustic sensor with a dynamic pressure sensitivity of $1100\, nm\, kPa^{-1}$, which was the highest reported [19]. However, considering the nanoscale deflection deformation of graphene membranes under loads, the used diaphragm is still so thick that the measured load-deflection behaviour is no longer consistent with the corresponding large deflection characteristics.

To overcome the challenges in each of graphene materials and SiC as reported, the growth of graphene with large crystalline domain on the uniform surface of SiC is necessary. Several methods of growing graphene on SiC substrate have been reported [20-26]. The combined metals form a stronger cohesive strength and extreme chemical stability, does not need to be transferred from the metal to another dielectric substrate, has a large band-gap and can be easily be integrated into silicon. These qualities, make it suitable for more technological industrial applications. To combine the advantages of both graphene and SiC,

we're motivated to use these two materials in a single sensor which increases sensitivity.

This chapter demonstrates and examines the interference characteristics and the large scale deflection behaviour of an FPI pressure sensor with an ultra-thin 16-layer graphene film with $125\,\mu m$ diameter deposited on SiC substrate as the diaphragm membrane. A numerical model of highly sensitive Graphene-SiC based sensor is proposed for practical oil and gas monitoring applications. The sensitivity of this sensor overcomes the sensitivity limitation (Increased thickness and decreased dimension of the diaphragm) of the conventional FPI pressure sensor. Mathematical models and design considerations of the proposed sensor are discussed in section 6.2. Results and discussions are detailed in section 6.3, while section 6.4 gives the summary.

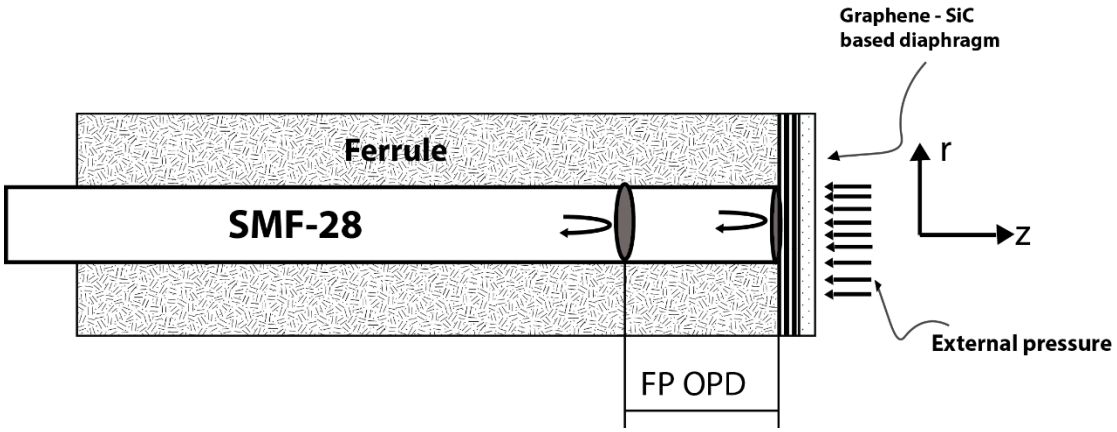

Figure 6.1 FPI interference characterization of multiple layer graphene on SiC substrate

6.2 Structure and operating principle of the FPI sensor with graphene-SiC diaphragm

The change in cavity length or the optical path difference (OPD) of an FPI sensor leads to pressure sensitivity measurement, which depends on the

transducer mechanism and the graphene-SiC based diaphragm thickness as shown in Figure 6.1. The diaphragm as a light reflector, made directly on the endface of the fibre and it adheres to the ferrule by the van der Waals force. When the diaphragm is subject to an external pressure, the deformation of the diaphragm membrane will cause the the FPI OPD to change. This change is as a result of the deflection of the diaphragm when there is difference in pressure between the inside and outside surfaces of the diaphragm. The deflection of the diaphragm is determined by detecting the intensity of the reflected light. For the purpose of this load-deflection modelling, the sensor is modelled as a clamped multiple dielectric slabs. Thus, the interference characterization and the large deflection behaviour of the graphene-SiC diaphragm can be investigated.

6.2.1 Thin film interference theory and model

The characteristic reflectivity of a thin film as a result of multiple beam interference has been extensively studied in the literature [27]. For a thin film with non-absorbing layer of thickness h and refractive index $n1$ bounded by two semi-infinite media with refractive indices $n0$ and $n2$, the reflectivity can be obtained theoretically by summing all the amplitudes of the reflected light beams. Multiple reflections may also occur within the layer Figure 6.2. When two optical interfaces with each having a Fresnel coefficients characteristics for reflection and transmission, the incident beam will split into multiple coherent waves.

The r_{ij} and t_{ij} are the corresponding Fresnel reflection and transmission coeficients at the optical interface i and j denoted in order of the propagation direction od the rays [28]. To determine r_{ij} and t_{ij}, the polarisation of the beam needs to be considered.

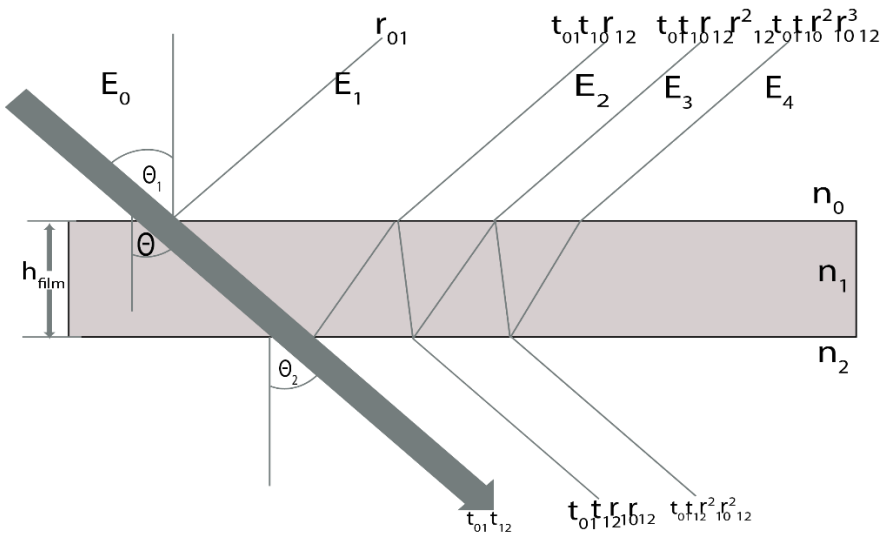

Figure 6.2 Thin film interference of Fresnel coefficients characteristics for reflection and transmission which shows how the incident beam will split into multiple coherent waves.

When the reflected coefficients are considered, there will be a number of higher order reflected waves $(E_1,\ E_2,\ E_3, \dots)$ which will result into colour appearance of the thin film. This is a characteristic of the film thickness h and the refractive index n_1.

The optical path difference due to the thin film for adjacent rays is expressed as [28]

$$\Delta = 2n_1 h_{film} cos\theta_1 \tag{6.1}$$

and the corresponding phase shift is given as [28]

$$\partial_m = (m+1).\frac{2\pi}{\lambda} n_1 h cos\theta_1 \tag{6.2}$$

m is the number of total internal reflections which is always an odd number, θ_1 is the angle of refraction in the layer.

The resulting complex reflected amplitude which is the summation of the overal amplitudes taking into account the phase shift is expressed as

$$I_r = r_{01} + t_{01}r_{12}t_{10}exp^{-2i\partial}\sum_{n-1}^{\infty}(-1)^n(r_{12}r_{10})^n exp^{-2in\partial}$$

$$= r_{01} + \frac{t_{01}r_{12}t_{10}exp^{-2i\partial}}{1 + r_{10}r_{12}exp^{-2i\partial}}$$

$$= \frac{r_{01} + r_{12}exp^{-2i\partial}}{1+r_{10}r_{12}exp^{-2i\partial}} \quad (6.3)$$

where $t_{01}t_{10} = \sqrt{1 - r_{01}^2}\sqrt{1 - r_{10}^2} = 1 - r_{01}^2$

For a lossless dielectric media where energy of the reflected and transmitted waves are conserved, the reflectivity of a thin film is given as

$$R = \frac{r_{01}^2 + r_{12}^2 + 2r_{01}r_{12}cos2\partial}{1+r_{01}^2r_{12}^2+2r_{01}r_{12}cos2\partial} \quad (6.4)$$

6.2.2 Multilayer reflectivity model

From the theory of multiple layer interference, the reflectance nature of the multilayer transparent, dielectric layers with different refractive indices can be

obtain through the reflected incident light from the different optical interfaces.

The multiple layer stack with N number of layers of two distinct materials with refractive indices $n1$ and $n2$ where $n1 > n2$ and the thin film thicknesses of $h1$, $h2$. The multiple layer stack is covered at both the top and the bottom by two media with refractive indices of $n0$ and nc

The incidence light touches on the multilayer stack at an angle θ_0 is shown in Figure 6.

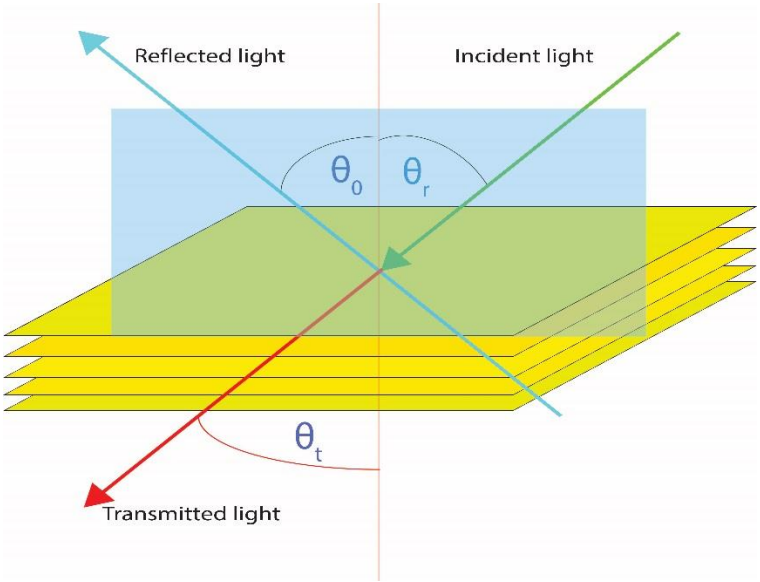

Figure 6.3 Multilayer Reflection and Transmission of light beams. Light beams will reflect at different interfaces of the stack resulting into characteristic reflection and transmission spectra depending on the refractive index and thickness of the material.

6.2.3 The transfer matrix based optical modelling

The Transfer Matrix Optical Modelling is one of the methods used to calculate the optical interference of multilayer stack of thin films. In this work, the transfer method is used to determine the reflectance and transmittance of a thin film multilayer stack. The transfer matrix method relates the electric and magnetic fields at the interfaces through the characteristic matix [29].

The reflectivity of the multilayer stack can be calculated as a function of the wavelength of the incident light λ, the refractive indices $n1$, $n2$, $n3$ …, the thin film thicknesses $h1$, $h2$, $h3$…. of the individual layer, the incidence angel of the light θ_0, the number of layers in the multilayer stack N.

For a dielectric material that is transparent in the multilayer stack, the i^{th} layer is defined by it's refractive index n_i and the layer thickness h_i. The equations used are summarized in the following section.

The boundary conditions for a thin film multilayer stack interference when considering the interface $0{,}1$ of the first layer is expressed as [27]

$$E_{0i} + E_{0r} = E_{1i} + E_{1r}$$

$$n_0 E_{0i} - n_0 E_{0r} = n_1 E_{1i} - n_1 E_{1r}$$

And at interface $1, 2$ of the layer;

$$E_{1i} exp^{ikh} + E_{1r} exp^{-ikh} = E_t$$

$$n_1 E_{1i} exp^{ikh} - n_1 E_{1r} exp^{-ikh} = n_2 E_t$$

The phase difference due to traversal of the thin film is given as;

$$\partial = (m+1).\frac{2\pi}{\lambda} n_1 h cos\theta_1 \tag{6.5}$$

Combining the above set of equations into an equivalent matrix representation to obtain;

$$\begin{bmatrix} 1 \\ n_0 \end{bmatrix} + \begin{bmatrix} 1 \\ -n_0 \end{bmatrix} \frac{E_{0r}}{E_{0i}} = \begin{bmatrix} cos\partial & -\frac{i}{n_1} sin\partial \\ -in_1 sin\partial & cos\partial \end{bmatrix} \begin{bmatrix} 1 \\ n_2 \end{bmatrix} \frac{E_t}{E_{0i}}$$

which can be written as

$$\begin{bmatrix} 1 \\ n_0 \end{bmatrix} + \begin{bmatrix} 1 \\ -n_0 \end{bmatrix} \mathcal{R}_i = M \begin{bmatrix} 1 \\ n_2 \end{bmatrix} T_i \tag{6.6}$$

$\mathcal{R}_i$ and T_i are the reflection and tramission coefficients respectively and M is the transfer matrix. For structures with N-number of layers, a transfer matrix is required for each layer and the product M_T is the light transmission throught the entire multilayer stack which is expressed as;

$$\begin{bmatrix} 1 \\ n_0 \end{bmatrix} + \begin{bmatrix} 1 \\ -n_0 \end{bmatrix} \mathcal{R}_i = M_1 M_2 M_3 \dots M_N \begin{bmatrix} 1 \\ n_2 \end{bmatrix} T_i = M_T \begin{bmatrix} 1 \\ n_2 \end{bmatrix} T_i$$

Where M_T is the product of the different transfer matrices. The components of the transfer matrix M_T can be represented as;

$$M_T = \begin{bmatrix} m_{11} & m_{12} \\ m_{21} & m_{22} \end{bmatrix}$$

The reflection and transmission coefficients $\mathcal{R}_i$ and T_i can also be represented in terms of the components of M_T for s-polarization as [27];

$$\mathcal{R}_i = \frac{n_0 m_{11} + n_0 n_2 m_{12} - m_{21} - n_2 m_{22}}{n_0 m_{11} + n_0 n_2 m_{12} + m_{11} + n_2 m_{22}}$$

$$T_i = \frac{2n_2}{n_0 m_{11} + n_0 n_2 m_{12} + m_{11} + n_2 m_{22}}$$

The reflectance $\mathcal{R}$ and transmittance T are now given by;

$\mathcal{R} = \mathcal{R}_i \mathcal{R}_i^*$ and $T = \frac{n_2}{n_0} T_i T_i^*$

For the effect of absorption in thin film, a complex refractive index is considered and this is specified by;

$$n - ik$$

Where n is the complex refractive index and k is the extinction coefficient. The thin film absortion is given by;

$$A = 1 - \mathcal{R} - T$$

With this, a multilayer thin film stack can be specified on any substrate and surface plots of reflection, transmission and absorption can be determined for both the s-polarization and p-polarization.

The reflectivity of the multilayer stack can be obtained by solving the transfer matrix equation [27]

$$\mathcal{R} = |r|^2 = \left| \frac{i\left(\frac{1}{N_1} - N_1\right)\sin\left(\frac{2\pi}{\lambda} N_1 h\right)}{2cos\left(\frac{2\pi}{\lambda} N_1 h\right) + i\left(\frac{1}{N_1} + N_1\right)\sin\left(\frac{2\pi}{\lambda} N_1 h\right)} \right|^2 \tag{6.7}$$

To determine the reflectivity $\mathcal{R}$, the complex refractive index of each layer and it's thickness need to be known. For multilayer graphene-SiC configuration shown in Figure 6.4, the first layer can be considered as part of the multilayer stack. The amplitude of the electric field $\boldsymbol{E}$ is divided into two components; the reflected component, E^- and the transmitted component, E^+. The refractive indices and thicknesses of all the layers are considered as follows. The complex refractive index of graphene is considered as approximately $n = 3.69 - j2.51$ [30-32] while its thickness is considered as $h = 0.34L\ nm$, where L is the number of graphene layers.

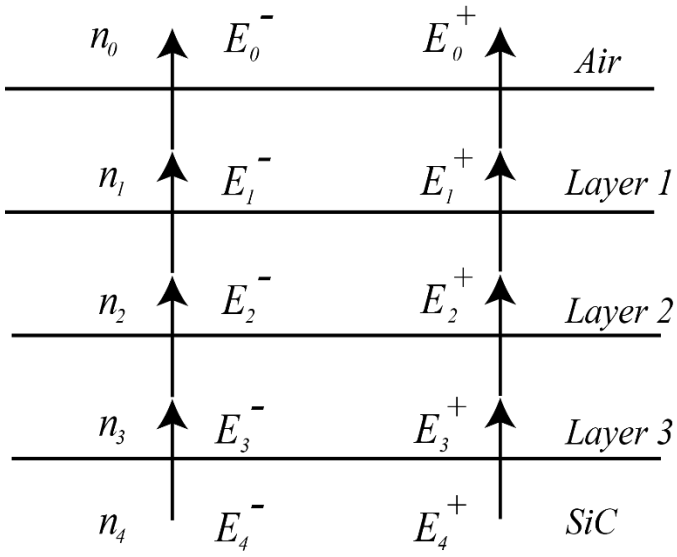

Figure 6.4 Schematic of electric field notation in the 3-layer graphene on SiC structure. The prime denotes waves at the down side of an interface.

6.3 Results and Discussion

The transfer matrix method was implemented in MATLAB. The algorithm allows for the variation of the multilayer graphene-SiC parameters like the refractive indices, thickness, number of layers and the angle of light incidence.

The reflectivity of the multilayer stack with refractive indices n_1 and n_3 depends on the refractive index contrast, the thickness of the layers, the polarisation of the light, and the angle of light incidence. The relationships between the transmittance and absorbance with respect to both the angle of incidence and wavelength are showed in Figure 6.5. It is evident from the results that multi-layered graphene on SiC presents high transmittance and low absorption in both the visible and near infra-red (NIR) spectrum of light.

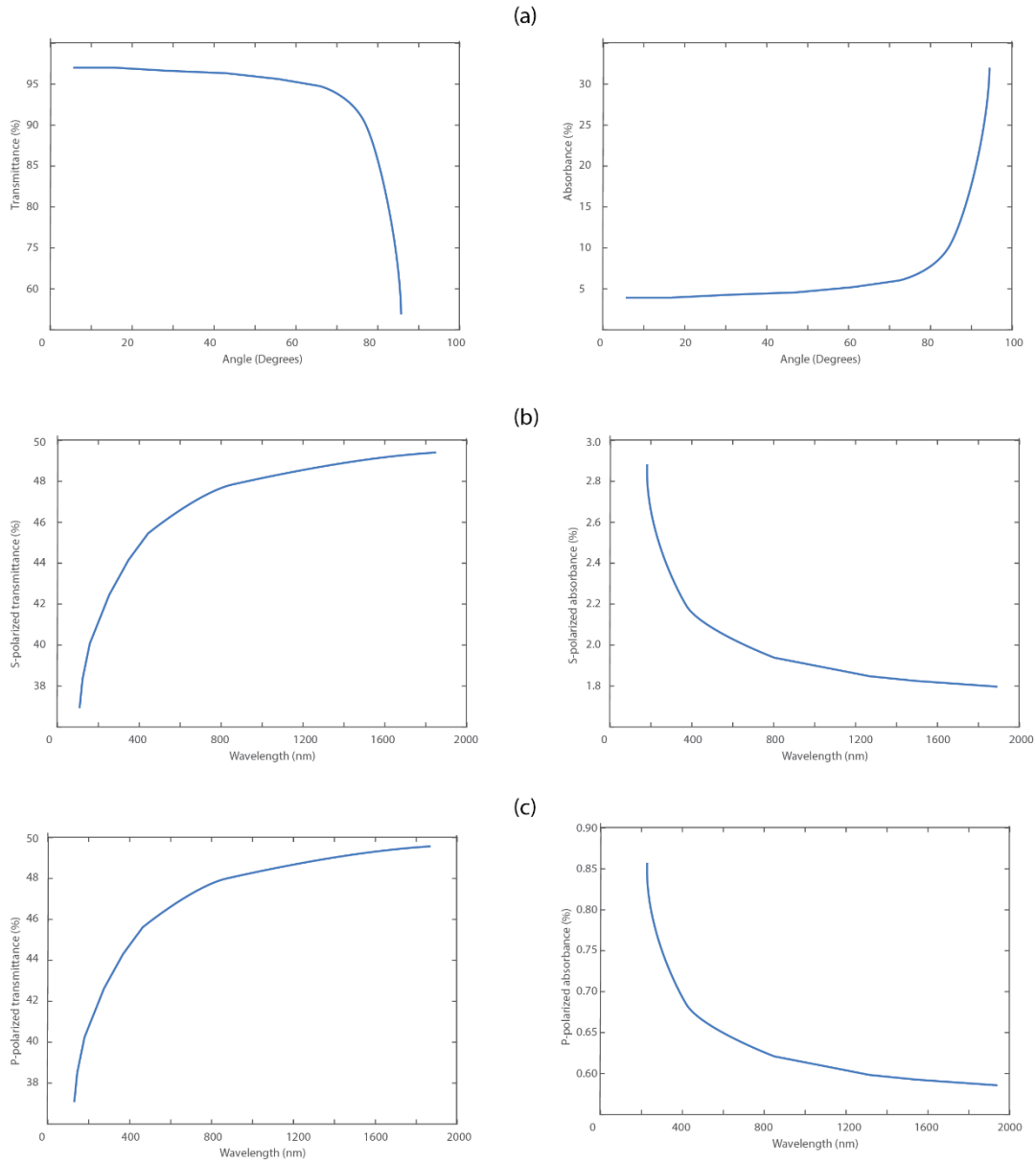

Figure 6.5 Transmittance and absorbance of multilayer graphene on SiC substrate. (a) transmittance and absorbance of multilayer graphene on SiC with respect to the angle of incidence (b) s-polarized transmittance and absorbance of multilayer graphene on SiC as a function of wavelength (c) p-polarized transmittance and absorbance of multilayer graphene on SiC substrate as a function of wavelength.

Recent work by [31, 32] demonstrated the optical functions of graphene in terms of the complex refractive index n and k as shown in Figure 6.6. The

general trend between the n and k shows values reasonably close in the visible light region and continue to increase with wavelength leading to the infrared region. The effect of the number of graphene layers on the reflectivity at a typical wavelength of $1550\,nm$ are shown in Figure 6.7. When light is incident on the graphene surface, part of the light is reflected back through the cavity length to the optic fibre while the remaining is transmitted through the graphene to the SiC.

The result shows that the reflectivity of the graphene membrane is greatly improved as the number of layers increases. This can enhance the interference signal demodulation.

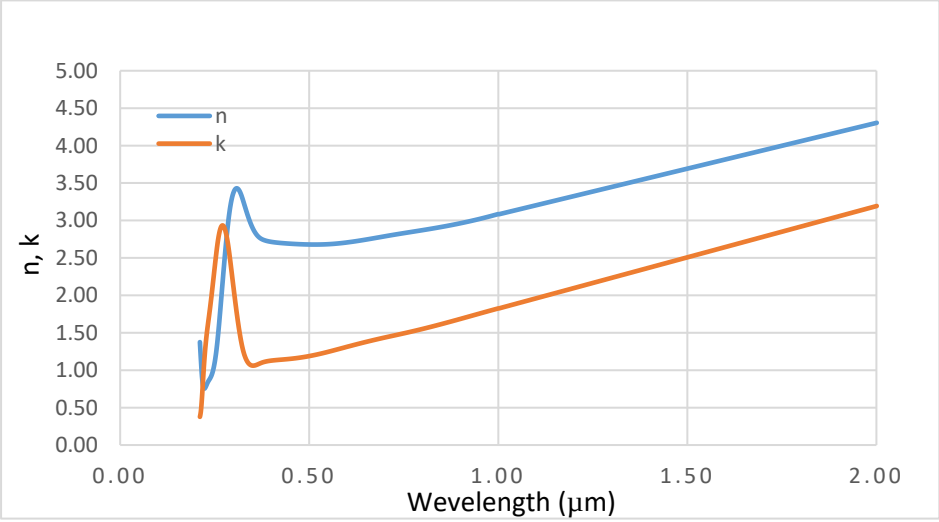

Figure 6.6 Real and imaginary parts n and k as the components of the complex refractive index of graphene as a function of wavelength.

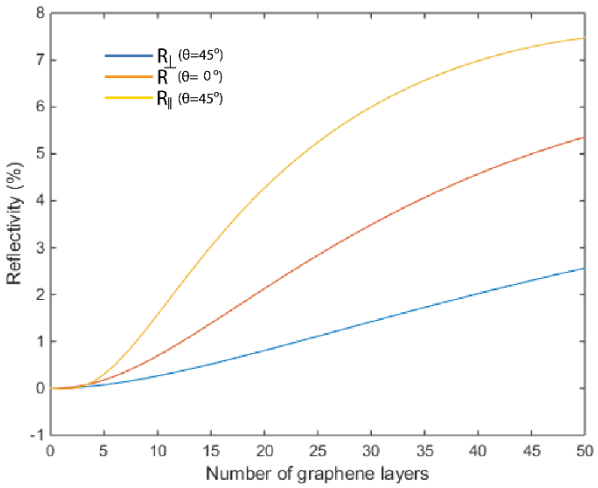

Figure 6.7 Simulated reflectivity versus number of graphene layers. The complex refractive index used in this simulation is $3.69 - j2.51$ at $1550\,nm$

It is observed that as the reflectivity of the graphene diaphragm increases as a result of the increase in the thickness of the diaphragm, it reaches a certain point where the reflectivity starts to decrease. This is as a result of the complex refractive index dominance of the graphene.

It is also interesting to note that the wavelength has no significant effect on the reflectivity of the of the graphene membrain at a particular thickness. Considering a 8-layered graphene as depicted in our simulation, when light is incident on this layered graphene at wavelengths of $1550\,nm$ and $1600\,nm$, the reflectivity is computed to be 62.48% and 65.56% respectviely. This shows that the effect of wavelength on the reflectivity of the graphene diaphragm is inconsequencial. For this work however, the wavelength of $1550\,nm$ is used for the interference and characterization performance of the graphene diaphragm.

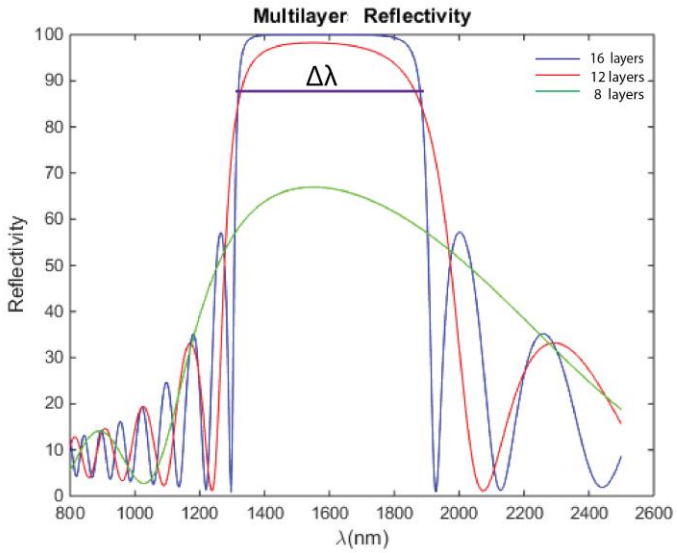

Figure 6.8 Multilayer reflectivity versus wavelength for different layer numbers N at normal light incidence.

Figure 6.8 shows the multilayer reflectivity response as a function of wavelength for different number of layers N at normal incidence light. The reflectivity of the multilayer structure also depends on the polarization of the incident light, the thickness of the individual layers and the angle of the incidence light. The incident medium is air with refractive index of $n = 1$. The graph shows the response for cases where $N = 8, 12, 16$. The design wavelength is $\lambda_0 = 1550\, nm$

As shown in Figure 6.8, when the number of layers N increases, the reflectivity also increases while the bandwidth of the reflected peak decreases. The wavelength bandwidth can be calculated from the graph as $\Delta\lambda = 568\, nm$. The bandwidth covers most of the visible spectrum in the graph. As the number of layer N increases, the reflection response tends to flaten at the edges as it tends towards 100%. This is an asymptotic representation of the reflecting band.

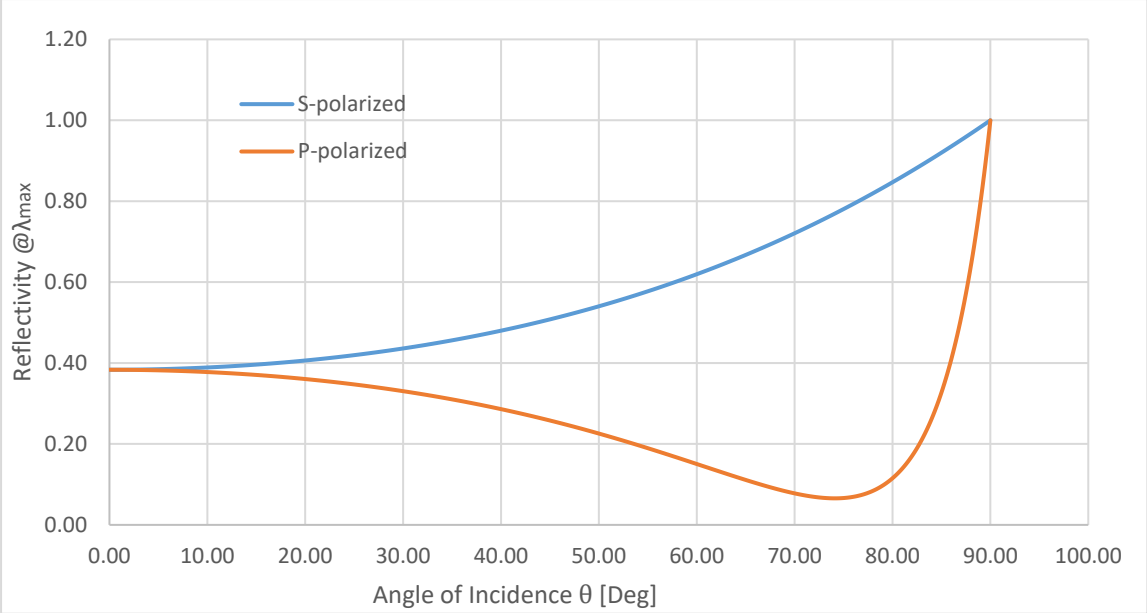

Figure 6.9 Reflectivity as a function of polarisation of incidence light for multilayer graphene

As the incidence angle of light increases, the reflectivity of s-polarized light increases monotonically towards unity while the reflectivity of p-polarized first decreases, reaching a minimum value of 0.07 at the Brewster angle [33] $Q_b = 76.2°$ before increasing towards unity as shown in Figure 6.9. The point at which the reflectivity of the p-polarised light drops drastically is known as the Brewster angle Q_b

6.3.1 High temperature measurement based on FPI graphene on SiC substrate as the diaphragm

The interference pattern of the FPI is shown in Figure 6.10 and the pattern is analysed in which the cavity length of the FPI can be calculated from

$$L = \frac{(\lambda_1 \lambda_2)}{2(\lambda_1 - \lambda_2)}$$

where λ_1 and λ_2 $(\lambda_1 > \lambda_2)$ are the two adjacent wavelengths of dips in the interference spectrum.

As the phase difference satisfies the condition of the interference, the dip wavelength can be expressed as

$$\lambda_m = \frac{2n_{eff}L_{eff}}{m} \tag{6.8}$$

It can be noted that the wavelength depends on the effective refractive index n_{eff} and the cavity length L_{eff}. The thickness of the diaphragm and the refractive index are functions of temperature. The relationships showing the effective refractive index and the effective cavity length as functions of temperature are expressed as,

$$n_{eff}(T) = n_{eff}(T_0)(1 + \sigma\Delta T)$$

$$L_{eff}(T) = L_{eff}(T_0)(1 + \alpha_g\Delta T)$$

where α_g is the thermal expansion coefficient and σ is the thermo-optic coefficient of the graphene on SiC diaphragm respectively.

By differentiating equation 6.8, the wavelength shift with respect to temperature can be expressed as,

$$\frac{d\lambda_m}{dT} = \frac{2n_{eff}(T_0)L_{eff}(T_0)}{m}\{\sigma + \alpha_g + 2\alpha\sigma\Delta T\} \tag{6.9}$$

This equation shows that the temperature sensitivity of the sensor is a function of the thermo-optic coefficient and the thermal expansion coefficient of

graphene on SiC diaphragm. However, the thermo-optic coefficient and the thermal expansion coefficient do not affect the shift in wavelength. The wavelength shift is only affected by the variation of the graphene diaphragm. The thermo-optic coefficient and the thermal expansion coefficient of graphene have been estimated to be on the order of $10^{-4}/k$ [34] and $10^{-5}/k$ [35, 36]. It can be seen from Figure 6.10 that the signal gives a cosine waveform that is generated by two beam interference. This shows the interference spectrum of the sensor with fringe contrast of $20\,dB$ at each wavelength. It can be seen that there are two peaks and three dips in the interference patterns where the maximum and minimum occur. The cavity length is calculated to be $59.67\,\mu m$ from the spectrum.

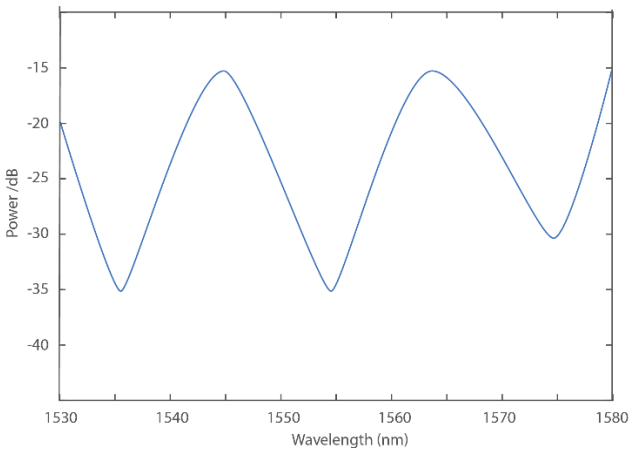

Figure 6.10 The interference pattern of the proposed multilayer graphene on SiC substrate.

To examine the dependence of temperature on FPI cavity sensor, the sensitivities under different range of temperature are examined. The fringe dip wavelengths are selected at $1535\,nm$ and $1575\,nm$ to depict the wavelength shift under low and high temperature. As shown in Figure 6.11, the wavelength shift

increases as temperature increase. A good linearity is achieved with temperature sensitivities of $0.75\ nm/°C$ and $1.02\ nm/°C$ at low temperature range of $20\ °C$ to $65\ °C$ and high temperature range of $1000\ °C$ to $1050\ °C$ respectively. This proposed FPI sensor has a temperature sensitivity to be three orders of magnitude larger than the one proposed by Tafulo *et al* [37]

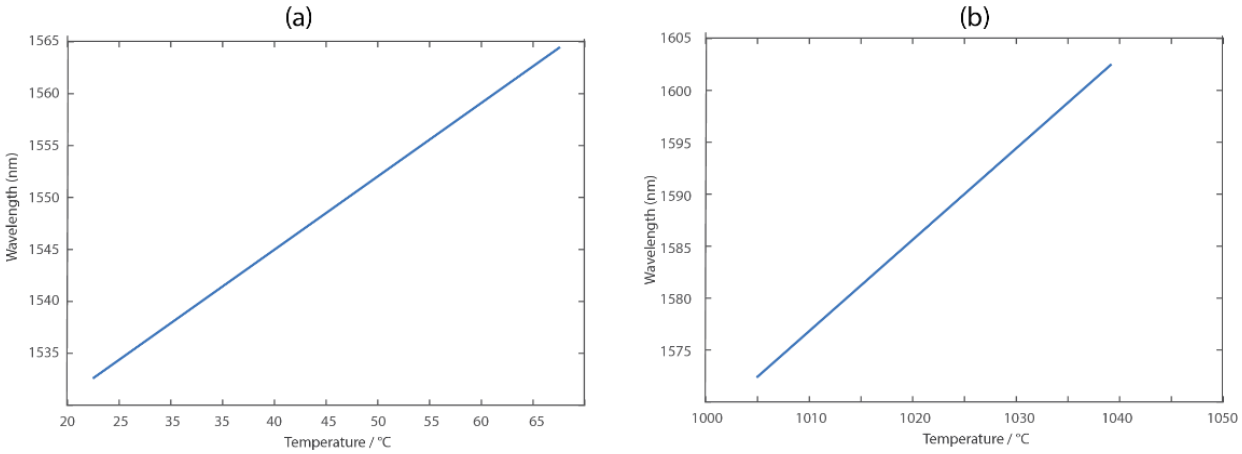

Figure 6.11 Wavelength shift with temperature variation. (a) dip wavelength shift with low temperature range (b) dip wavelength shift with high temperature range

The fringe contrast of the interference spectrum is given by [38]

$$FC = 20\log_{10}\left[\left|\frac{\sqrt{R}+K(1-R)|(n_g-1)|/(n_g+1)}{\sqrt{R}-K(1-R)|(n_g-1)|/(n_g+1)}\right|\right] \tag{6.10}$$

where $K = (1-A_1)(1-\alpha)$ is the total loss factor of the sensor head, A_1 is the transmission loss factor at the reflected surface due to surface imperfection or roughness and α is the loss factor of the cavity caused by diffraction of the graphene diaphragm cavity. For this design, we ignored the surface

imperfections for simplicity of the model. The fringe contrast decreases with increase in temperature as showed in Figure 6.12.

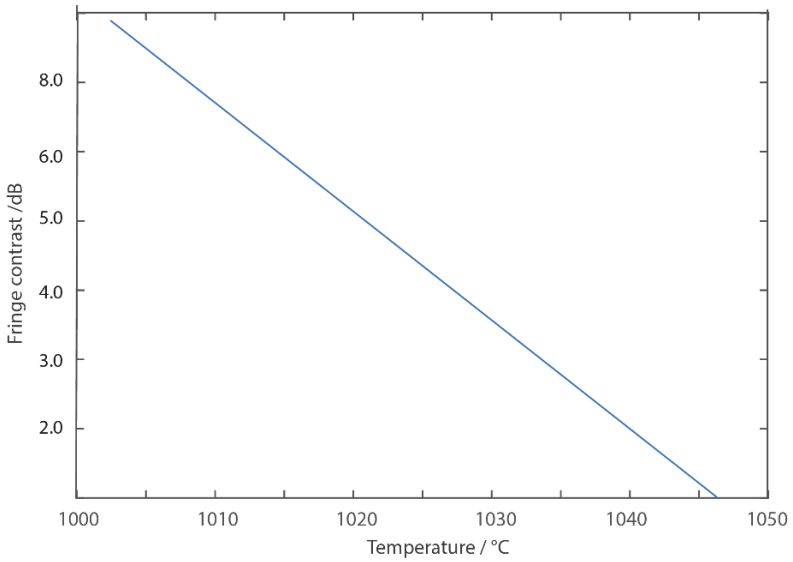

Figure 6.12 Fringe contrast with temperature variation from 1000 °C to 1050 °C

6.3.2 High pressure measurement based on FPI graphene on SiC substrate as the diaphragm

Fringe visibility as one of the performance design parameters is also analysed. Figure 6.13 shows the fringe visibility as a function of different cavity lengths. As expected, the visibility of the reflected light decreases with increase in cavity length. The fringe visibility only drops about 15% from 100% to 85% when the cavity length increases from $0-50\,\mu m$ for the 50% reflectivity response. It can also be seen that the fringe visibility decreases more quicker as the cavity length becomes larger. In most practical applications, FPI sensors usually have cavity length less than $100\,\mu m$. For this design, the interference spectrum

exhibits a fringe visibility of approximately $70\,\%$ with a diaphragm diameter of $125\,\mu m$ for a $59.67\ \mu m$ cavity length. The degradation of fringe visibility as a result of cavity length is acceptable in most applications.

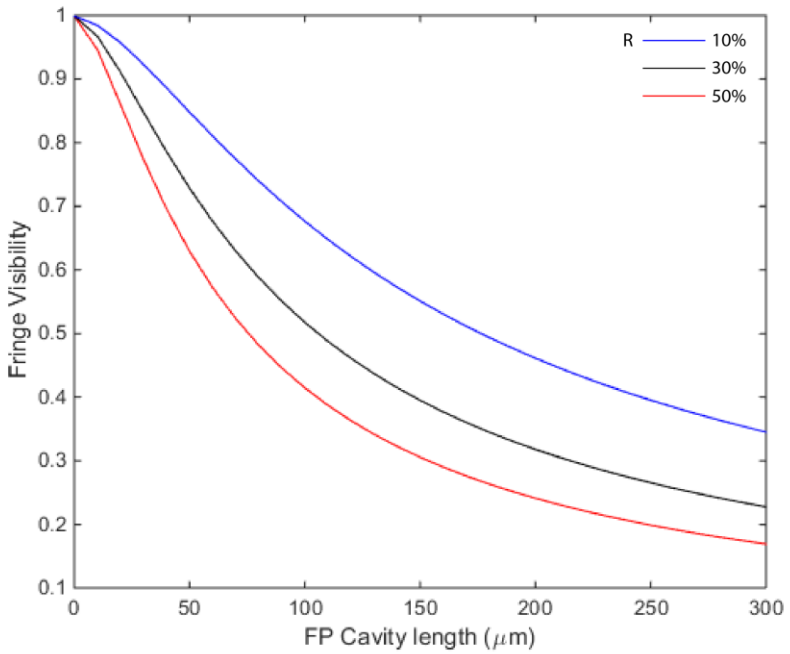

Figure 6.13 Fringe visibility as a function of cavity length for multilayer graphene.

The interference characterisation and efficiency of the 16-layered graphene diaphragm had shown better perfomance when compared to others. The optical interference signal can be extracted when the FPI sensor is subjected to external pressure. However, the number of graphene layers will have effect on the pressure sensitivity.

Figure 6.14 shows the result of centre deflection against applied external pressure. The sensitivity for the 16-layer graphene is approxiamtely $2380\ nm\ kPa^{-1}$.

For graphene diaphragm and radius of $12.5\,\mu m$ and $62.5\,\mu m$ respectively, the centre deflections against applied external pressures is shown in Figure 6.14(a) and Figure 6.14(b). To compare the sensitivity against applied pressures of few layer (2~5) graphene and multilayer graphene, the deflections of few layer graphene are included in the plots.

Results show that the sensitivity increases as the diameter increases. It is also seen that the sensitivity of the multilayer graphene is much more than that of few layer (2~5). This suggests that ultra thin multilayer graphene on SiC substrate has the potential for monitoring oil and gas applications in harsh environment.

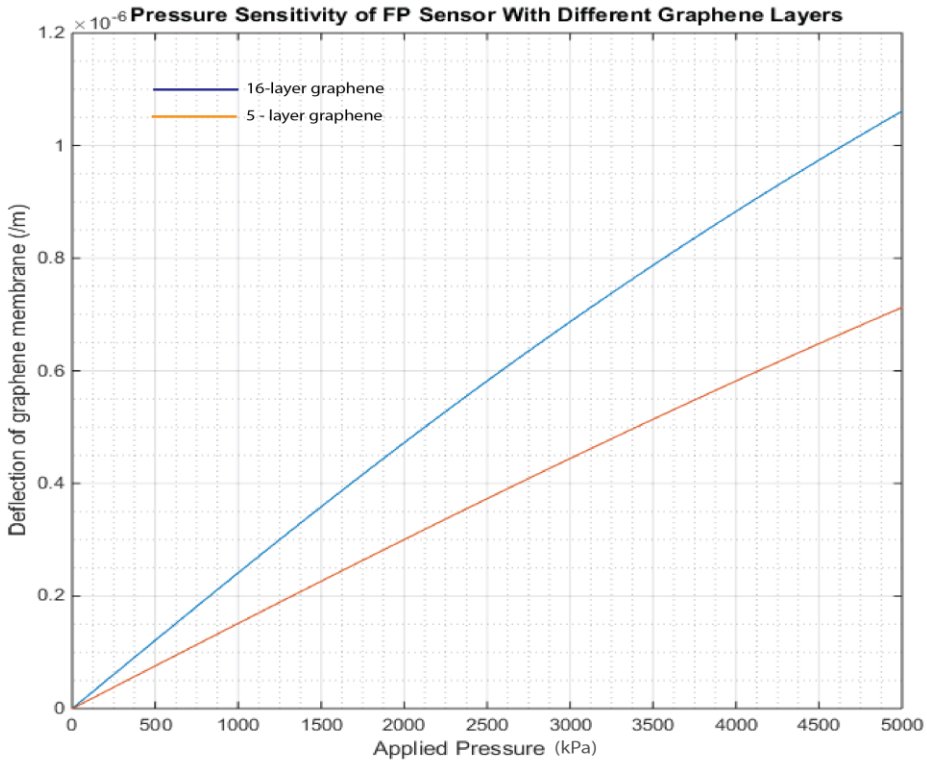

(a)

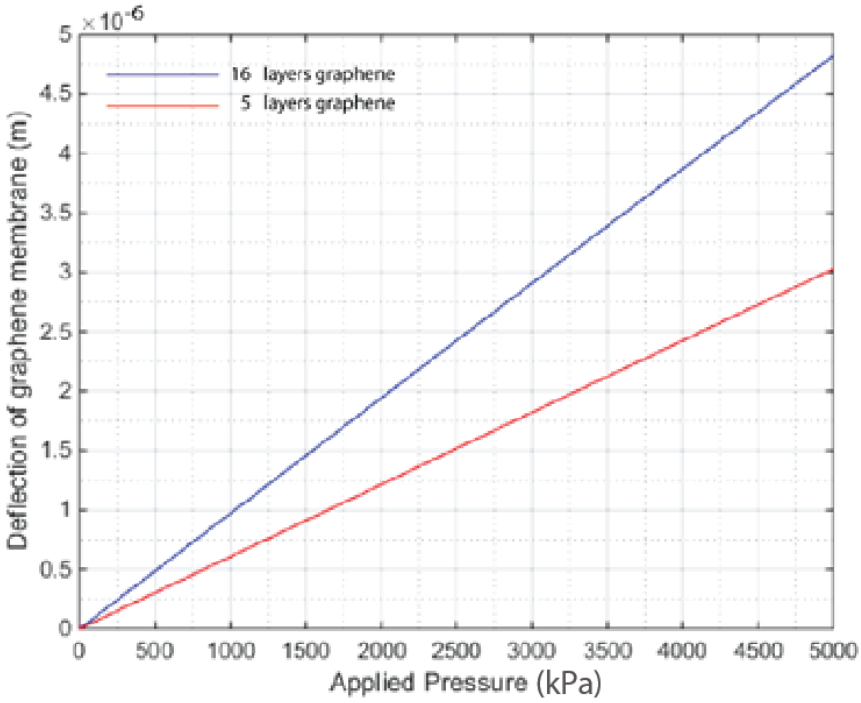

(b)

Figure 6.14 Centre deflection of graphene diaphragm with different thickness and applied pressure (a) r = $12.5\,\mu m$ (b) r= $62.5\,\mu m$

6.4 Summary

In summary, the theoretical design and analysis of high pressure high temperature fibre optic based sensor was developed and characterised. The initial preliminary characterisation of this sensor for harsh environment using a dual sensing approach with glass capillary and aluminium as the coating elements did not produce a desirable results. This was expected as the sensor became inherently fragile when exposed to extreme harsh environments. To overcome this challenge, a technique for protecting the fibre optic sensor when exposed to harsh environment and also has the ability to minimise the effect of cross sensitivity was also studied. However, when the coated metal sensor was simulated in harsh environmental conditions beyond a certain limit, the linear structural properties and the characterization of the sensor start to

decrease. To further address this issue, a parametric analysis was theoretically conducted to study the applicability of ultra-thin multilayer graphene on SiC substrate with strong adhesion, good mechanical strength and thermal stability. The interference characteristics and optical reflection properties are simulated using the transfer matrix model. A $59.67\ \mu m$ cavity length FPI sensor with 16-layer graphene was designed. The theoretical analysis shows that;

The proposed sensor exhibits excellent temperature response measuring upto $1050\ ^{\circ}C$ with good linearity and high sensitivity of $1.02\ nm\ ^{\circ}C^{-1}$. The sensor exhibits a relatively linear response between deflections of the graphene diaphragm and the external applied pressure in the range of $0 - 5000\ kPa$ with ultra-high pressure sensitivity of $2380\ nm\ kPa^{-1}$ for a $125\ \mu m$ diameter 16-layer graphene deposited on SiC substrate. The sensitivity of multilayer graphene diaphragm is more than that of few layer graphene due to the thickness. The diaphragm thickness is a very critical parameter to the reflectivity and additional layers improved the reflectivity. This sensor may have potential for monitoring oil and gas applications in harsh environments.

6.5 References

[1] Y. J. Rao, "Recent progress in fiber-optic extrinsic Fabry–Perot interferometric sensors," *Optical Fiber Technology,* vol. 12, pp. 227-237, 2006.

[2] T. W. Kao and H. F. Taylor, "High-sensitivity intrinsic fiber-optic Fabry–Perot pressure sensor," *Optics Letters,* vol. 21, pp. 615-617, 1996.

[3] W. Wang, N. Wu, Y. Tian, C. Niezrecki, and X. Wang, "Miniature all-silica optical fiber pressure sensor with an ultrathin uniform diaphragm," *Optics Express,* vol. 18, pp. 9006-9014, 2010.

[4] X. Wang, J. Xu, Y. Zhu, K. L. Cooper, and A. Wang, "All-fused-silica miniature optical fiber tip pressure sensor," *Optics Letters,* vol. 31, pp. 885-887, 2006.

[5] Y. Wang, D. N. Wang, C. Wang, and T. Hu, "Compressible fiber optic micro-Fabry-Pérot cavity with ultra-high pressure sensitivity," *Optics Express,* vol. 21, pp. 14084-14089, 2013.

[6] F. Xu, D. Ren, X. Shi, C. Li, W. Lu, L. Lu, L. Lu, and B. Yu, "High-sensitivity Fabry–Perot interferometric pressure sensor based on a nanothick silver diaphragm," *Optics Letters,* vol. 37, pp. 133-135, 2012.

[7] Y. Zhu, K. L. Cooper, G. R. Pickrell, and A. Wang, "High-Temperature Fiber-Tip Pressure Sensor," *Journal of Lightwave Technology,* vol. 24, p. 861, 2006.

[8] H. Bae and M. Yu, "Miniature Fabry-Perot pressure sensor created by using UV-molding process with an optical fiber based mold," *Optics Express,* vol. 20, pp. 14573-14583, 2012.

[9] G. C. Hill, R. Melamud, F. E. Declercq, A. A. Davenport, I. H. Chan, P. G. Hartwell, and B. L. Pruitt, "SU-8 MEMS Fabry-Perot pressure sensor," *Sensors and Actuators A: Physical,* vol. 138, pp. 52-62, 2007.

[10] G. Ferro, "3C-SiC Heteroepitaxial Growth on Silicon: The Quest for Holy Grail," *Critical Reviews in Solid State and Materials Sciences,* vol. 40, pp. 56-76, 2015.

[11] L. H. Chen, C. C. Chan, W. Yuan, S. K. Goh, and J. Sun, "High performance chitosan diaphragm-based fiber-optic acoustic sensor," *Sensors and Actuators A: Physical,* vol. 163, pp. 42-47, 2010.

[12] K. S. Novoselov, A. K. Geim, S. V. Morozov, D. Jiang, Y. Zhang, S. V. Dubonos, I. V. Grigorieva, and A. A. Firsov, "Electric Field Effect in Atomically Thin Carbon Films," *Science,* vol. 306, p. 666, 2004.

[13] C. Lee, X. Wei, J. W. Kysar, and J. Hone, "Measurement of the Elastic Properties and Intrinsic Strength of Monolayer Graphene," *Science,* vol. 321, p. 385, 2008.

[14] S. P. Koenig, N. G. Boddeti, M. L. Dunn, and J. S. Bunch, "Ultrastrong adhesion of graphene membranes," *Nat Nano,* vol. 6, pp. 543-546, 2011.

[15] J. S. Bunch, S. S. Verbridge, J. S. Alden, A. M. van der Zande, J. M. Parpia, H. G. Craighead, and P. L. McEuen, "Impermeable Atomic Membranes from Graphene Sheets," *Nano Letters,* vol. 8, pp. 2458-2462, 2008.

[16] O. K. Kwon, J. H. Lee, K.-S. Kim, and J. W. Kang, "Developing ultrasensitive pressure sensor based on graphene nanoribbon: Molecular dynamics simulation," *Physica E: Low-dimensional Systems and Nanostructures,* vol. 47, pp. 6-11, 2013.

[17] A. D. Smith, S. Vaziri, F. Niklaus, A. C. Fischer, M. Sterner, A. Delin, M. Östling, and M. C. Lemme, "Pressure sensors based on suspended graphene membranes," *Solid-State Electronics,* vol. 88, pp. 89-94, 2013.

[18] J. Ma, W. Jin, H. L. Ho, and J. Y. Dai, "High-sensitivity fiber-tip pressure sensor with graphene diaphragm," *Optics Letters,* vol. 37, pp. 2493-2495, 2012.

[19] J. Ma, H. Xuan, H. L. Ho, W. Jin, Y. Yang, and S. Fan, "Fiber-Optic Fabry-Perot Acoustic Sensor With Multilayer Graphene Diaphragm," *IEEE Photonics Technology Letters,* vol. 25, pp. 932-935, 2013.

[20] C. Berger, Z. Song, X. Li, X. Wu, N. Brown, C. Naud, D. Mayou, T. Li, J. Hass, A. N. Marchenkov, E. H. Conrad, P. N. First, and W. A. de Heer, "Electronic Confinement and Coherence in Patterned Epitaxial Graphene," *Science,* vol. 312, p. 1191, 2006.

[21] W. A. de Heer, C. Berger, M. Ruan, M. Sprinkle, X. Li, Y. Hu, B. Zhang, J. Hankinson, and E. Conrad, "Large area and structured epitaxial graphene produced by confinement controlled sublimation of silicon carbide," *Proceedings of the National Academy of Sciences,* vol. 108, pp. 16900-16905, 2011.

[22] "Dirac point and transconductance of top-gated graphene field-effect transistors operating at elevated temperature," *Journal of Applied Physics,* vol. 116, p. 154504, 2014.

[23] J. L. Tedesco, B. L. VanMil, R. L. Myers-Ward, J. M. McCrate, S. A. Kitt, P. M. Campbell, G. G. Jernigan, J. C. Culbertson, C. R. E. Jr., and D. K. Gaskill, "Hall effect mobility of epitaxial graphene grown on silicon carbide," *Applied Physics Letters,* vol. 95, p. 122102, 2009.

[24] H. Yike, R. Ming, G. Zelei, D. Rui, P. James, H. John, B. Claire, and A. d. H. Walt, "Structured epitaxial graphene: growth and properties," *Journal of Physics D: Applied Physics,* vol. 45, p. 154010, 2012.

[25] J. Hass, F. Varchon, J. E. Millán-Otoya, M. Sprinkle, N. Sharma, W. A. de Heer, C. Berger, P. N. First, L. Magaud, and E. H. Conrad, "Why Multilayer Graphene on 4H -SiC ($000\bar{1}$) Behaves Like a Single Sheet of Graphene," *Physical Review Letters,* vol. 100, p. 125504, 2008.

[26] C. Berger, Z. Song, T. Li, X. Li, A. Y. Ogbazghi, R. Feng, Z. Dai, A. N. Marchenkov, E. H. Conrad, P. N. First, and W. A. de Heer, "Ultrathin Epitaxial Graphite: 2D Electron Gas Properties and a Route toward Graphene-based Nanoelectronics," *The Journal of Physical Chemistry B,* vol. 108, pp. 19912-19916, 2004.

[27] M. Born, E. Wolf, A. B. Bhatia, D. Gabor, A. R. Stokes, A. M. Taylor, P. A. Wayman, and W. L. Wilcock, *Principles of Optics: Electromagnetic Theory of Propagation, Interference and Diffraction of Light*: Cambridge University Press, 2000.

[28] D. E. Aspnes, "Optical properties of thin films," *Thin Solid Films,* vol. 89, pp. 249-262, 1982.

[29] M. Born and E. Wolf, *Principles of Optics: Electromagnetic Theory of Propagation, Interference and Diffraction of Light*, 7 ed. Cambridge: Cambridge University Press, 1999.

[30] M. Bruna and S. Borini, "Optical constants of graphene layers in the visible range," *Applied Physics Letters,* vol. 94, p. 031901, 2009.

[31] J. W. Weber, V. E. Calado, and M. C. M. v. d. Sanden, "Optical constants of graphene measured by spectroscopic ellipsometry," *Applied Physics Letters,* vol. 97, p. 091904, 2010.

[32] F. J. Nelson, V. K. Kamineni, T. Zhang, E. S. Comfort, J. U. Lee, and A. C. Diebold, "Optical properties of large-area polycrystalline chemical vapor deposited graphene by spectroscopic ellipsometry," *Applied Physics Letters,* vol. 97, p. 253110, 2010.

[33] H. F. Mahlein, "Generalized Brewster-angle conditions for quarter-wave multilayers at non-normal incidence," *Journal of the Optical Society of America,* vol. 64, pp. 647-653, 1974.

[34] GuT, PetroneN, J. F. McMillan, A. van der Zande, YuM, G. Q. Lo, D. L. Kwong, HoneJ, and C. W. Wong, "Regenerative oscillation and four-wave mixing in graphene optoelectronics," *Nat Photon,* vol. 6, pp. 554-559, 2012.

[35] D. Yoon, Y. W. Son, and H. Cheong, "Negative Thermal Expansion Coefficient of Graphene Measured by Raman Spectroscopy," *Nano Letters,* vol. 11, pp. 3227-3231, 2011.

[36] D. K. L. Tsang, B. J. Marsden, S. L. Fok, and G. Hall, "Graphite thermal expansion relationship for different temperature ranges," *Carbon,* vol. 43, pp. 2902-2906, 2005.

[37] P. A. R. Tafulo, P. A. S. Jorge, J. L. Santos, F. M. Araujo, and O. Frazao, "Intrinsic Fabry-Perot Cavity Sensor Based on Etched Multimode Graded Index Fiber for Strain and Temperature Measurement," *IEEE Sensors Journal,* vol. 12, pp. 8-12, 2012.

[38] Y. Huang, J. Tao, and X. Huang, "Research Progress on FP Interference Based Fiber-Optic Sensors," *Sensors,* vol. 16, p. 1424, 2016.

Chapter 7

7 Conclusions and recommendations for future work

7.1 Introduction

The work contained in this research was carried out to meet the recent increasing needs for optical fibre based pressure and temperature sensors capable of operating accurately and reliably in harsh environments, specifically for oil and gas applications. The main aim of this research was the design and analysis of optical sensing systems which could be applied in addressing the cross sensitivity problem that may exist in FBG for high pressure high temperature measurements in oil and gas applications. To effectively address this issue, various sensing design configurations and material selection were considered.

This chapter offers the final conclusions of this research, with assessment and analysis of the design system provided. Finally, possible improvement and recommendations for direction of future work are provided.

7.2 Conclusions

The purpose of this research was to design and analyse appropriate optical sensing systems which could be applied in addressing the cross sensitivity problem that may exist in FBG for high pressure high temperature measurements in oil and gas applications. Modelling, simulation and characterization of the Bragg grating which are based on solving the CMT equation by using the transfer matrix method were carried out. The theoretical models of the cross sensitivity function of FBG and it physical mechanism was

developed and analysed. The interaction of the physical parameters and light wave properties pose a serious cross sensitivity challenge on the reliability of FBG sensor. It was concluded that the interactions between the physical properties of FBG and cross sensitivity depict that the cross sensitivity would change widely when external perturbations and fibre materials effects are very large. Different sensing design configurations and analysis were utilised to address the cross sensitivity problem.

A multiplexed FBG/EFPI sensor for simultaneous measurement of temperature and pressure is designed and developed. Analysis of the spectral characterizations (basic sensor system configuration, finesse, fringe visibility, sensor mechanical analysis which includes diaphragm deflection, frequency response and stress distribution) were presented and a de-multiplexing mathematical model for the multiplexed sensor was proposed. This configuration is used to eliminate the issue of temperature-pressure cross-sensitivity and effectively improve the resolution of the sensor system. Experimental results show good linearity between the Bragg wavelength shift and the physical parameters (temperature and pressure), high sensitivity and high accuracy. Moreover, the major limitation to this hybrid sensing configuration was due to the fact that the glass capillary and the aluminium material used for the sensor coating have inherent fragility when the external parameters exceed beyond certain limit and also allowed the independent measurement of pressure and temperature.

To overcome these challenges, a novel technique for protecting the fibre when exposed to HPHT environments while still have the capacity to minimise the effect of cross sensitivity of the sensor was investigated.

The theoretical design and analysis of a double metal coated hybrid sensing system of FBG/EFPI cavity for HPHT measurement in harsh environments was carried out. The FBG is coated with outer protective layer of copper and inner layer of nickel, while the EFPI pressure sensor has an all SiC diaphragm with $1\,mm$ radius, thickness of $40\,\mu m$ and cavity length of $30\,\mu m$. This technique increases the measurement sensitivity of the sensor with respect to the wavelength shift peak when compared to the results obtained for the direct load on the glass capillary and aluminium material on the sensing configuration in section 4.6. The designed sensor has the capability of measuring temperature and pressure between the ranges of $100-1000\,℃$ and $0-5000\,kPa$ respectively. Simulated result shows that this novel double metal coated hybrid sensing system could increase temperature sensitivity from $13.95\,pm\,℃^{-1}$ to $23.89\,pm\,℃^{-1}$ and measured pressure sensitivity up to $21\,\mu m\,kPa^{-1}$.

A novel thin-film fibre optic FBG/EFPI sensor with ultra-high pressure and temperature sensitivities is theoretically analysed using 16-layer graphene film deposited on SiC substrate as the diaphragm. The performance parameters of the proposed sensor are investigated in terms of sensitivity at the operating wavelength of $1550\,nm$ and the proposed sensor exhibits excellent temperature response measuring upto $1050\,°C$, an ultra-high pressure sensitivity of $2380\,nm\,kPa^{-1}$ and temperature sensitivity of $1.02\,nm\,°C^{-1}$.

7.3 Recommendations for future work

In section 4.4, it was depicted that the developed sensor exhibited inherent fragility when exposed to extreme environmental conditions, which was mainly attributed to the glass capillary and the aluminium material used for the sensor coating. To augment for future performance of the sensor, the use of single

crystal sapphire fibre that will enable the sensor to withstand extremely harsh environment with temperature above $1000\,℃$ and a dynamic pressure of above $20000\,kPa$ should be investigated. Single crystal sapphire fibre sensor has the capability to withstand temperature up to $2000\,℃$ without significant performance degradation due to it high melting point of $2040\,℃$, high hardness and resistance to corrosion. Further study could carefully explore the potentials of using single crystal sapphire as the coating material for future optimisation of the sensor.

Also, apart from the two-point peak wavelength interrogation method considered in this research, future study investigating other sensor signal processing and interrogation techniques should be carried.

As demonstrated in chapter 5, the FBG is coated with outer protective layer of copper and inner layer of nickel, while the EFPI pressure sensor has an all SiC diaphragm. Other combination of coating materials should be investigated.

Further research should be undertaken to explore other miniaturised thin-film fibre optic sensors. Example of such miniaturised thin-film is the possibility of combing graphene and sapphire. This will involve depositing multilayer graphene on sapphire fibre tip to form a prototype sensor. The ultra-miniaturised size have the potentials of making such sensors a strong candidate for embedded sensor in oil and gas sensing applications in extreme harsh environments.

This research was mainly based on theoretical analysis and designs, which could have had some impact in the design parameters, performance parameters and results of the sensors based on the assumptions made and boundary conditions considered. In order to validate the results and

performance of the sensor, further laboratory experiment should be carried out.

The downhole optical sensing data is a promising resource for real time downhole monitoring in the oil and gas industry. However, the utilization of these data is still a major challenge due to the noise and the volume of data gathered within a short time. Further study in applying machine learning algorithms to reveal the relationship between the pressure and temperature histories from the sensing data and hence extract the appropriate downhole reservoir model should be investigated.

Appendix A

A The Coupled Mode Theory (CMT)

The CMT is a very important mathematical tool in describing the behaviour of Bragg gratings by analysing the wave propagation and interactions in optical waveguide. It aims to solve the Maxwell's equation for a perturbed waveguide when the electric field E_i can be expressed as the expansion of ideal modes of various summations. They include the transverse field distribution associated with the μ-th guided mode $\mathcal{E}_0$ and the amplitude term A. Also the radiative modes HE and EH define the transversal field distribution. The generalised for of the CMT is expressed as;

$$E_t = \frac{1}{2}\sum_{\mu=1}^{l}\left[A_\mu(z)\mathcal{E}_{\mu,t}e^{i(\omega t-\beta_\mu(z))}\right] + \sum\int_{\rho=0}^{\infty} A_\rho(z)\mathcal{E}_{\rho,t}e^{i(\omega t-\beta_\rho(z))}d\rho \qquad (A-1)$$

the modes satisfy the unperturbed waveguide equation;

$$\nabla^2 E = \mu_0\epsilon_0\frac{\partial^2 E}{\partial t^2} + \mu_0\frac{\partial^2 P}{\partial t^2} \qquad (A-2)$$

The effect of the grating in the perturbed system must be included in the perturbation effect for us to effectively derive the equation of the coupled modes. The polarization vector is expressed as;

$$P = P_{unperturbed} + P_{grating} \qquad (A-3)$$

where

$$P = P_{unperturbed} = \epsilon_0 \chi^{(i)} E_\mu \qquad (A-4)$$

$(A-2)$ is then expressed as;

$$\nabla^2 E = \mu_0 \epsilon_0 \epsilon_r \frac{\partial^2}{\partial t^2} E_{\mu,t} + \mu_0 \frac{\partial^2}{\partial t^2} P_{grating,\mu} \qquad (A-5)$$

Substituting equation $(A-1)$ into $(A-5)$, the unperturbed wave equation becomes;

$$\nabla^2 \left[\frac{1}{2} \sum_{\mu=1}^{l} \left[A_\mu(z) \mathcal{E}_{\mu,t} e^{i\left(\omega t - \beta_\mu(z)\right)} \right] + \sum \int_{\rho=0}^{\infty} A_\rho(z) \mathcal{E}_{\rho,t} e^{i\left(\omega t - \beta_\rho(z)\right)} d\rho \right]$$

$$+ \frac{1}{2} \sum_{\mu=1}^{l} \left[A_\mu(z) \mathcal{E}_{\mu,t} e^{i\left(\omega t - \beta_\mu(z)\right)} \right] + \mu_0 \epsilon_0 \epsilon_r \frac{\partial^2}{\partial t^2} \left[\sum \int_{\rho=0}^{\infty} A_\rho(z) \mathcal{E}_{\rho,t} e^{i\left(\omega t - \beta_\rho(z)\right)} d\rho \right]$$

$$= \mu_0 \frac{\partial^2}{\partial t^2} P_{grating,\mu} \qquad (A-6)$$

When the coupling with radiative modes is neglected, the unperturbed wave equation becomes;

$$\nabla^2 \left[\frac{1}{2} \sum_{\mu=1}^{l} \left[A_\mu(z) \mathcal{E}_{\mu,t} e^{i\left(\omega t - \beta_\mu(z)\right)} \right] \right] + \mu_0 \epsilon_0 \epsilon_r \frac{\partial^2}{\partial t^2} \left[\sum \int_{\rho=0}^{\infty} A_\rho(z) \mathcal{E}_{\rho,t} e^{i\left(\omega t - \beta_\rho(z)\right)} d\rho \right]$$

$$= \mu_0 \frac{\partial^2}{\partial t^2} P_{grating,\mu} \qquad (A-7)$$

The left term of $(A-7)$ shows the modal expansion of the transversal field distribution E_t without the radiative contribution and this justify the unperturbed waveguide equation expressed as;

$$\nabla_t^2 E_t - \mu_0 \epsilon_0 \epsilon_r \frac{\partial^2}{\partial t^2} E_t = 0 \qquad (A-8)$$

The Laplacian operator in $(A-8)$ can be decomposed into transversal and longitudinal terms as;

$$\nabla^2 = \nabla_t^2 + \frac{\partial^2}{\partial z^2} \qquad (A-9)$$

Substituting $(A-9)$ and $(A-8)$ into $(A-7)$, the expression becomes;

$$\frac{\partial^2}{\partial z^2}\left[\frac{1}{2}\sum_{\mu=1}^{l}\left[A_\mu(z)\mathcal{E}_{\mu,t}e^{i\left(\omega t-\beta_\mu(z)\right)}\right]\right] = \mu_0 \frac{\partial^2}{\partial t^2} P_{grating,\mu} \qquad (A-10)$$

The product of the exponential and the amplitude A_μ in $(A-10)$ can further be derived as;

$$\frac{\partial^2}{\partial z^2}\left[\frac{1}{2}\sum_{\mu=1}^{l}\left[A_\mu(z)\mathcal{E}_{\mu,t}e^{i\left(\omega t-\beta_\mu(z)\right)}\right]\right]$$

$$= \frac{\partial}{\partial z}\left[\frac{1}{2}\sum_{\mu=1}^{l}\left[\frac{\partial A_\mu(z)}{\partial z}\mathcal{E}_{\mu,t}e^{i\left(\omega t-\beta_\mu(z)\right)}\right]\right]$$

$$+ \frac{\partial}{\partial z}\left[\frac{1}{2}\sum_{\mu=1}^{l}\left[(-\beta_\mu)A_\mu(z)\mathcal{E}_{\mu,t}e^{i\left(\omega t-\beta_\mu(z)\right)}\right]\right]$$

$$= \frac{1}{2}\sum_{\mu=1}^{l}\left[\frac{\partial A_\mu(z)}{\partial z^2}\mathcal{E}_{\mu,t}e^{i\left(\omega t-\beta_\mu(z)\right)}\right]$$

$$+ \frac{1}{2}\sum_{\mu=1}^{l}(-\beta_\mu)\left[\frac{\partial^2 A_\mu(z)}{\partial z^2}\mathcal{E}_{\mu,t}e^{i\left(\omega t-\beta_\mu(z)\right)}\right]$$

$$+\frac{1}{2}\sum_{\mu=1}^{l}(-\beta_\mu)\left[\frac{\partial^2 A_\mu(z)}{\partial z^2}\mathcal{E}_{\mu,t}e^{i\left(\omega t-\beta_\mu(z)\right)}\right]$$

$$+\frac{1}{2}\sum_{\mu=1}^{l}\left(-\beta^2{}_\mu\right)\left[A_\mu(z)\mathcal{E}_{\mu,t}e^{i\left(\omega t-\beta_\mu(z)\right)}\right] \qquad (A-11)$$

$$= \frac{1}{2}\sum_{\mu=1}^{l}\left[\frac{\partial A_m u(z)}{\partial z^2}\mathcal{E}_{\mu,t}e^{i\left(\omega t-\beta_\mu(z)\right)}\right]$$

$$+\frac{1}{2}\sum_{\mu=1}^{l}(-2i\beta_\mu)\left[\frac{\partial^2 A_m u(z)}{\partial z^2}\mathcal{E}_{\mu,t}e^{i\left(\omega t-\beta_\mu(z)\right)}\right]$$

$$+\frac{1}{2}\sum_{\mu=1}^{l}\left(-\beta^2{}_\mu\right)\left[A_\mu(z)\mathcal{E}_{\mu,t}e^{i\left(\omega t-\beta_\mu(z)\right)}\right] \qquad (A-12)$$

By applying the Slowly Varying Envelope Approximation (SVEA) and grouping the terms in $(A-12)$, the expression becomes;

$$\nabla^2 E_t = \frac{1}{2}\sum_{\mu=1}^{l}\left[(-2i\beta_\mu)\frac{\partial A_\mu(z)}{\partial z}\mathcal{E}_{\mu,t}e^{i\left(\omega t-\beta_\mu(z)\right)} - \beta_\mu^2\, A_\mu(z)\mathcal{E}_{\mu,t}e^{i\left(\omega t-\beta_\mu(z)\right)}\right] \qquad (A-13)$$

By expanding the second term in $(A-13)$, the wave equation becomes;

$$\sum_{\mu=1}^{l}\left[\left(-i\beta_{\mu}\right)\frac{\partial A_{\mu}(z)}{\partial z}\mathcal{E}_{\mu,t}e^{i\left(\omega t-\beta_{\mu}(z)\right)}\right]= \quad \mu_0\frac{\partial^2}{\partial t^2}P_{grating,t} \tag{A-14}$$

The subscript t indicates that $P_{grating,t}$ has a transversal profile. Multiplying $\mathcal{E}_{\mu}^{*}$ to both terms of $(A-14)$ and carrying out integration on the transversal section of the waveguide, we obtain;

$$\sum_{\mu=1}^{l}\int_{-\infty}^{+\infty}\int_{-\infty}^{+\infty}\left[\left(-i\beta_{\mu}\right)\frac{\partial A_{\mu}(z)}{\partial z}\mathcal{E}_{\mu,t}\mathcal{E}_{\mu}^{*}e^{i\left(\omega t-\beta_{\mu}(z)\right)}\right]dxdy$$

$$= \int_{-\infty}^{+\infty}\int_{-\infty}^{+\infty}\mu_0\frac{\partial^2}{\partial t^2}P_{grating,t}\,\mathcal{E}_{\mu}^{*}dxdy \tag{A-15}$$

By applying orthogonality relation, $(A-15)$ becomes;

$$\sum_{\mu=1}^{l}\left[\left(-2i\omega\mu_0\right)\frac{\partial A_{\mu}(z)}{\partial z}\mathcal{E}_{\mu,t}e^{i\left(\omega t-\beta_{\mu}(z)\right)}\right]$$

$$= \int_{-\infty}^{+\infty}\int_{-\infty}^{+\infty}\mu_0\frac{\partial^2}{\partial t^2}P_{grating,t}\,\mathcal{E}_{\mu,t}^{*} \tag{A-16}$$

$(A-16)$ describes different mode coupling techniques, it is applied to both progressive and regressive waves. The equation can be rewritten as;

$$E_t = \left(A_v(z)\mathcal{E}_{v,t}e^{i\left(\omega t-\beta_{\mu}(z)\right)} + B_v(z)\mathcal{E}_{v,t}e^{i\left(\omega t+\beta_{\mu}(z)\right)}\right) \tag{A-17}$$

$$H_t = \left(A_v(z)\mathcal{H}_{v,t}e^{i\left(\omega t-\beta_{\mu}(z)\right)} - B_v(z)\mathcal{H}_{v,t}e^{i\left(\omega t+\beta_{\mu}(z)\right)}\right) \tag{A-18}$$

The progressive mode carries the positive exponent sign while the regressive mode carries the positive exponent sign. Substituting $(A-17)$ and $(A-17)$ into $(A-16)$, we obtain;

$$\left[\frac{\partial A_v(z)}{\partial z}e^{i\left(\omega t-\beta_\mu(z)\right)}\right]-\left[\frac{\partial B_\mu(z)}{\partial z}e^{i\left(\omega t-\beta_\mu(z)\right)}\right]=\frac{i}{2\omega}\int_{-\infty}^{+\infty}\int_{-\infty}^{+\infty}\mu_0\frac{\partial^2}{\partial t^2}P_{grating,t}\,\mathcal{E}^*_{\mu,t}\quad(A-19)$$

$(A-19)$ plays an important role in CMT.

When the dielectric constant ϵ periodically changes along the propagation direction in a material medium, the polarization can be defined by means of perturbed permittivity given as;

$$P=\epsilon_0[\epsilon_r-1+\Delta\epsilon(z)]E_\mu \qquad (A-20)$$

The terms in the bracket are equivalent to $\chi^{(i)}$ in the polarization expression given in $(A-4)$. ϵ_r is the permittivity of the unperturbed medium. Recall that in Physics, the relationship between the refractive index n and the permittivity in a medium can be express as $n^2=\epsilon_r$, this means that we can express;

$$[n+\partial n(z)]^2=\epsilon_r+\Delta\epsilon(z) \qquad (A-21)$$

$$n^2+\partial n(z)^2\;2n\partial n(z)=\epsilon_r+\Delta\epsilon(z) \qquad (A-22)$$

Assuming the perturbation intensity $\partial n(z)$ is very small with respect to the refractive index n, we obtain;

$$\Delta\epsilon(z)\approx 2n\partial n(z) \qquad (A-23)$$

The refractive index modulation is then given as;

$$\partial n(z) \;=\; \overline{\Delta n}\left\{1+\frac{v}{2}\left(e^{1[(2\pi N/\Lambda)z\,+\,\varphi(z)]}\right)\right\}E_{\mu} \qquad (A-24)$$

Where $\overline{\Delta n}$ is the average value of the refractive index variation of the fibre core. v is the fringe visibility and $\varphi(z)$ is the pahse term.

From $(A-19)$,

$$\left[\frac{\partial A_v(z)}{\partial z}e^{i\left(\omega t-\beta_{\mu}(z)\right)}\right]-\left[\frac{\partial B_{\mu}(z)}{\partial z}e^{i\left(\omega t-\beta_{\mu}(z)\right)}\right]=\frac{i\epsilon_0}{2\omega}\int_{-\infty}^{+\infty}\int_{-\infty}^{+\infty}\frac{\partial^2}{\partial t^2}\partial n(z)\left[A_v(z)\mathcal{E}_{v,t}e^{i\left(\omega t-\beta_{\mu}(z)\right)}+B_v(z)\mathcal{E}_{v,t}e^{i\left(\omega t+\beta_{\mu}(z)\right)}\right]\mathcal{E}^{*}_{\mu,v,t}dxdy=\;-in\omega\,\epsilon_0A_v\int_{-\infty}^{+\infty}\int_{-\infty}^{+\infty}\left[\overline{\Delta n}+\frac{\Delta n}{2}\left(e^{1[(2\pi N/\Delta)z\,+\,\varphi(z)]}\right)\right]\mathcal{E}_{\mu,v,t}\;e^{i\left(\omega t-\beta_{\mu}(z)\right)}\mathcal{E}^{*}_{\mu,v,t}dxdy\;+$$

$$-in\omega\,\epsilon_0B_{\mu}\int_{-\infty}^{+\infty}\int_{-\infty}^{+\infty}\left[\overline{\Delta n}+\frac{\Delta n}{2}\left(e^{1[(2\pi N/\Delta)z\,+\,\varphi(z)]}\right)\right]\mathcal{E}_{\mu,v,t}\;e^{i\left(\omega t-\beta_{\mu}(z)\right)}\mathcal{E}^{*}_{\mu,v,t}dxdy \qquad (A-25)$$

The LHS of $(A-25)$ shows the variation rate of A_v and B_{μ} which are determined by the modal order μ and v of the dielectric field. The RHS of the equation has two components A and B for both modes.

$$RHS=-in\omega\,\epsilon_0B_{\mu}e^{i\left(\omega t-\beta_{\mu}(z)\right)}\int_{-\infty}^{+\infty}\int_{-\infty}^{+\infty}\overline{\Delta n}\,\mathcal{E}_{\mu,t}\;\mathcal{E}^{*}_{\mu,t}dxdy\;-$$

$$=-in\omega\,\epsilon_0A_ve^{i\left(\omega t+\beta_{\mu}(z)+\varphi(z)\right)}\int_{-\infty}^{+\infty}\int_{-\infty}^{+\infty}\frac{\Delta n}{2}\mathcal{E}_{v,t}\;\mathcal{E}^{*}_{\mu,t}dxdy \qquad (A-26)$$

Multiplying both sides with $e^{i\left(\omega t-\beta_\mu(z)\right)}$ gives;

$$\frac{\partial B_\mu}{\partial z}= ik_{dc}\beta_\mu + ik_{ac}A - ve^{-i(\Delta\beta_z-\varphi(z))} \quad (A-27)$$

Where $\Delta\beta$ is defined as;

$$\Delta\beta = \beta_\mu + \beta_v - \frac{2\pi N}{\Lambda} \quad (A-28)$$

k_{dc} is the continuous coupling constant defined as;

$$k_{dc} = n\omega\,\epsilon_0 \int_{-\infty}^{+\infty}\int_{-\infty}^{+\infty}\overline{\Delta n}\mathcal{E}_{u,t}\;\mathcal{E}^*_{\mu,t}dxdy \quad (A-29)$$

k_{ac} is the alternate coupling constant defined as;

$$k_{ac} = n\omega\,\epsilon_0 \int_{-\infty}^{+\infty}\int_{-\infty}^{+\infty}\frac{\Delta n}{2}\mathcal{E}_{v,t}\;\mathcal{E}^*_{\mu,t}dxdy = \frac{v}{2}k_{dc} \quad (A-30)$$

Finally, in solving the problem of FBG using the CMT, the progressive mode and the regressive mode are renamed as the $Reference$ and $Signa$l respectively.

$$R = A_v e^{(-i/2)(\Delta\beta_z-\varphi(z))} \quad (A-31)$$

$$S = B_\mu e^{(-i/2)(\Delta\beta_z-\varphi(z))} \quad (A-32)$$

Taking the derivative of $(A-31)$ and $(A-32)$ gives the following expression;

$$\frac{dR}{dz} + i\left[k_{dc} + \frac{1}{2}\left(\Delta\beta - \frac{d\varphi(z)}{dz}\right)\right]R = -ik^*_{ac}S \quad (A-33)$$

$$\frac{dR}{dz} - i\left[k_{dc} + \frac{1}{2}\left(\Delta\beta - \frac{d\varphi(z)}{dz}\right)\right]S = ik_{ac}^{*}R \qquad (A-34)$$

$$\frac{S(0)}{R(0)} = \frac{-k_{ac}\sinh(\alpha L)}{\partial\sinh(\alpha L) - i\alpha\cosh(\alpha L)} \qquad (A-35)$$

Appendix B

Publications

1. Solomon, A. Radhakrishna, P. James, N. 2017. Theoretical design and analysis of a sensing system for high pressure and temperature measurement in subsea underwater applications. Oceans'17 MTS/IEEE Conference, 19th – 22nd June, 2017. Aberdeen UK.

2. S. Udoh, J. Njuguna, R. Prabhu, B. Chirappuram and P. Radhakrishnan. Preliminary Investigation of Temperature and Pressure Measurement System for Down-hole Monitoring of Oil Wells Using FBG/EFPI Sensing Technique. SPE Nigeria Annual International Conference and Exhibition, 4-6 August, Lagos, Nigeria. 2015

3. Solomon Udoh, Radhakrishna Prabhu and James Njuguna, "Modelling and Simulation of Fibre Bragg Grating Characterization for Oil and Gas Sensing Applications", Proceedings of the 2014 International Conference on Systems Informatics, Modelling and Simulation. IEEE Computer Society, 2014

4. Solomon, A. Radhakrishna, P. Analysing the Applicability of Multilayer Graphene Diaphragm for Underwater sensing Applications. Ocean's 2018 MTS/IEEEE Kobe. (SUBMITTED)

5. Ovoke, A., Solomon, A. Babs, O. Application of Non-parametric Bayesian Inversion Gaussian Processes to Multiwell Testing and Anomaly Detection. Society of Petroleum Engineer. (SUBMITTED)